Studies of Nematic to Smectic-A Phase Transitions using Synchrotron Radiation Experimental Techniques and Experiments

Christensen, F.

Publication date:
1981

Document Version
Publisher's PDF, also known as Version of record

Risø-R-459

RISØ

Risø-R-459

Studies of Nematic to Smectic-A Phase Transitions using Synchrotron Radiation Experimental Techniques and Experiments

Finn Christensen

Risø National Laboratory, DK 4000 Roskilde, Denmark
October 1981

Risø-R-459

STUDIES OF NEMATIC TO SMECTIC-A PHASE TRANSITIONS USING SYNCHROTRON RADIATION. EXPERIMENTAL TECHNIQUES AND EXPERIMENTS

Finn Christensen

Abstract. High-resolution X-ray diffraction on liquid crystals, with a triple-axis spectrometer, was initiated 4-5 years ago, using rotating-anode sources. The natural extension of this work was to use the same kind of spectrometer at the much more powerful source provided by synchrotron radiation. This work was initiated during excursions to the DORIS storage ring in Hamburg in 1979-1980. The triple-axis spectrometer, built at Risø, is now permanently positioned at DORIS in HASYLAB and series of dedicated beam time are used by the solid-state physics group at Risø. The triple-axis X-ray spectrometer work in general and especially at the synchrotron source is a new field and a portion of this thesis is devoted to a description of the techniques it uses.

(Continue on next page)

October 1981
Risø National Laboratory, DK-4000 Roskilde, Denmark

The experiments described here are studies of the nematic to smectic-A phase transition in liquid crystals. The first is a study of the monomolecular liquid crystal $\bar{8}S5$ ($C_8H_{17}O-\phi-COS-\phi-C_5H_{11}$, where ϕ denotes a benzene ring). The results of this experiment are compared to those on the bimolecular compounds 8CB ($C_8H_{17}-\phi-\phi-CN$), 8OCB ($C_8H_{17}O-\phi-\phi-CN$), and CBOOA ($C_8H_{17}O-\phi-NCH-\phi-CN$). The second experimental study is one of the reentrance phenomenon in the ternary mixture: $5CT_{.09}$:$7CB_{.x}$:$8OCB_{.91-x}$; where 5CT($C_5H_{11}-\phi-\phi-\phi-CN$) and 7CB($C_7H_{15}-\phi-\phi-CN$) have only a nematic phase and not the smectic-A phase. The results are interpreted in terms of Landau theory, which also explains a pressure-driven reentrance phenomenon in certain pure bilayer compounds (ex. 8OCB).

Finally, a frame is given for discussing the nature of the smectic-A phase and an experiment is proposed to explore the nature of the smectic-A phase together with detailed calculations of (001)- and (002)-lineshapes for the smectic-A phase.

UDC 539.26:548.73

This report is submitted to the Technical University of Denmark in partial fulfilment of the requirement for obtaining the lic. tech. (Ph.D.) degree.

ISBN 87-550-0823-2
ISSN 0106-2840

Risø repro 1982

CONTENTS

Page

ACKNOWLEDGEMENTS

The experimental work, reported on in this thesis, was carried out at the DORIS-storage ring in Hamburg. The author wishes to thank scientists and technicians in HASY-LAB for their skilful guidance, especially Dr. G. Materlik, who provided information on crystal cutting.

The author also wishes to express his deep gratitude to the group of technicians in the Physics Department at Risø, especially S. Bang, E. Dahl Petersen, J. Linderholm, and J. Munck, all of who never refused to spend a night of hard work in Hamburg whenever needed.

I would also like to thank the secretaries in the Physics Department, especially K. Kjøller, and Lis Vang for their patience and skill in typing the draft of the manuscript.

Privately I am greatly indebted to may parents for their support throughout my whole education.

Last, but not least, I gratefully acknowledge the inspiring guidance from and collaboration with Dr. J. Als-Nielsen.

1. INTRODUCTION

Synchrotron radiation has become a powerful tool in experimental physics in recent years, especially since the possibility of dedicated beamtime is growing. A number of well-known experimental techniques in solid-state physics such as X-ray diffraction, EXAFS, photoemission, etc. have been reconsidered in order to match the experimental equipment to the properties of the synchrotron radiation, and a whole new era of experiments have started within the various fields.

In order to pursue the advantages of synchrotron radiation, Dr. J. Als Nielsen at Risø built a triple-axis spectrometer for general-purpose X-ray diffraction in 1978. At the same time construction of a rotating anode was funded. The advantage of having two complementary scattering probes (X-rays and neutrons) at the same place is obvious, and secondly the rotating anode set-up provided the home base for the testing of the triple-axis spectrometer, the development of new experimental equipment, routines, and the training of experimenters, until the triple-axis spectrometer could be moved permanently to the experimental hall of HASYLAB at DORIS in Hamburg. This took place in October 1980. During the 1-1/2 years from May 1979 to October 1980 the spectrometer was brought to EMBL (European Molecular Biology Laboratory) at DORIS for test experiments and actual experiments. During these excursions we worked in a parasitic mode (high-energy physics experiments deciding the energy and the lifetime of the electrons/positrons), but nevertheless we gained valuable experience. All in all everything was well prepared for the dedicated beamtime at HASYLAB in October-November 1980 and it was possible to utilize the dedicated beamtime fully from the start.

This thesis reports on high-resolution X-ray diffraction studies of the nematic to smectic-A phase transition in liquid crystals, using primarily synchrotron radiation. The renewed theoretical

and experimental interest in liquid crystals started in the beginning of the seventies, especially with the theoretical work of de Gennes[1], W.L. McMillan[2], and K.K. Kobayashi[3]. The interest was parallel to the breakthrough in the theory of phase transitions. The new approach to phase transitions, known as renormalization group theory (R.G.T.)[4], provides a number of simple concepts. One of the salient features of the theory is the recognition that critical phenomena associated with continuous phase transitions in two quite different condensed matter systems have some fundamental features in common, provided they belong to the same universality class. This basically means that the interaction space dimensionality d and the order parameter space dimensionality n are the same for the two systems. This leads to a unified picture of the phenomena of continuous phase transitions in condensed matter, regardless of the origin of the physical interaction between the basic constituents of the system. The theory is thus not designed to solve exactly any particular manybody problem in condensed matter physics, but rather describe the critical behaviour. This is done through symmetry considerations, dimensionality considerations and a few basic assumptions. An important concept is that of marginal dimensionalities, d_ℓ being the lower marginal dimensionality and d_u is the upper marginal dimensionality. for $d < d_\ell$ thermal fluctuations destroy the long-range order otherwise favoured by the interactions among the basic constituents. For $d > d_u$ the behaviour in the critical regime can be calculated from mean field theory (M.F.T.). For most condensed matter systems $d_u = 4$ and $d_\ell = 2$.

The phases and phase transitions of liquid crystals have properties which make them uniquely suited for testing these new ideas. The smectic-A phase is namely thought to be a system exactly at lower marginal dimensionality. Furthermore, the nematic to smectic-A transition belongs to the same universality class as superfluid helium and the superconductor in a magnetic field, which lead to predictions for the critical exponents. The analogy between the nematic to smectic-A phase transition and the normal-to-superconducting transition for a metal in an external magnetic field is an even closer one. This analogy

manifests itself in isomorphous (phenomenological) free energy expressions for the spatial fluctuations.

The experimental studies, reported on in this thesis, have been performed on the liquid crystal 8S5, and a ternary mixture of liquid crystals of the following composition: $5CT_9$:$7CB_x$:$8OCB_{91-x}$, where the index x means weight percent. This mixture exhibits a T-x phase diagram with a reentrant nematic phase for $x < 76.74$. $\bar{8}S5$ is out of the family $\bar{n}S5$:C_nH_{2n+1}-ϕ-COS-ϕ-C_5H_{11} where ϕ denotes a benzene ring. This family exhibits the following sequence of phases for $8 < n < 12$: isotropic - nematic - smectic-A - smectic-C - smectic-B - solid. $\bar{8}S5$ was chosen because of its monomolecular smectic-A structure, as opposed to the bimolecular structure of materials such as 8CB, 8OCB, and CBOOA, which have been studied in great detail by J.D. Litster et al.[5].

The reentrant behaviour of the mixture is analogous to the pressure-driven reentrant behaviour in pure compounds like 8OCP which have been studied by P.E. Cladis[6]. There are a number of mixtures which display reentrant behaviour. The one we studied has the advantages of good chemical stability, the reentrant nematic phase being stable, not supercooled, with a completely reversible and second-order phase transition[7].

The plan of the thesis is the following:

Chapter 1: Introduction.

Chapter 2: An overview over liquid crystals, phases and phase transitions, displaying various analogies and theoretical predictions, as briefly outlined in the introduction.

Chapter 3: A discussion of the use of perfect single crystals in high-resolution X-ray diffraction.

Chapter 4: The resolution function of the triple-axis spectrometer. Detailed measurements are shown for a typical liquid crystal set-up at the rotating anode.

Chapter 5: The properties of synchrotron radiation as a radiation source in high-resolution X-ray diffraction. Its measured properties (DORIS - HAMBURG) are compared with calculated ones and with the rotating-anode source at Risø.

Chapter 6: An experimental study of the nature of the second-order nematic-smectic-A phase transition in the monolayer smectic-A component $\bar{8}S5$, performed at the EMBL-outstation at DORIS. The obtained results are compared with similar studies on bilayer compounds such as 8OCB, 8CB, and CBOOA.

Chapter 7: An experimental study of the ternary mixture $5CT_9:7CB_x:8OCB_{91-x}$, exhibiting reentrant nematic behaviour for $x < 76.74$. The study determines the phase diagram, critical exponents for different values of x, and absolute values of correlation lengths. The experimental results are compared with available theoretical predictions.

Chapter 8: Different models for the nature of the smectic-A phase, including calculations of molecular form factors and calculations of the (001)-lineshape and the (002)-lineshape in the smectic-A phase of 8OCB for a specific experimental set-up.

Appendix A: The calculation of the anomalous scattering singularities in the smectic-A phase.

Appendix B: A description of the transformation from one set of conjugate diameters to another.

Appendix C: The numerical deconvolution procedure that is used to obtain correlation-length-data close to T_c.

Appendix D: A description of the combination of resolution ellipses for the triple-axis spectrometer.

Appendix E: The effect of mosaicity of the sample on the resolution function.

REFERENCES

1) P.G. de Gennes (1972) Solid State Commun. 10, 753.
2) W.L. McMillan (1972) Phys. Rev. A6, 936.
3) K.K. Kobayashi (1970) Phys. Lett. 31A, 125.
4) S.K. Ma (1976) Modern Theory of Critical Phenomena, (Benjamin, Reading Mass.) 561 p.
5) J.D. Lister, J. Als-Nielsen, R.J. Birgeneau, S.S. Dana, D. Davidov, F. Garcia-Golding, M. Kaplan, C.R. Safinya & R. Schaetzing (1979) J. Phys. Colloq. Orsay, Fr. 40, C3, 339.
6) P.E. Cladis, R.K. Bogardus, W.B. Daniels & G.N. Taylor (1977) Phys. Rev. Lett. 39, 720.
7) S. Bhattacharya and V. Letcher (1980) Phys. Rev. Lett. 44, 414.

2. LIQUID CRYSTAL MATERIALS, PHASES, AND PHASE TRANSITIONS. ANALOGIES AND THEORETICAL PREDICTIONS

The materials exhibiting liquid crystal behaviour have certain fundamental features in common. As is well known, they are all elongated, rodlike molecules consisting of two or more benzene rings and hydrocarbon chains. Typically, the length of these molecules falls in the 20-30 Å range. There are of course quite a number of materials meeting these requirements, and the spectrum of liquid crystals is quite rich. A table of various liquid crystal materials together with their chemical formula and other relevant information is listed below. These materials have been used quite extensively in the study of the nematic to smectic-A phase transition during the last five years. From the table it is evident that the d-spacing of the smectic-A phase is incommensurable with the molecular length for the compounds CBOOA, CBOA, 8OCB, 8CB and CBNA, but on the other hand, $\ell \approx d$ for $\bar{8}S5$ and 4O.8. This fact has led to a division of smectic-A compounds into two categories, namely: Bilayer smectic-A compounds and monolayer smectic-A compounds.

2.1. Liquid crystal materials and phases

The basic building block of the bilayer smectic-A compounds is thought to be an overlapping configuration of two molecules[2),3)], while in monolayer compounds the basic building block is one molecule. The bilayer compounds are typically molecules with head-tail structure. To be specific let us consider 8CB. Here the C_8H_{17} constitutes the nonpolar tail and Ø-Ø-CN constitutes the polar head (core). Ø denotes a benzene ring.

From this model, assuming a complete overlap of the heads, one may infer that $d \approx a + 2b$[2)] for bilayer smectic-A compounds where a and b are the lengths of the head and tail, respectively. This is in qualitative agreement with the observed

Table 2.1. A survey of some smectic-A compounds. The symbol Ø denotes a benzene ring. The superscript on ℓ and d refers to references. The d's and ℓ's are measured and calculated values, respectively. The spread in d reflects the accuracy of the measurements and the spread in ℓ reflects the lack of precise knowledge of all interatomic distances and some degrees of freedom in the molecular formation.

NAME(S)	CHEMICAL FORMULA	ℓ ≡ MOLECULAR LENGTH (Å)	d ≡ D-SPACING IN SMECTIC-A PHASE	TRANSITION TEMPERATURES °C
8OOA	$C_8H_{17}O$-Ø-NCH-Ø-CN	$26.4^{(3)}/25.6^{(2)}$	$35.10^{(1)}/35.0^{(2)}$	C 73 SA 82.5 N 106.9 I
CBOA	C_8H_{17}-Ø-NCH-Ø-CN	$25.8^{(3)}$	$34.7^{(3)}$	SA 63.8 N 72.2 I
8OCB≡COOB	$C_8H_{17}O$-Ø-Ø-CN	$23.1^{(3)}/23.4^{(2)}$	$31.89^{(1)}/32.0^{(2)}$	C 54.5 SA 67 N 80 I
8CB≡COB	C_8H_{17}-Ø-Ø-CN	$22.4^{(3)}/22.1^{(2)}$	$31.73^{(1)}/31.6^{(2)}/31.0^{(5)}$	C 21 SA 33.6 N 40.6 I
8S5	$C_8H_{17}O$-Ø-COS-Ø-C_5H_{11}	$27.5^{(4)}$	$28.5^{(4)}$	SB ≃35 SC ≃55 SA ≃63 N ≃87 I
40.8	C_4H_9O-Ø-CHN-Ø-C_8H_{17}	$25.4^{(4)}$	$28.5^{(4)}$	SB ≃50 SA ≃64 N ≃79 I
CBNA	C_9H_{19}-Ø-NCH-Ø-CN	$27.0^{(3)}$	$38.1^{(3)}$	C 59 SA 75.1 N 77.5 I

d-spacings. The model has been used in attempts to describe the reentrance phenomena in liquid crystals under pressure qualitatively[3] and has led to a quantitative Landau-theory for the reentrance phenomena (to be discussed later). The monolayer compounds differ from the bilayer compounds chemically by the addition of a carbon-tail, so the general structure is two or more benzene rings in the middle of the molecule and the carbon-tails stretching out to either side.

The liquid crystal phases and phase transitions one observes in these materials are due to the extra, orientational, degree of freedom of the rodlike molecules compared to isotropic molecules/atoms. The phases of principal interest and currently under active study, are: Nematic, Smectic-A, Smectic-C and Smectic-B. All these phases (with the possible exception of Smectic-B, which can probably be classified as a three-dimensional solid) constitute intermediate states of matter (mesophases), between that of the isotropic liquid phase (I) and the three-dimensionally ordered solid phase (S).

A material exhibiting all phases will usually have the following sequence of phases:

$$(*)\ \mathrm{S} \overset{T_{c1}}{\leftrightarrow} \mathrm{Sm\ B} \overset{T_{c2}}{\leftrightarrow} \mathrm{Sm\ C} \overset{T_{c3}}{\leftrightarrow} \mathrm{Sm\ A} \overset{T_{c4}}{\leftrightarrow} \mathrm{Nem} \overset{T_{c5}}{\leftrightarrow} \mathrm{I}$$

with $T_{c1} < T_{c2} < T_{c3} < T_{c4} < T_{c5}$, reflecting the decrease of the order (usually) with increasing temperature. (See also Table 2.1). There exist, however, mixtures of liquid crystals which exhibit a reentrant nematic phase (N*) giving a phase sequence of ...N* ↔ Sm-A ↔ N... . One example is the ternary mixture, reported on in this thesis, $5CT_9$:$7CB_X$:$8OCB_{91-X}$. Also pure compounds may exhibit the same sequence under pressure, f.ex. 8OCB.

The structural characteristics of the three mesophases nematic, Sm-A, and Sm-C are the following:

Nematic: In this phase the centres of gravity of the molecules are distributed at random as in a liquid, but the rodlike molecules are orientationally ordered with their long axes, on the

average, in the same direction, the optical axis of the nematic phase. The variation in space of the direction of the long axes is commonly described by the unit vector $\vec{n}(\vec{r})$, called the director, giving at point $\vec{r}$, the average direction of the long axes. (See Figure 2.1a, where the nematic phase is shown schematically together with the density-variation along the

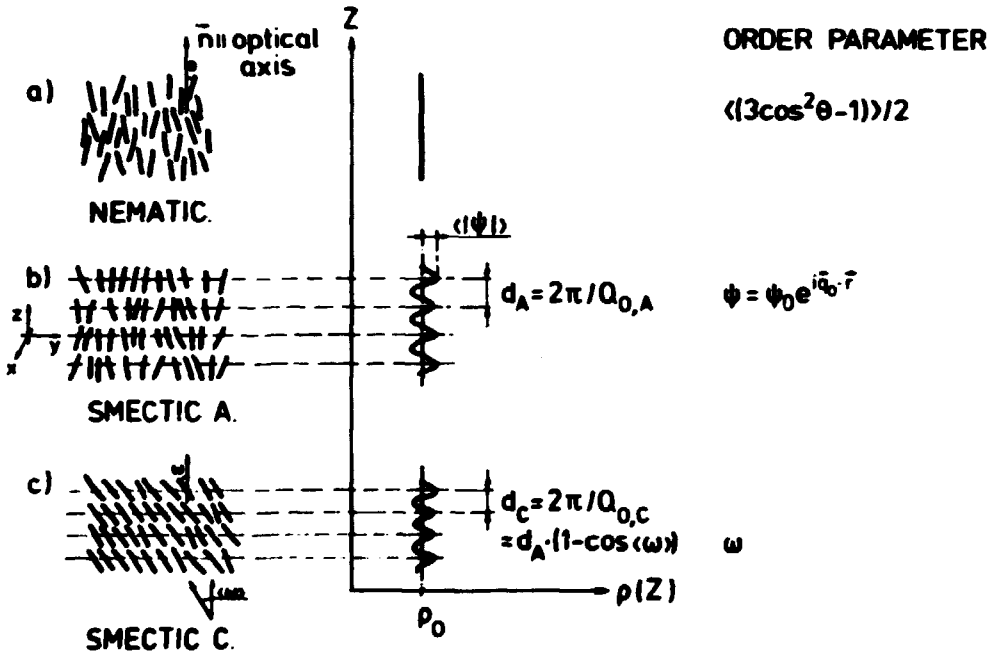

Fig. 2.1. The structural characteristics of the three main mesophases of liquid crystals.

optical axis, here denoted the z-direction.) The order parameter describing the N ↔ I transition is $S \equiv 1/2\langle(3\cos^2\theta-1)\rangle$, where θ is the angle between the optical axis and the long axis of the molecules. S = 1 for total alignment and 0 for the isotropic phase. The parameter $\langle\cos\theta\rangle$ is not the correct order parameter because the directions +n and -n are equivalent, leading to $\langle\cos\theta\rangle = 0$.

A phenomenological theory for the nematic order parameter S has been given by W. Maier & A.Z. Saupe[15)&6)].

Smectic-A: This phase is characterized by the orientational order of the nematic phase and in addition a density-ripple along the z-axis. (See Figure 2.1b.) This gives rise to a layered structure indicated on the schematic drawing. The nature of the layering is discussed in detail in Chapter 8. As will be apparent there exists to this day no conclusive evidence for the exact nature of this layering. Within these layers the positional order of the molecule is still liquidlike. The order parameter for the Sm-A ↔ N transition is the two-component complex order parameter $\psi(\vec{r}) = a(\vec{r}) \cdot e^{iq_o u(\vec{r})}$, where:

$$\rho(\vec{r}) = \rho_o \cdot \{1+\mathrm{Re}(\psi(\vec{r}) \cdot e^{iq_o z})\} \; ; \; q_o = \frac{2\pi}{d} \qquad (2.1)$$

$\rho(\vec{r})$ being the density. Clearly $a(\vec{r})$ is the amplitude of the density ripple and $u(\vec{r})$ is the displacement in the z-direction of the layer at $\vec{r}$. The expression for $\rho(\vec{r})$ assumes a sinusoidal density-ripple. More rigorously, one could regard $\mathrm{Re}\{\psi(r)e^{iq_o z}\}$ as the first harmonic term in a Fourier-series expansion of the density. (See Chapter 8, Section 8.5.)

An extension of the Maier-Saupe mean field theory covering both the nematic-isotropic transition and the nematic smectic-A transition has been outlined by McMillan[16]. He assumes the following expression for the pairwise interaction between the constituent molecules:

$$V_{12}(r_{12},\cos\theta_{12}) = -V_o \cdot e^{-(r_{12}/r_o)^2}[(3/2\cos^2\theta_{12}-1/2)+\delta)]$$

where r_{12} is the distance between centers of mass and θ_{12} is the angle between the long axes of the two molecules. V_o, r_o and δ are the model parameters. The term r_o is of the order of the length of the rigid section of the molecule, and $o<\delta<1$. The next step is to assume the following mean field expression for the one-particle potential:

$$V_1(z,\cos\theta) = -V_o[\eta(3/2\cos^2\theta-1/2)+\alpha\delta\tau\cos(2\pi z/d)$$

$$+\alpha\sigma\cos(2\pi z/d)(3/2\cos^2\theta-1/2)]$$

where z is the position of the center of mass along the z-axis and θ is the angle between the long axis of the molecule and the preferred direction. α is the McMillan parameter:

$$\alpha = 2e^{-(r_o\pi/d)^2}$$

A more general mean field expression for V_1 would contain higher Fourier components[18], but these are neglected. Using V_1,V_{12} is recalculated and self-consistency demands that:

$$\eta = \langle 3/2\cos^2\theta - 1/2 \rangle \; ; \; \tau = \langle \cos(2\pi z/d) \rangle \; ;$$

$$\sigma = \langle \cos(2\pi z/d)(3/2\cos^2\theta - 1/2) \rangle$$

where the thermal average is calculated using the one-particle distribution function $f = e^{-(V_1(z,\cos\theta)/kT)}$.

η is identical to S the orientational order parameter of the nematic phase, τ is the density wave amplitude or the smectic order parameter, σ is a mixed order parameter. The three expressions above can be solved numerically to obtain η,τ,σ vs. temperature for different values of model parameters V_o,r_o (or α) & δ. V_o determines the N-Isotropic transition temperature and fixes the temperature scale of the model. α is a dimensionless interaction strength for smectic ordering. δ is a parameter which allows the translational order to be decoupled from orientational order. McMillan has determined the phase diagram for $\delta = o$, which means that the translational order cannot be decoupled from the orientational. Setting $\delta = 0.65$ and without assuming the specific form of the one-particle potential V_1, which neglects higher Fourier components, Lee et al[17] have used the McMillan form of V_{12} and minimized the free energy with respect to the distribution function f, using a variational form of f, thus obtaining the I-N-SmA phase diagram. The results of McMillan and Lee et al. are in qualitative agreement, but Lee et al. predictions for the phase diagram are in closer agreement with experiment[17]. Regarding the onset of second-order phase transitions, the two calculations differ very little. McMillan's calculation predicts the following:

The transition is first order for $0.7 < \alpha < 1$ and second order for $\alpha < 0.7$, or equivalently the transition is first order if $T_{NA}/T_{NI} > 0.87$ and second order if $T_{NA}/T_{NI} < 0.87$. It is worth noting that experimentally the compounds 8CB, 8OCB and CBOOA all exhibit second-order transitions, with $T_{NI}/T_{NA} < 0.87$ as predicted. Lee et al. predicts 0.88 instead of 0.87. The upper limit on T_{NA}/T_{NI} for second-order transitions reflects the nearly saturated form of the nematic order within the mean field theory, before the nematic to smectic-A transition can take place in a continuous manner.

Smectic-C: This phase is optically biaxial, but otherwise resembles the Sm-A phase. This is microscopically interpreted as a result of a tilting of the molecules within the layers, as sketched in Figure 2.1c. The order parameter for the Sm-C $\leftrightarrow$ Sm-A transition is again a two-component complex scalar of the following form: $\psi(\vec{r}) = \omega(\vec{r}) \cdot e^{i\phi(\vec{r})}$ is the tilt angle and $\phi(\vec{r})$ is the azimuthal angle of the projection of the molecule on the layer. The tilting of the molecules (or $\vec{n}$) drives the layer distance d_C away from this distance in the Sm-A phase, by the simple geometric relation $d_C = d_A\,(1-\cos\langle\omega\rangle)$.

The fundamental static distortions of the nematic phase are described by the phenomenological Frank free energy F_N, which is an expansion in the spatial derivatives of $\vec{n}(\vec{r})$, including only terms which are compatible with the symmetry of the phase. It turns out[6] that F_N can be written:

$$F_N = F_o + 1/2\ K_1(\nabla\cdot n)^2 + 1/2\ K_2(n\cdot(\nabla\times n))^2 + 1/2\ K_3(n\times(\nabla\times n))^2 \qquad (2.2)$$

where K_1, K_2, and K_3 are the Frank elastic constants. Each term in the expansion corresponds to a fundamental distortion. These are:

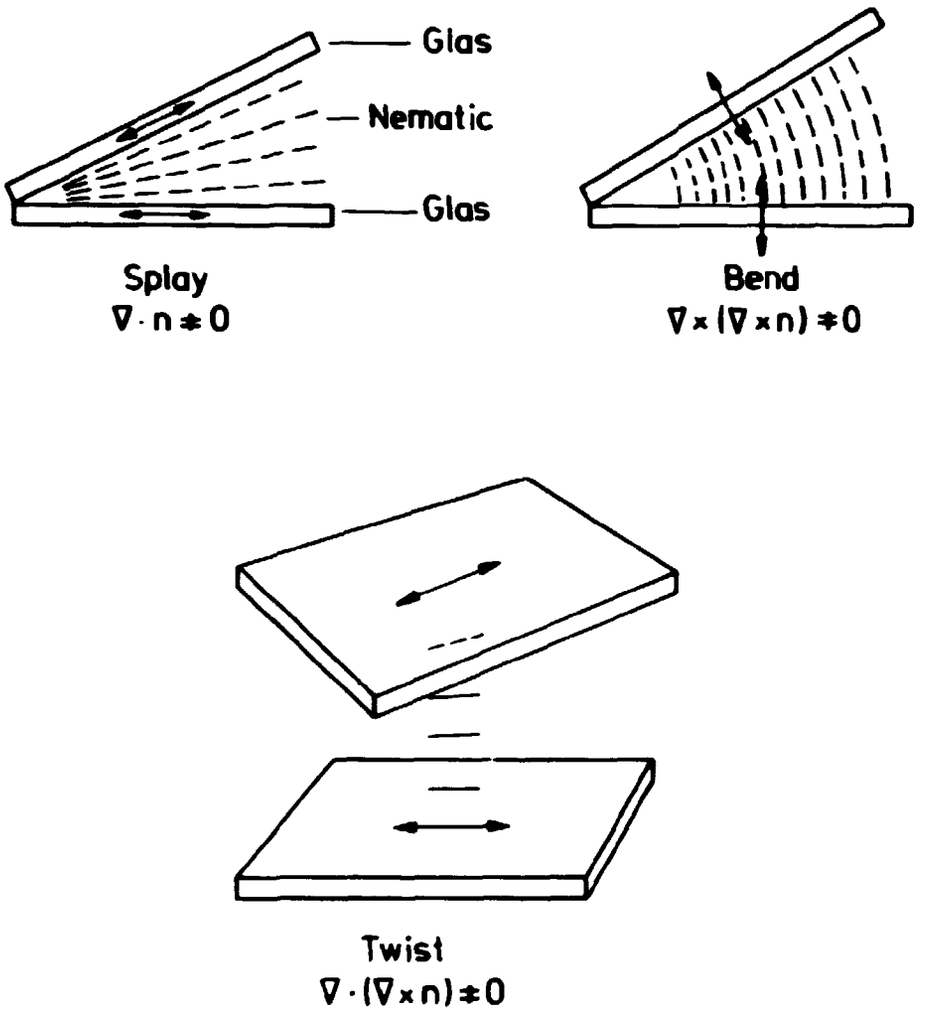

Fig. 2.2. The static distortions of the nematic phase.

SPLAY which corresponds to		$(\vec{\nabla} \cdot \vec{n})^2 \neq 0$
TWIST	- - -	$(\vec{n} \cdot (\vec{\nabla} \times \vec{n}))^2 \neq 0$
BEND	- - -	$(\vec{n} \times (\vec{\nabla} \times \vec{n}))^2 \neq 0$

(See Figure 2.2 where these distortions are drawn schematically.) The elastic constants K_1, K_2, and K_3 can be measured by light wave scattering. In fact, the fluctuations of $\hat{n}$ give rise to strong scattering of light, which makes the nematic phase seem turbid.

The long wavelength fluctuations of the Sm-A-phase can be described using a phenomenological free energy F_S (analogous to the Frank free energy F_N for the nematic phase), which is an expansion in the spatial derivatives of $u(\vec{r})$, compatible with the symmetry of the Sm-A-phase and a few basic assumptions. F_S has the following form[6)&7)]:

$$F_S = F_O + 1/2\ \bar{B}\ (\frac{\partial u}{\partial z})^2 + 1/2\ K_1\ (\frac{\partial^2 u}{\partial x^2} + \frac{\partial^2 u}{\partial y^2})^2 \qquad (2.3)$$

where $\bar{B}$ is a stiffness constant and K_1 is the SPLAY-elastic constant. It is important to understand this form of F_S. The crucial symmetry points and assumptions made in writing down F_S are:

i) -z and +z-directions are equivalent (excludes uneven powers of derivatives)
ii) Simultaneous rotations of layers and molecules do not change the free energy (excluding terms $\propto (\partial u/\partial x)^2$ and $(\partial u/\partial y)^2$).

A term $1/2\ D[(n_x + \partial u/?x)^2 + (n_y + \partial u/\partial y)^2]$, giving the energy associated with fluctuations of the director away from the layer normal is neglected. Fluctuations away from the layer normal are associated with BEND & TWIST-deformations. To a first approximation these are forbidden in the smectic-A phase. (See later.) Formally the neglect of the D-term leads to:

$$\frac{\partial u}{\partial x} = -n_x << 1$$

$$\frac{\partial u}{\partial y} = -n_y << 1 \qquad (2.4)$$

which immediately shows that the term:

$$1/2\ K_1\left[\left(\frac{\partial^2 u}{\partial y^2}\right) + \left(\frac{\partial^2 u}{\partial x^2}\right)^2\right] = 1/2\ K_1\ (\vec{\nabla}\cdot\vec{n})^2$$

is just the SPLAY-term of the nematic phase. The reason for the absence of the TWIST and BEND terms is that, as a first approximation, the layer distance is a constant ≡ d, simply because changing the layer distance requires compression of layers which costs too much energy. The proof that $n\cdot(\nabla\times n)$ and $n\times(\nabla\times n)$ vanishes completely when d is constant is simple as shown below:

$$n_{AB} = \frac{1}{d}\int_A^B \vec{n}\cdot\vec{dl}$$

measures the number of layers crossed when moving from A to B. This means immediately

$$\frac{1}{d}\oint \vec{n}\cdot\vec{dl} = 0 = \frac{1}{d}\int \vec{\nabla}\times\vec{n}\ d\sigma \text{ (according to Stokes's theorem)}$$

which completes the proof.

Terms involving $\propto (\partial^2 u/\partial z^2)$ are neglected as the dominant term is $1/2\ \bar{B}(\partial u/\partial z)^2$. On the other hand, the SPLAY-term cannot be neglected on the same grounds (since, if $\partial u/\partial z = 0$, the splay-term is then the only term left).

In comparison with the nematic phase the layering in the smectic-A phase introduces the new term $1/2\ \bar{B}(\partial u/\partial z)^2$ in the free energy and at the same time only the SPLAY-term survives this layering. In Figure 2.3 the two fundamental distortion configurations are sketched. Figure 2.3a shows a <u>longitudinal</u> displacement distortion, where $\partial u/\partial z \neq 0$ and $\partial^2 u/\partial x^2 = \partial^2 u/\partial y^2 = 0$. Figure 2.3b shows a <u>transverse</u> displacement distortion (undulation mode), where $\partial u/\partial z = 0$ and either $\partial^2 u/\partial x^2$ or $\partial^2 u/\partial y^2 \neq 0$ (or both).

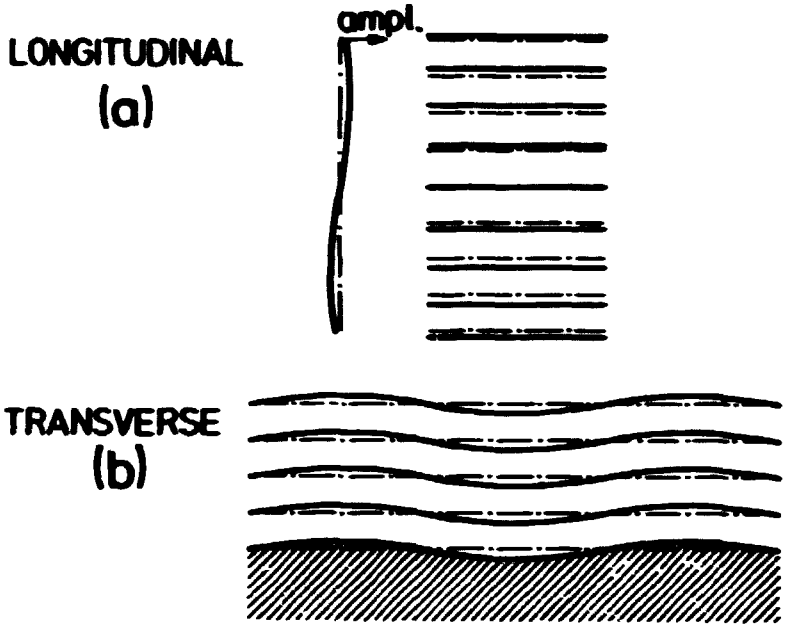

Fig. 2.3. The static distortions of the smectic-A phase.

The peculiar form of F_s has a fundamental implication on the smectic-A phase, which is most easily seen by calculating $\langle u^2(r)\rangle$. Using equipartition on F_s yields:

$$F_s = \frac{V}{2}\Sigma(\bar{B}\, q_z^2+K_1 q_\perp^4)u^2(q) \Rightarrow \langle u^2(q)\rangle = \frac{k_B T}{\bar{B}V(q_z^2+\lambda^2 \cdot q_\perp^4)} \quad ; \quad \lambda \equiv \sqrt{\frac{K_1}{\bar{B}}}$$

(2.5)

λ is the penetration depth for SPLAY-deformations and $1/(\lambda k)^2$ measures how far an imposed undulation mode of wavelength k will penetrate into a smectic-A phase[6]. One gets for $\langle u^2(r)\rangle$:

$$\langle u^2(r)\rangle = \sum_{\vec{q}} \langle u^2(q)\rangle = \frac{V}{(2\pi)^3} \int \langle u^2(q)\rangle \, d\vec{q}$$

$$= \frac{k_B}{8\pi^2} \cdot \int_{-2\pi/d}^{2\pi/d} dq_z \int_{2\pi/L}^{2\pi/d} \frac{2q_\perp \, dq_\perp}{B\, q_z^2 + K_1 q_\perp^4}$$

$$= \frac{k_B}{4\pi\sqrt{BK_1}} \ln\left(\frac{L}{d}\right)$$

where L is the sample dimension and d the layer spacing. This logarithmic divergence of the layer displacement indicates the unique feature of this phase, namely that the Sm-A phase is a system at low marginal dimensionality. The lack of long-range order (L.R.O.) is frequently referred to as the Landau Peierls instability of the smectic-A phase.[14]

The divergence of $\langle u^2(\vec{r})\rangle$ does not, however, mean that the peaks in $S(\vec{q})$: The Fourier transform of the correlation function $G(\vec{r})$ totally disappears. There remain singularities in $S(\vec{q})$, which are weaker than conventional δ-function Bragg-peaks. The calculation of $G(\vec{r})$ and $S(\vec{q})$ was first worked out by Caillé[8] and is done carefully in Appendix A for completeness and because it differs significantly from the usual calculations of thermal diffuse scattering. The result is the following for $q_z = nq_o$, i.e. near the "pseudo" reciprocal lattice points:

$$G(\vec{r}) = \langle e^{iq_z(u(\vec{r})-u(\vec{o}))} \rangle = e^{-2\gamma n} \cdot \left(\frac{2dn}{2\pi n}\right) \cdot e^{-n \cdot E_1\left(\frac{\rho^2}{4\lambda z}\right)} \qquad (2.6)$$

where: γ = Euler const. = 0.577; $\rho^2 = x^2 + y^2$; d = layer spacing

$$\eta = \frac{k_B T q_o^2 \cdot n^2}{16\pi\bar{B}\lambda} \; ; \; E_1(x) \equiv \int_x^\infty \frac{e^{-t}}{t}\, dt \; ; \; \lambda = \sqrt{\frac{K_1}{B}} ; \; nq_o = n \cdot \frac{2\pi}{d}$$

for $\rho << z$:

$$G(\vec{r}) \propto e^{-\gamma\eta} \left(\frac{d^2}{4n^2\pi^2\lambda z}\right)^{\eta} \tag{2.7}$$

for $\rho >> z$:

$$G(\vec{r}) \propto e^{-2\gamma\eta} \left(\frac{2d}{2\pi n\rho}\right)^{2\eta} \tag{2.8}$$

which gives for $S(\kappa)$:

$$S(0,0,q_z) \propto \frac{1}{(q_z - q_o)^{2-\eta}} \quad \text{and}$$

$$S(\vec{q}_\perp,0) \propto \frac{1}{q_\perp^{4-2\eta}} \tag{2.9}$$

The power law decay of $S(\vec{q})$ has been experimentally verified by high-resolution x-ray scattering on 8OCB by Als-Nielsen et al.[9)&10)].

In this study the $S(0,0,q_z)$-lineshape has been measured for a number of temperatures close to T_c. It shows, as expected, an increase of η as $T \to T_c$. K_1 is constant over the narrow temperature range.

2.2. The nematic to smectic-A phase transition. Analogies - theoretical predictions

F_N and F_S describe well the static distortions of respectively the Nematic and Sm-A phases, whereas the phase transition is described using the complex order parameter $\psi(\vec{r}) = a(\vec{r}) \cdot e^{iq_o u(\vec{r})}$ which indicates that the N $\leftrightarrow$ Sm-A transition belongs to the $n = 2$; $d = 3$ universality class. The full free energy

functional used to describe the phase transition is:

$$F = F_o + \alpha|\psi|^2 + \beta|\psi|^4 + \frac{1}{2} M_v \left|\frac{\partial \psi}{\partial z}\right|^2 + \frac{1}{2} M_t \left[\left|\left(\frac{\partial}{\partial x} + iq_o n_x\right)\psi\right|^2 + \left|\left(\frac{\partial}{\partial y} + iq_o n_y\right)\psi\right|^2\right] + F_N \tag{2.10}$$

Inserting $\psi = a(\vec{r}) \cdot e^{iq_o u(\vec{r})}$ yields

$$F = F_o + \alpha \cdot a^2 + \beta \cdot a^4 + \frac{1}{2} M_v \left[\left(\frac{\partial a}{\partial z}\right)^2 + a^2 q_o^2 \left(\frac{\partial u}{\partial z}\right)^2\right] + \frac{1}{2} M_t \left\{\left(\frac{\partial a}{\partial x}\right)^2 + \left(\frac{\partial a}{\partial y}\right)^2 + a^2 q_o^2 \left[\left(n_x + \frac{\partial u}{\partial x}\right)^2 + \left(n_y + \frac{\partial u}{\partial y}\right)^2\right]\right\} + F_N \tag{2.11}$$

by comparing with the free energy expression p. 20, where spatial fluctuations in a were neglected, one can identify: $\bar{B} = 1/2\ M_v\ a^2 q_o^2$ and $D = 1/2\ M_t\ a^2 q_o^2$.

The physical meaning of each of these terms is the following: The first three terms are the usual Landau theory terms, which are the only ones left when neglecting spatial fluctuations. The fourth is the energy cost of <u>longitudinal amplitude fluctuations</u> and <u>longitudinal phase fluctuations</u>. The fifth term, in curly brackets, consists of two different contributions: The first $((\partial a/\partial x)^2 + (\partial a/\partial y)^2)$ is simply the energy cost of <u>transverse amplitude fluctuations</u>. The second the energy cost associated with <u>fluctuations of $n(\vec{r})$ away from the normal</u> to the layers. The sixthhand term is the Frank elastic energy of the nematic phase.

It is worth noting the difference between this free energy functional and the sum of F_S and F_N. One notices that all the terms of F_S and F_N are present, but new ones have appeared. Basically because the order parameter used is a two-component one and because fluctuations of n(r) away from the layer normal are generally allowed.

The form of $F-F_N$ provides the basis for the analogy with superconductors. $F-F_N$ will namely describe a superconductor in a magnetic field $H(r) = \nabla \times A(r)$ where $A(z) = 0$, provided one makes the identification:

$$q_o(n_x,n_y) = -e^*/h\ (A_x,A_y);\ e^* \equiv \frac{2e}{c}$$

which is easily checked by noting that the Landau-Ginzburg free energy for the superconductor is[13]:

$$F_{s.c} = F^N_{s.c} + \alpha|\psi|^2 + \beta|\psi|^4 + \frac{1}{2} M|(-ih\vec{\nabla}-e^*\vec{A})\psi|^2 .$$

It is now interesting to look upon the pretransitional effects which can emerge from $F-F_N$ and compare these with analogous effects in the superconductor. One of the most interesting is the anomalous increase in K_2 and K_3 as T approaches T_c. This effect can be explained in the following manner: Far above T_c the correct description is provided by F_N and for a specific material one has Frank elastic constants K_{10}, K_{20}, and K_{30}. As T approaches T_c fluctuations in ψ will lead to resistance against deformations, as they are not allowed in the smectic-A phase. This effect, which has been measured by D. Litster et al.[1], is the analogy of fluctuation diamagnetism in superconductors as first calculated by Schmid[11]. This pretransitional analogy was pointed out by de Gennes[12].

The magnitude of the effect can be calculated using $F-F_N$; formally it leads to an increase of K_2 and K_3 of the order:

$$\delta K_2 = \frac{k_B}{(24\pi)}\, q_o^2\, (\xi_\perp^2/\xi_{||}) \qquad \xi_{||} = \sqrt{\frac{M_v}{2\alpha}}$$

and

$$\delta K_3 = \frac{k_B}{(24\pi)}\, q_o^2\, \xi_{||} \;;\; \xi_{\perp} = \sqrt{\frac{M_t}{2a}}$$

The most striking advantage of the N ↔ Sm-A phase transition in liquid crystals, as compared to the superconducting transition in metals is the possibility of probing the magnitude of the fluctuation in ψ directly via x-ray measurements and thus follow the divergence of $\xi_{||}$ and $\xi_{\perp}$ in the critical region. To see this one must calculate $S(\vec{q}) = \langle|\rho(\vec{q})|^2\rangle$, where $S(\vec{q})$ is the scattering cross-section and $\rho(\vec{q})$ is the Fourier transform of the density. Around $\vec{q} = \vec{q}_o = (0,0,2\pi/d)$ one finds via the relation between $\rho(\vec{r})$ and $\psi(\vec{r})$: $\langle|\rho(\vec{q})|^2\rangle \propto \langle|\psi(\vec{q}-\vec{q}_o)|^2\rangle$. Neglecting the fourth-order term, F_N, director fluctuations and phase fluctuations in (2.10) gives upon Fourier transforming and equipartition:

$$S(\vec{q}) \propto \frac{k_B T}{a\cdot[1+\xi_{||}^2(q_z-q_o)^2+\xi_{\perp}^2 q_{\perp}^2]} \qquad (2.12)$$

where: $q_{\perp}^2 = q_x^2 + q_y^2$ and $\xi_{||}$, $\xi_{\perp}$ are defined as in the expressions for δK_2 and δK_3.

The Lorentzian structure factor reflects the Ornstein-Zernike form of $\langle\psi^*(0)\psi(r)\rangle$:

$$\langle\psi^*(\vec{0})\,\psi(\vec{r})\rangle \sim \frac{e^{-r/\xi}}{r} \qquad (2.13)$$

and clearly $\xi_{||}$ is a measure of the range of correlation along the long axis of the molecule and $\xi_{\perp}$ measures the range of correlation perpendicular to the long axis of the molecules. High-resolution x-ray measurements have been performed on a number of bilayer smectic-A compounds (8OCB, 8CB, CBOOA) by D. Lister et al.[1]. In these studies it was shown, however, that a fourth-order term $c\cdot\xi_{\perp}^4 q_{\perp}^4$ in the denominator of $S(\vec{q})$ was essential in deconvoluting experimental data.

The analogy with superfluid helium manifests itself only in that this transition belongs to the same universality class (d = 3, n = 2) as the N ↔ Sm-A transition. The R.G.T. predictions for this universality class gives for the divergence of $\delta K_{2,3}$ and $\xi_{||,\perp}$:[12)&19)]

$$\delta K_{2,3} \sim \xi_{||,\perp} \propto t^{-\nu} \; ; \; t \equiv \left(\frac{T-T_c}{T_c}\right)$$

where the critical exponents ν, γ, and η are predicted to be:

$$\nu = \gamma/(2-\eta) = 0.66$$
$$\gamma = 1.30$$
$$\eta = 0.04$$

The Landau approach, where $\alpha \sim (T-T_c)$, predicts the mean-field exponents

$$\nu = 0.5$$
$$\gamma = 1.0$$
$$\eta = 0.0$$

The detailed x-ray scattering experiments[1)] on 8CB, 8OCB & CBOOA show that

$$\nu_{||} = 0.70 \pm 0.04 > \nu_{\perp} = 0.60 \pm 0.04 \text{ and } \gamma = 1.30 \pm 0.04$$

Thus $\nu_{||}$ and γ are in agreement with the liquid He analogy, but $\nu_{\perp}$ is not. This subtle difference between theory and experiment is currently under active study, theoretically as well as experimentally. On the theoretical side there are attempts to explore the effect of the Landau-Peierls instability on the critical behaviour. On the experimental side experiments on monolayer smectic-A materials like 40.8 and $\bar{8}$S5 are made in order to establish whether or not the tendency from the bilayer compounds is true also for the monolayer compounds.

In the experimental studies on $\bar{8}$S5 and the mixture $5CT_9{:}7CB_x{:}8OCB_{91-x}$, the expression (2.12) has been used to analyze the data.

REFERENCES

1) J.D. Litster, J. Als-Nielsen, R.J. Birgeneau, S.S. Dana, D. Davidov, F. Garcia-Colding, M. Kaplan, C.R. Safinya and R. Schaetzing (1979) J. Phys. Colloq. Orsay, Fr. 40, C3, 339.
2) A.J. Leadbetter, J.C. Prost and J.P. Gaughan, G.W. Gray and A. Mosley (1979) J. Phys. Orsay, Fr. 40, 375.
3) P.E. Cladis, R.K. Bogardus and D. Aadsen (1978) Phys. Rev. A, 18, 2292.
4) From measurements at DORIS Hamburg in Oct.-Nov. 1980.
5) J. Stamatoff, P.E. Cladis, D. Guillon, M.C. Cross, T. Bilash and P. Finn (1980) Phys. Rev. Lett. 44, 1509.
6) P.G. de Gennes (1979) The physics of liquid crystals (Clarendon Press, Oxford) 333 p.
7) P.G. de Gennes (1969) J. Phys. Colloq. Orsay, Fr. 30, C4, 65.
8) M.A. Caillé (1977) C.R. Herbd. Seances Acad. Sci. Ser. B, 274, 891.
9) J. Als-Nielsen, R.J. Birgeneau, M. Kaplan, J.D. Litster and C.R. Safinya (1979) Phys. Lett. 39, 1668.
10) J. Als-Nielsen, J.D. Litster, R.J. Birgeneau, M. Kaplan, C.R. Safinya, A. Lindegaard-Andersen and S. Mathiesen (1980) Phys. Rev. B, 22, 312.
11) A. Schmid (1969) Phys. Rev. 180, 527.
12) P.G. de Gennes (1972) Solid State Commun. 10, 753.
13) J.R. Schrieffer (1964) The theory of superconductivity (Benjamin, New York) 282 p.
14) R.E. Peierls (1934) Helv. Phys. Acta 7, Suppl. 11, 81. L.D. Landau (1973) Phys. Z. Sowjetunion. 11, 26.
15) W. Maier & A.Z. Saupe, Z. Naturforsch. A, 13, 564, (1958). 14, 882 (1959). 15, 187 (1960).
16) W.L. McMillan (1971) Phys. Rev. A, 4, 1238. W.L. McMillan (1972) Phys. Rev. A, 6, 936.
17) F.T. Lee, H.T. Tan, Yung Ming Shih and Chai-Wei Woo (1973) Phys. Rev. Lett., 31, 1117.

18) R.B. Meyer and T.C. Lubensky (1976) Phys. Rev. A, 41, 2307.
19) K.G. Wilson (1972) Phys. Rev. Lett., 28, 548.

3. PERFECT SINGLE-CRYSTAL TECHNIQUES IN TRIPLE-AXIS X-RAY DIFFRACTION

The development and use of perfect single crystals in triple-axis X-ray diffraction is fairly new. Specifically, the construction of monochromator crystals specially suited for the white synchrotron radiation is a new field, which has emerged in recent years parallel to the growth in synchrotron radiation facilities. This chapter will summarize the basic techniques employed in triple-axis X-ray diffraction, as it has been used at Risø at the rotating anode and at the DORIS synchrotron in Hamburg during the last three years.

3.1. The perfect crystals

A typical experimental set-up employed in triple-axis, elastic, X-ray diffraction is shown in Figure 3.1, where M is the monochromator and A the analyzer.

For a set-up like the one shown in Figure 3.1, one will almost always use identical crystals as monochromator and analyzer. There is generally no point in using a fixed good collimation on one side of the sample and a fixed bad collimation on the other. On the other hand, one can think of set-ups where an excellent fixed collimation, given by a perfect crystal on the incoming side of the sample, is matched with a slit-system on the outgoint side, which provides a continuously tuneable in-plane resolution. A set-up like this is optimal if one wants to look for weak reflections, since one can relax the collimation on the outgoint side until a reasonable signal can be obtained.

Table 3.1. Scattering angles for commonly used wavelengths and reflections. λ is the wavelength of the radiation, $k = \frac{2\pi}{\lambda}$, d the distance between scattering planes a the length of the cubic unit cell vector and θ the Bragg angle.

			a_{Si}=5.4307Å		a_{Ge}=5.65635Å	
			$d_{Si(111)}$=3.1354Å	$d_{Si(220)}$=1.9200Å	$d_{Ge(111)}$=3.2657Å	$d_{Ge(220)}$=1.9998Å
Radiation	λ/Å	$k/Å^{-1}$	$\theta_{Si(111)}$/deg	$\theta_{Si(220)}$/deg	$\theta_{Ge(111)}$/deg	$\theta_{Ge(220)}$/deg
$CuK_{\alpha 1}$	1.5405	4.0787	14.221	23.651	13.642	22.654
$CuK_{\alpha 2}$	1.5443	4.0686	14.257	23.713	13.677	22.713
$CuK_{\bar{\alpha}}$	1.5424	4.0736	14.239	23.682	13.656	22.683
$CuK_{\beta 1}$	1.3922	4.5131	12.827	21.257	12.307	20.370
$CuK_{\beta 2}$	1.3810	4.5497	12.722	21.078	12.207	20.199
$CuK_{\bar{\beta}}$	1.3866	4.5314	12.775	21.167	12.257	20.285
$MoK_{\alpha 1}$	0.7093	8.8583	6.495	10.644	6.234	10.215
$MoK_{\alpha 2}$	0.7135	8.8061	6.533	10.708	6.272	10.276
$MoK_{\bar{\alpha}}$	0.7114	8.8321	6.514	10.676	6.253	10.246
$MoK_{\beta 1}$	0.6323	9.9370	5.787	9.478	5.555	9.096
$MoK_{\beta 2}$	0.6210	10.1179	5.683	9.307	5.456	8.932
$MoK_{\bar{\beta}}$	0.6267	10.0275	5.736	9.393	5.506	9.015

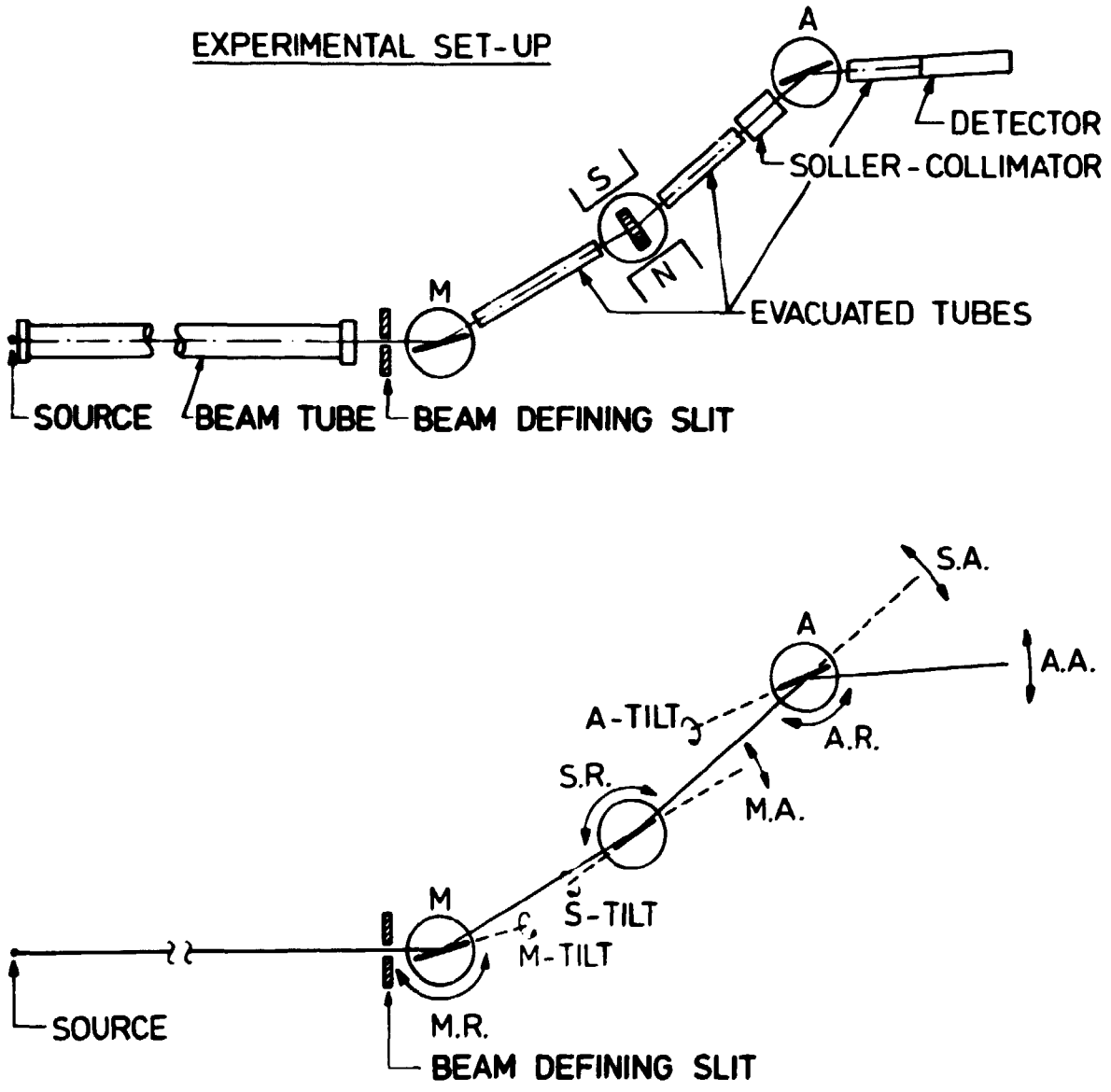

Fig. 3.1. A typical experimental set-up employed in triple-axis, elastic, X-ray diffraction.

The most commonly used crystals are silicon & germanium. Together they cover a rather wide range of resolution. The reflections most often used are Si(111), Si(220), and Ge(111). In Table 3.1 some useful information is given for several of the most frequently used wavelengths.

As shown in the next chapter, the in-plane resolution is determined by the $(\Delta\lambda/\lambda)$-content and the shape of the direct beam profile for the two crystals. For two absolutely perfect crystals, the latter is determined by the Darwin width of the reflection, but also depends on whether the crystals are channel cut or not. In Figure 3.2 two channel-cut crystals are shown, together with the track of the X-rays. On the same figure what is meant by a direct beam profile is shown.

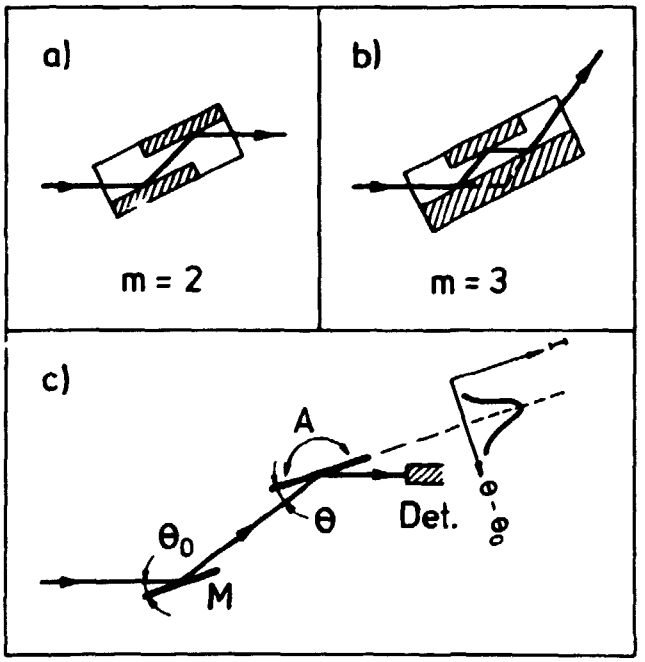

Fig. 3.2. Channel cut crystals. Direct beam profile. θ_0 is the Braggangle corrected for refraction.

3.2. Calculation of reflectivities and direct beam profiles

We have used m = 1 and m = 3 for Si(111) and Si(220) and m = 1 for Ge. It is a straightforward calculation to derive the direct beam profile from dynamical diffraction theory. In several textbooks on X-ray diffraction, like the one of W.H. Zachariasen[1], one can find excellent accounts of this theory. Since this

theory is essential to the resolution considerations given in Chapter 4, I will briefly recall the essential results of dynamical diffraction theory, and also some numerical calculations will be presented.

The scattering geometry for diffraction in a perfect crystal is displayed in Figure 3.3, where a ray of wavevector $\vec{K}_i$ is incident on the crystal surface and a ray of wavevector $\vec{K}_o$ is diffracted from the crystal. (Bragg geometry)

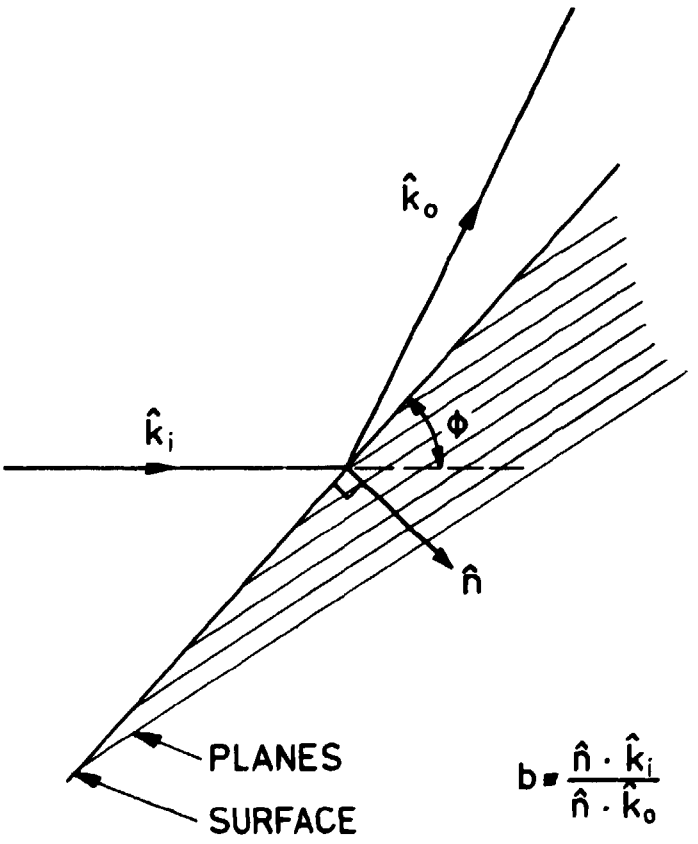

Fig. 3.3. Diffraction of a ray of wavevector $\vec{K}_i$ by an asymmetrically cut crystal.

As is shown in Figure 3.3 the scattering planes need not be parallel to the surface; there may be an angle ϕ between the surface and the scattering planes. In dynamical diffraction theory this asymmetry is expressed by the asymmetry parameter b,

$$b \equiv \frac{\hat{n}\cdot\hat{k}_i}{\hat{n}\cdot\hat{k}_o}$$

where $\hat{n}$ is an inward unit vector normal to the surface. $\hat{k}_i$ and $\hat{k}_o$ are unit vectors along the incident and the diffracted rays, respectively.

The wavelength is connected to the kinematical Bragg angle θ_B by:

$$\lambda = 2d \sin\theta_B$$

where d is the spacing of the diffracting planes.

Basically the dynamical diffraction theory predicts the following: A monochromatic beam incident on a perfect crystal will be almost totally reflected within a narrow angular range, the Darwin width. The center of this angular range $\equiv \theta_o$ will be displaced from the kinematical Bragg angle θ_B, and if the angle of incidence is θ_i ($\equiv$ angle between diffracting planes and incident ray), the angle of reflection $\equiv \theta_r$ ($\equiv$ angle between diffracting planes and diffracted ray) will be:

$$\theta_r = \theta_B - b(\theta_i - \theta_B)$$

Thus it is only for $b = -1$ (corresponding to $\phi = 0$) that $\theta_r = \theta_i$.

The physical origin of the displacement from θ_B to θ_o is that even X-rays will be refracted slightly when entering a crystal. The existence of an angular range of almost total reflection is due to the contribution to the diffraction by only a finite number of layers, simply because the intensity in the incoming beam will decay much faster than dictated by true absorption, when the reflection condition is satisfied.

The following set of equations, taken from W.H. Zachariasen[1], gives the reflectivity $R_{\vec{H}}(\theta)$ for the $\vec{H}$-reflection when true absorption in the crystal is taken into account.

$$R_{\vec{H}}(\theta) = (L - \sqrt{L^2 - (1 + 4\kappa^2)}) \cdot \frac{1}{|C|}$$

$$L = |\sqrt{(y^2 - g^2 - 1)^2 + 4(g \cdot y - \kappa)^2}| + y^2 + g^2$$

and

$$y = \frac{(\frac{1-b}{2})\ \psi'_{\vec{O}} + (\theta_B - \theta)\sin(2\theta_B) \cdot \frac{b}{2}}{K|\psi'_{\vec{H}}|\sqrt{|b|}}$$

θ is the angle of <u>incidence</u>.

$$g = \frac{(\frac{1-b}{2}) \cdot \psi''_{\vec{O}}}{K|\psi'_{\vec{H}}|\sqrt{|b|}} \quad ; \quad \kappa = \frac{\psi''_{\vec{H}}}{\psi'_{\vec{H}}}$$

$\psi'_{\vec{O}}$, $\psi'_{\vec{H}}$ & $\psi''_{\vec{H}}$ are real quantities given by:

$$\psi'_{\vec{O}} = -\Gamma \cdot F'_{\vec{O}} \quad ; \quad \psi''_{\vec{O}} = -\Gamma \cdot F''_{\vec{O}} \quad ; \quad \Gamma = \frac{r_e \lambda^2}{\pi V}$$

$$\psi'_{\vec{H}} = -\Gamma \cdot F'_{\vec{H}} \quad ; \quad \psi''_{\vec{H}} = -\Gamma \cdot F''_{\vec{H}}$$

$F_{\vec{H}} = F'_{\vec{H}} + i\ F''_{\vec{H}}$ is the structure factor for the $\vec{H}$-reflection

$= (f_o + \Delta f' + i\cdot\Delta f'') \cdot F_{\vec{H}}^{Geo} \cdot e^{-M}$; where $F_{\vec{H}}^{Geo} \equiv \sum_j e^{iH\cdot r_j}$ with the sum extending over the basis of the unit cell. r_j is the position of the j'th atom in the basis. r_e is the classical electron radius and v is the volume of the unit cell. f_o = the atomic formfactor. $\Delta f'$ & $\Delta f''$ are dispersion corrections to the atomic formfactor.

M is the Debye-Waller factor and K a polarization factor given by:

$$k = \begin{cases} 1 & ; \text{ polarization of incoming beam } \perp \text{ to scattering plane} \\ |\cos(2\theta)| & ; \text{ polarization of incoming beam in the scattering plane} \\ \left(\frac{1+|\cos 2\theta|}{2}\right) & ; \text{ incoming beam unpolarized.} \end{cases}$$

The formula for $R_+(\theta)$ in the Bragg geometry is valid for strong reflections, where $\psi_{\vec{0}}' >> \psi_{\vec{0}}''$, provided that the crystal has a center of inversion and that $F_{\vec{0}}^{Geo}$ is calculated with the origon of the unit cell in this inversion center!

As mentioned earlier there are a number of general features of the reflection curves. From the above formulas[1)&4)] one may deduce the following:

Due to refraction the center of the reflection curves (corresponding to y = 0) shown on Figure 3.4 is not identical to the kinematical Bragg angle, but is displaced towards higher angles: θ_o on Figure 3.4 is given by

$$\theta_o = \theta_B + (1 - 1/b) \cdot \frac{|\psi_{\vec{0}}'|}{2\sin(2\theta_B)}$$

If the angle of incidence is θ_i the angle of reflection θ_r will be (see Figure 3.8)

$$\theta_r = \theta_B - b(\theta_i - \theta_B)$$

Thus, it is for the b = - 1 case alone that $\theta_r = \theta_i$. A measure for the width of the reflection curves is the angular range for which $-1 < y < 1$, or explicitly:

$$\Delta\theta_i = \frac{2K|\psi'_{\vec{H}}|}{\sqrt{|b|}\,\sin(2\theta_B)} \quad \text{and} \quad \Delta\theta_r = |b| \cdot \Delta\theta_i$$

where i refers to angle of incidence and r refers to angle of emergence.

Since $|\psi'_{\vec{O}}|$ & $|\psi'_{\vec{H}}|$ depends critically on the wavelength λ the reflection curves for higher-order reflections, like Si(333) and Si(440), will be displaced from the fundamental and have a different width. Furthermore, the parameter b is freely adjustable and can be used to enhance the inherent properties of the reflection curves. Section 3.3 will show an example of this.

Table 2. Parameters used to calculate reflectivities. $f_O \to Z$ (No. of electrons) for $\theta \to 0$.

	Si(111)	Si(220)	Ge(111)	Ge(220)
a/Å	5.4307	5.4307	5.65635	5.65635
f_O	11.2	8.75	27.1	23.6
$\Delta f'$	0.2	0.2	-1.3	-1.3
$\Delta f''$	0.4	0.4	1.1	1.1
λ/Å	1.542	1.542	1.542	1.542

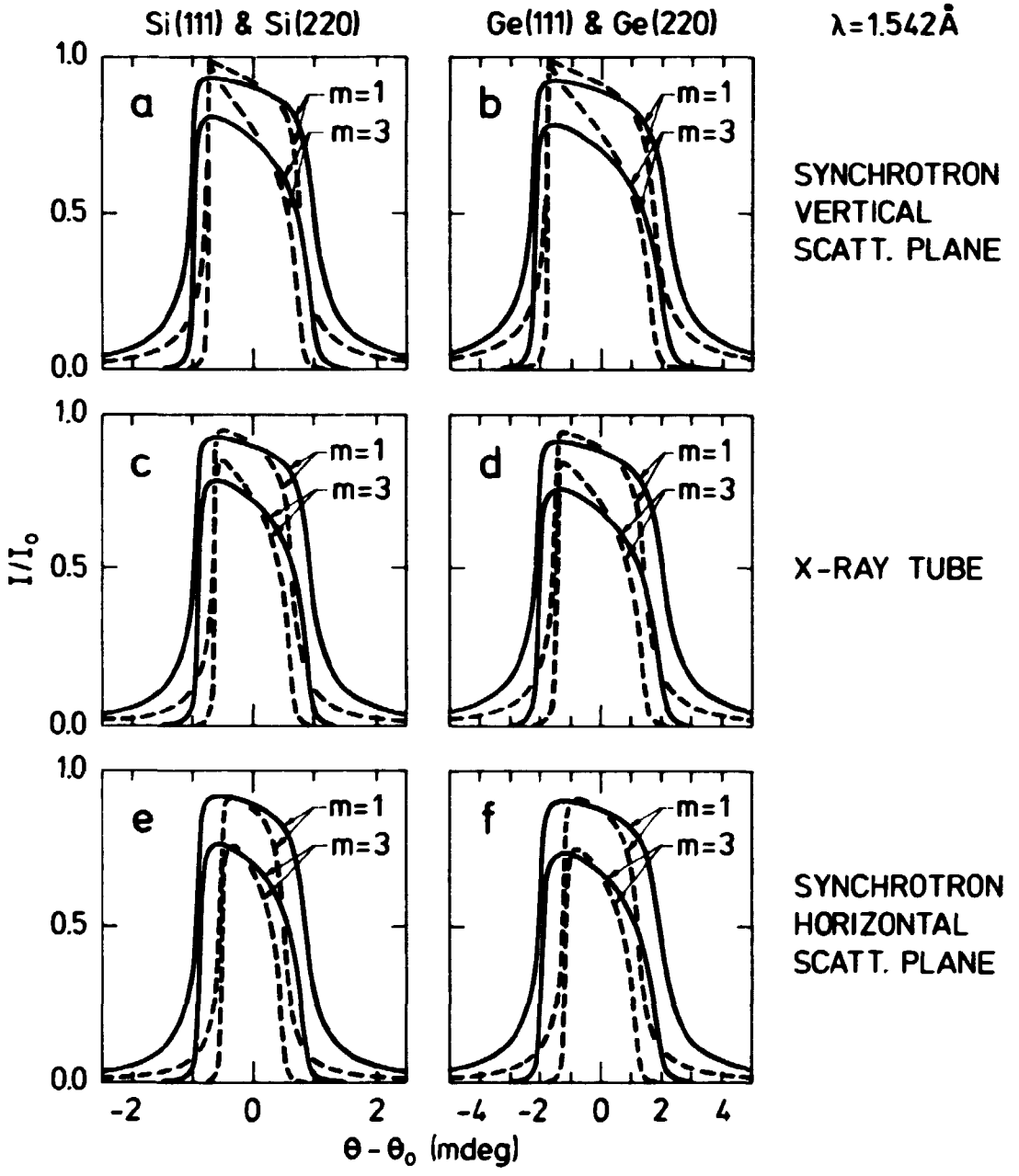

Fig. 3.4. Calculated reflectivities from Si/Ge(111/220); m = 1 & m = 3. Full lines correspond to (111)-reflections. Dotted lines correspond to (220)-reflections. a), c) & e): Si, b), d) & f): Ge. a), b) $\vec{E}$ ⊥ to scattering plane. c) & d) unpolarized incoming beam. e) & f) $\vec{E}$ in the scattering plane.

With the scattering planes parallel to the surface, the asymmetry parameter b is -1 and the reflectivity after m reflections in a channel-cut crystal is simply given by $(R(\theta))^m$. In Figure 3.4 the results of a numerical calculation are shown for m = 1 and m = 3 for three different polarizations of the incoming beam. i) The electric field $\vec{E}$ ⊥ to the scattering plane, ii) unpolarized and iii) the electric field $\vec{E}$ in the scattering plane. i) corresponds to a synchrotron with the scattering plane in the vertical plane, ii) to the rotating anode, and iii) to a synchrotron, with the scattering plane in the horizontal direction.

The calculations show that the reflectivity is asymmetric, square-like, and with a width which depends somewhat on m. By performing the direct profile scan, it is the convolution of these curves with themselves (for identical M and A) one measures. The result of a numerical convolution of the reflectivities in Fig. 3.4 is shown in Figs. 3.5 and 3.6. In these same two figures, available data from experiments performed at Risø and in Hamburg are compared with the theoretical calculations. Since the spectrometer can step only 0.5 m deg, the data-points are rather scarce, especially for the Si(220)-reflections. This makes the normalization of the data to the calculated curves uncertain, but nevertheless the agreement is generally excellent and one can conclude that the crystals we have used are truly perfect.

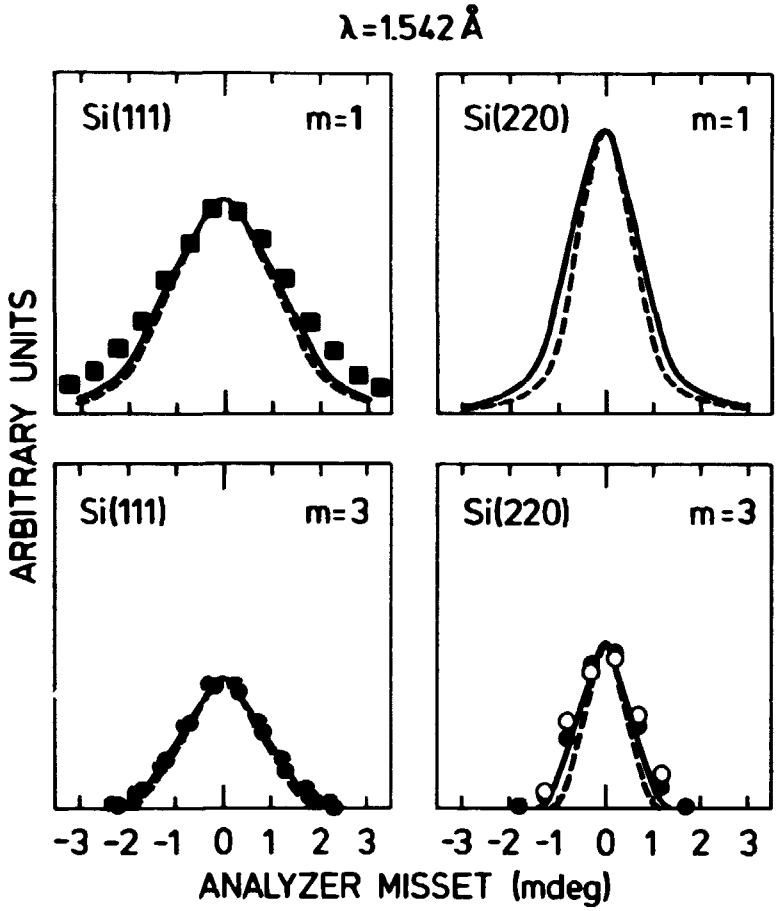

Fig. 3.5. Calculated and measured direct beam profiles for Si(111/220). Full lines correspond to unpolarized incoming beam. (Rot. anode) Dotted lines correspond to $\vec{E}$ in the scattering plane (DORIS). Filled points are data taken at DORIS. Empty points are data taken at the rotating anode.

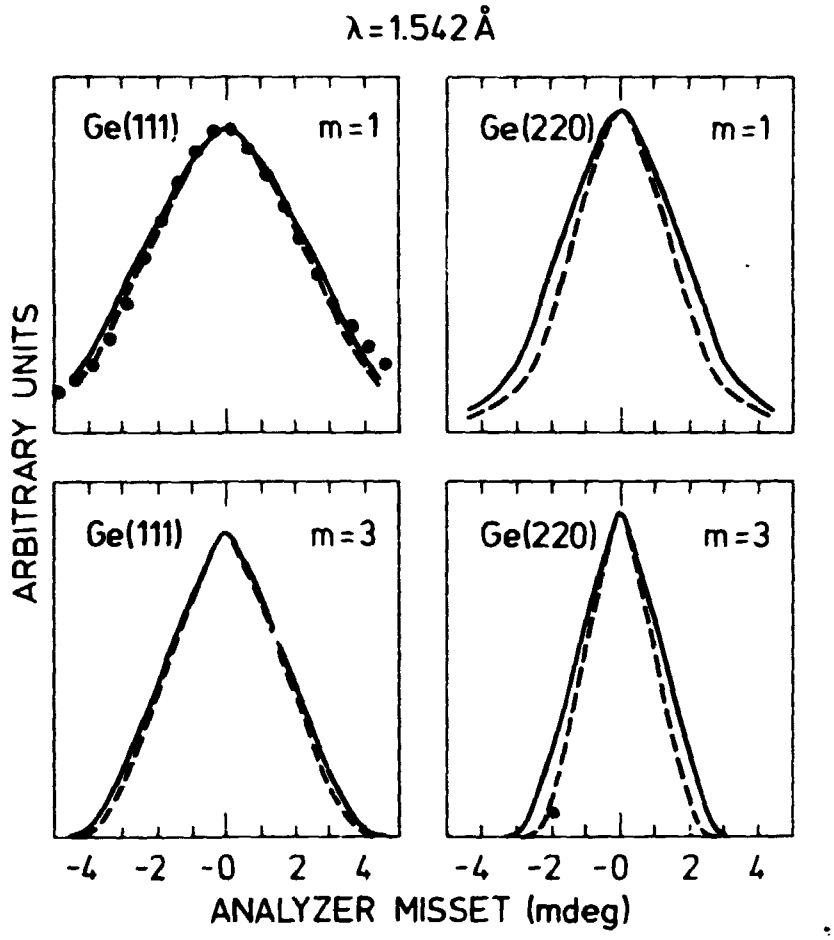

Fig. 3.6. Calculated and measured direct beam profiles for Ge(111/220). Full lines correspond to unpolarized incoming beam. (Rot. anode). Dotted lines correspond to $\vec{E}$ in the scattering plane (DORIS). Data points are taken at DORIS.

The width of the calculated curves is given in Table 3.3. For later reference these will be called D.B.-FWHM (Direct Beam FWHM).

Table 3.3. FWHM in mdeg of direct beam profiles for Si/Ge (111/220)-reflection. Note that (FWHM (⊥-pol) + FWHM (||-pol))/2 ≈ FWHM (unpol). λ = 1.542 Å.

		Si(111)	Si(220)	Ge(111)	Ge(220)
m = 1	⊥pol	2.80	2.10	6.12	4.82
	un-pol	2.65	1.78	5.67	4.04
	||-pol	2.48	1.45	5.37	3.37
m = 3	⊥-pol	1.95	1.45	4.24	3.43
	un-pol	1.84	1.23	4.01	2.80
	||-pol	1.73	0.99	3.76	2.32

The great advantage in using the channel-cut crystals is <u>not</u> the factor ~ 1.5 reduction in D.B.-FWHM one obtains when going from m = 1 to m = 3. So far we have dealt only with the reflectivity close to θ_o. It is well known[1)&2)] that $R(\theta)$, if the thermal motion of the atoms is included, has thermally diffuse wings goint like ε^{-2}, where $\varepsilon \equiv \theta-\theta_o$ or equivalently q^{-2}; where $q \equiv \kappa-\tau$ (τ is the relevant reciprocal lattice vector). Going from $R(\theta) \rightarrow (R(\theta))^3$ will change the q-dependence of the reflectivity to q^{-6} and thereby also drastically influence the wings of the direct beam profile. Even though the direct beam profile is a convolution of reflectivities, this will not alter the q^{-6}-dependence very much.

In Figure 3.7 the investigation of the tails of the direct beam profile is shown for two sets of crystals: 2 × Si(111); m = 3 and 2 × Si(220); m = 3. One can clearly see the effect. It is this effect which has made it possible to probe the detailed lineshape of the smectic-A phase[3)].

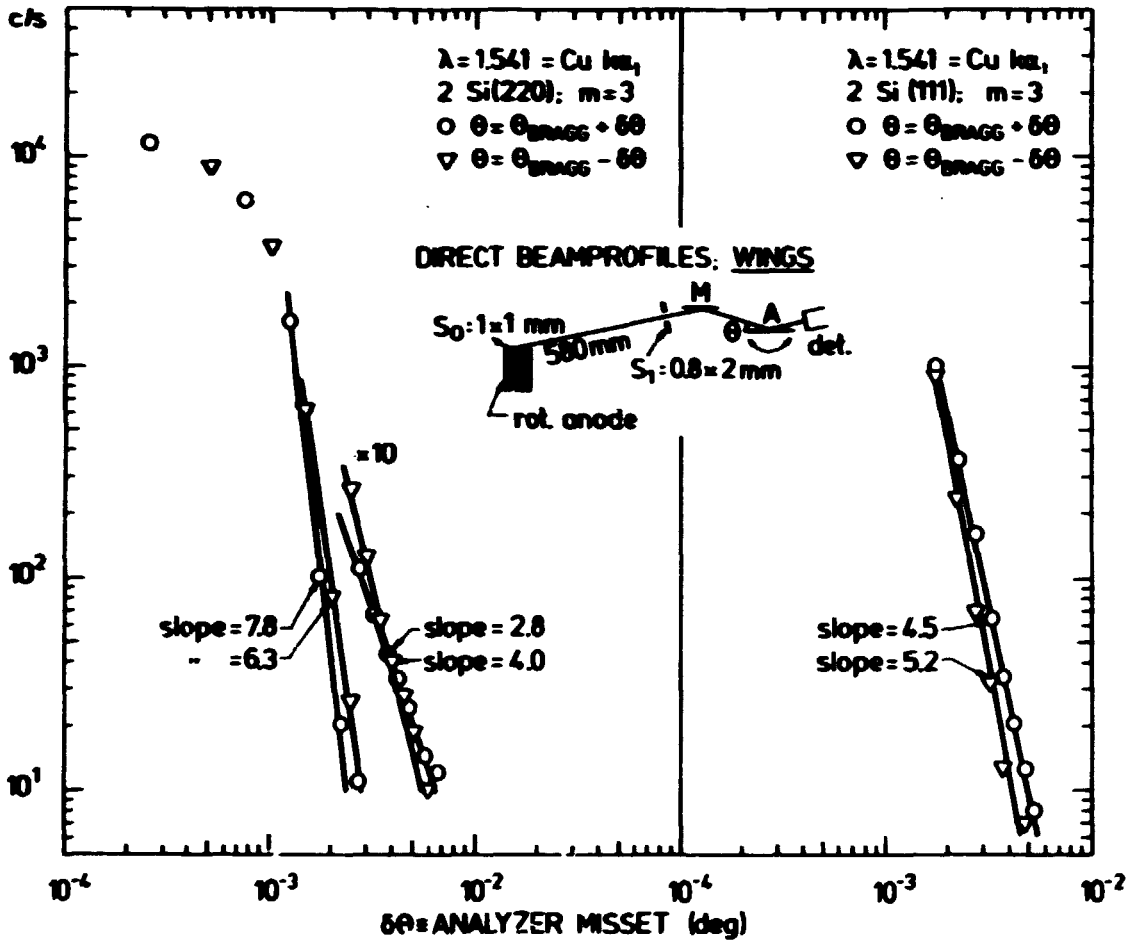

Fig. 3.7. Wings of the direct beam profile for Si(111) & Si(220).

3.3. Design and cutting of a monochromator crystal, especially suitable for white synchrotron radiation

The continuous spectrum of the synchrotron radiation has called for the need of monochromators, which are perfect and which can eliminate higher-order reflections. A recently developed solution to this problem is described in reference[4]. The basic idea is to use either Silicone or Germanium, preferably (Si(111) or Ge(111), since the second harmonic is forbidden in this case, and cut a channel-cut crystal with one of the reflecting surfaces cut at an angle ~ 5° with respect to the scattering

planes, and furthermore introduce a weak link in the crystal, thereby making it possible to offset one of the reflecting surfaces, slightly. Figure 3.8 shows a lay-out for a Si(111) channel cut crystal of this kind.

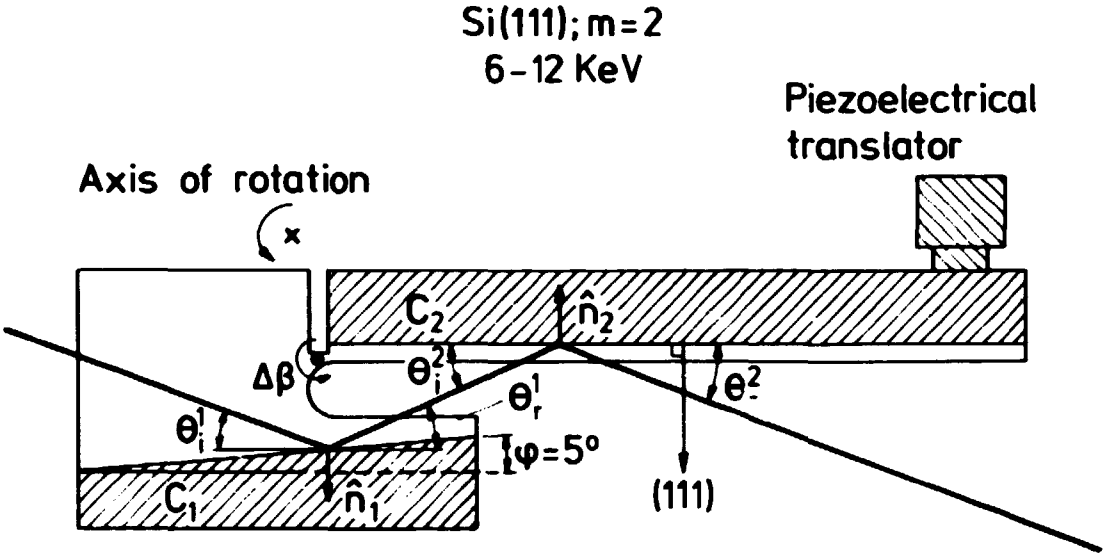

Fig. 3.8. Design of a Si(111)-channel cut monochromator. It is designed to give a reasonable beam size for energies E with 6 keV < E < 12 keV corresponding to 0.8 Å < λ < 2.0 Å.

As noted in the previous section the dependence of $\Delta\theta_i$, $\Delta\theta_r$, and θ_o on the wavelength, and the asymmetry parameter b, can be used to discriminate against higher orders. This is achieved with the arrangement in Figure 3.8. This is most easily seen by calculating the reflectivity curves for the two reflections in the channel-cut crystal. The result is shown in Figure 3.9.

It is clear from Figure 3.9 that the essential trick is to separate the reflectivity regions for higher-order reflections by letting the first crystal be cut asymmetrically.

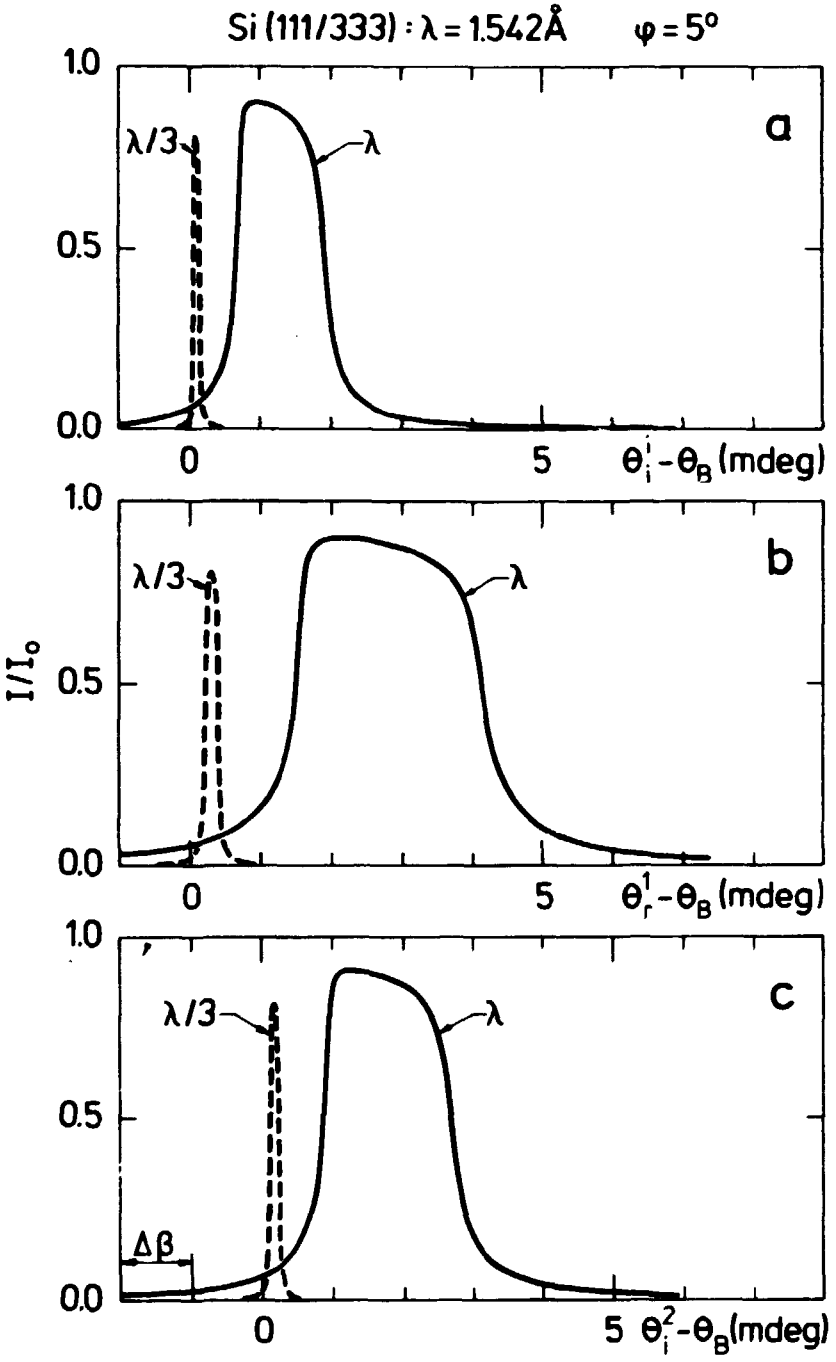

Fig. 3.9. Calculated reflection curves for a double crystal as shown in Figure 7. Parts (a) and (b) give the intensity distributions tied to crystal C_1 for incidence and emergence respectively. Part (c) for crystal C_2 for incidence. Note that the curves for C_2 are shifted with respect to the curves for C_1, $\Delta\beta = 0.001^{\circ}$, thus getting rid of the higher order (333)-reflection. The offset is facilitated by bending C_2 using a piezoelectrical translator.

With $\Delta\beta \sim 1$ mdeg it is essential to be able to bend C_2 with high accuracy. This is obtained by letting a piezoelectrical translator, commercially available, push on the far end of C_2, as shown in Figure 3.8. The piezoelectrical device we used can be set continuously between 0-10 μm by varying the voltage input from 0-1000 volt. This gives a full range for $\Delta\beta$ of approximately 20 mdeg for our final arrangement with the piezo-device ~ 30 mm from the weak link.

The disadvantage of the arrangement in Figure 3.8 is that, since the synchrotron radiation is white, a number of other reflections, Si(α,β,δ); α,β,δ ≠ 1,1,1, may accidentally be reflected and be parallel to the Si(111)-reflection on the outgoing side. It is also clear that this effect is not present for m = 1 & m = 3 channel-cut crystals (see Figure 3.10).

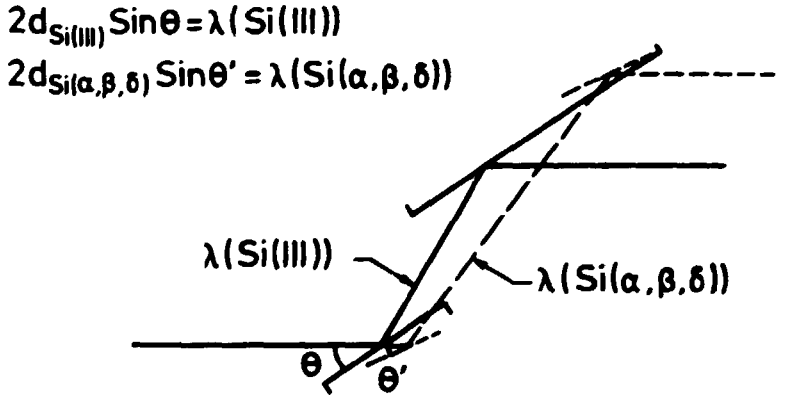

Fig. 3.10. A spurious reflection.

Even though the above-mentioned so-called spurious reflections are parallel to Si(111)-reflection, they will be spatially separated as shown in Reference 4 and a slit system on the outgoing side of crystal can separate these from Si(111).

For the kind of diffraction experiments reported on in this thesis it has not been necessary to eliminate higher-order reflections. The elimination of higher-order reflections is crucial in experiments like EXAFS. For future use I have cut a crystal like the one in Figure 3.8. This was done using a diamond saw in HASYLAB in Hamburg.

After cutting, the crystal must be etched in order to remove surface impurities and dislocations. The etching procedure is done in the following steps:

i) Cleaning: This is done by putting the crystal in sulphuric acid for ~ 12 hours.

ii) Etching: After cleaning in sulphuric acid the crystal is flushed with distilled water and acetone and lastly flushed with methanol. When the crystal is dry it is etched by putting it in a solution of 95% HNO_3 and 5% HF (volume concentration), without touching the crystal with one's fingers. The total amount of solution should not be less than 30 ml per cm^2 of crystal. During etching, which takes approx. 1/2 hour, it is essential to rotate and "bump" the plastic container with crystal and solution all the time. This ensures that the crystal is turned around in the solution, thus getting a uniform etching; furthermore, the "bumping" will remove airbubbles that continuously form on the crystal surface. If these bubbles are not removed the crystal surface will resemble orange peel afterwards, with small grooves all over the surface. Also the crystal should not contact the air above the solution. The whole etching procedure must take place in a ventilated-fume cupboard and every now and then the tightly closed plastic container must be opened to remove the pressure. After etching, the crystal is flushed with acetone and distilled water. The final crystal is shown in Figure 3.11.

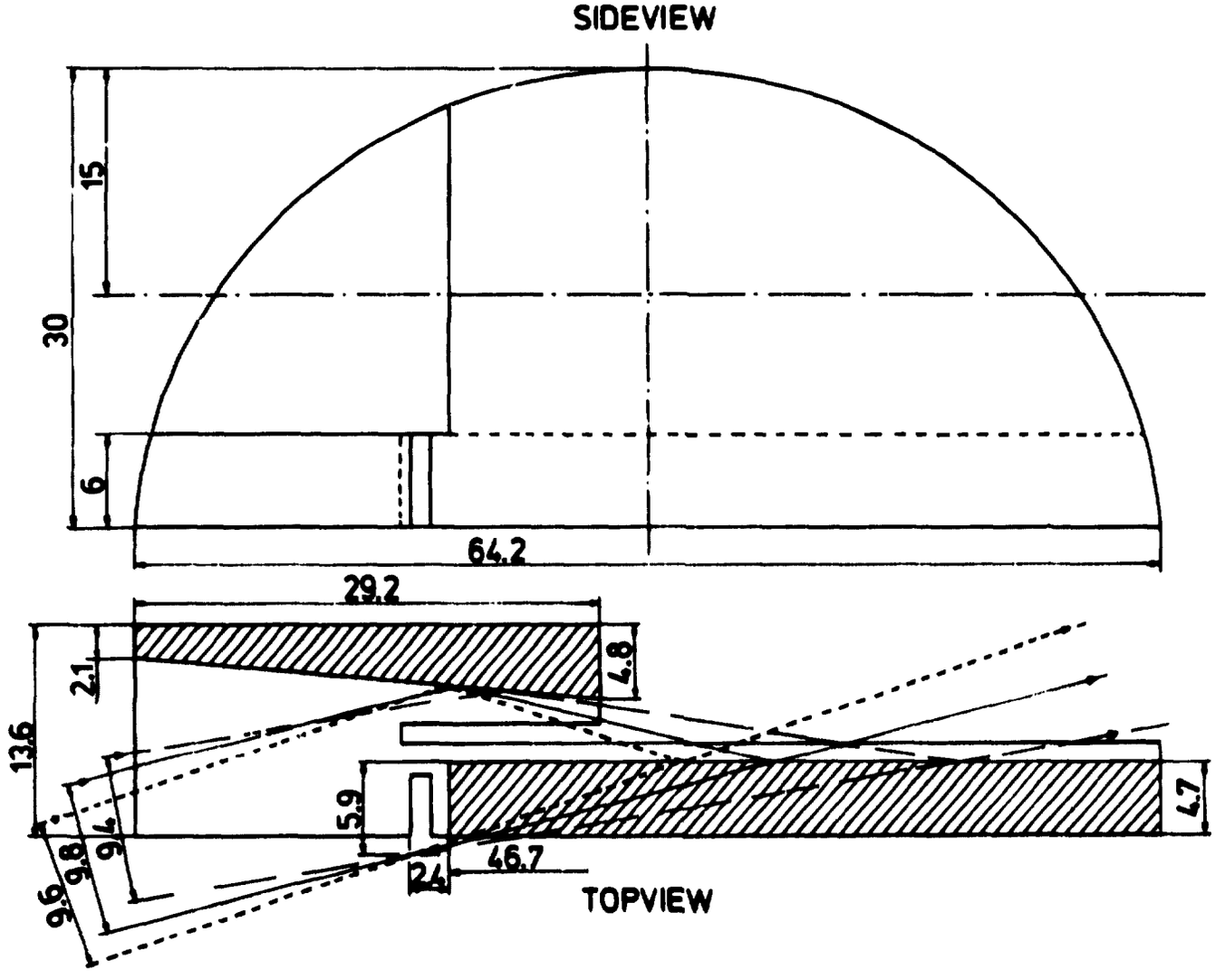

Fig. 3.11. The crystal cut and etched in Hamburg. Dimensions in mm.

REFERENCES

1) W.H. Zachariasen (1967) Theory of X-ray diffraction in crystals (Dover, New York) 255 p.
2) B.E. Warren (1969) X-ray diffraction (Addison-Wesley, Reading, Mass.) 381 p.
3) J. Als-Nielsen, J.D. Litster, R.J. Birgeneau, M. Kaplan, C.R. Safinya, A. Lindegaard-Andersen and S. Mathiesen (1980) Phys. Rev. B, 22, 312.
4) G. Materlik & V.O. Kostroun (1981) Rev. Sci. Instrum. 51, 86.

4. THE RESOLUTION OF THE TRIPLE-AXIS SPECTROMETER

The perfect crystals with Darwin widths ≈ 1 mdeg, provide a high resolution of the triple-axis spectrometer in the scattering plane. This chapter is dedicated to the calculation of the resolution function of the triple-axis spectrometer, when the set-up is as shown in Figure (3.1) in Chapter 3. It will be assumed throughout that the scattering in the sample is elastic and that the monochromator crystal is identical to the analyzer crystal.

4.1. Introduction

The resolution one will obtain depends on the following:

i) The characteristics of the source (spectral distribution, collimation of radiation, etc.) and slit system before the monochromator.
ii) The monochromator crystal and the analyzer crystal.
iii) Collimators and slits in the vertical plane. Note no collimators and slits are necessary in the scattering plane, as the crystals also provide the collimation in the scattering plane apart from monochromatization.
iv) The sample and the scattering angle θ_s.

The resolution function is generally defined via the expression for the measured intensity, when the spectrometer is set to measure at point $\vec{q}$ (often close to a reciprocal lattice vector $\vec{q}_o$):

$$I(\vec{q}) = \int S(\vec{q}-\vec{q}')R(\vec{q}',\vec{q}_o)d\vec{q}' \qquad (4.1)$$

where R is the resolution function and S the scattering cross-section. Expression (4.1) states, simply that $R(\vec{q}',\vec{q}_o)$ is the probability of detecting a scattering process at $\vec{q}-\vec{q}'$ when the

spectrometer is set to detect scattered radiation at $\vec{q}$ (close to $\vec{q}_o$).

$R(\vec{q}',\vec{q}_o)$ can be decomposed into two uncorrelated contributions, the out-of-plane, vertical, resolution $R_v(q_v')$ and the in-plane resolution $R_i(\vec{q}_i')$.

The in-plane resolution is determined by i), ii), and iv) and the out-of-plane resolution, the vertical resolution, will be determined by iii). Note that R generally varies throughout reciprocal space, indicated by the $\vec{q}_o$ in the argument.

4.2. The in-plane resolution

The finite energy-bandwidth of the incoming radiation (i) and the finite collimations in the scattering plane (ii), make it impossible to set the spectrometer to detect radiation of one energy E at one point in reciprocal space $\vec{q}$. There will always be a certain amount of uncertainty in the direction and the magnitude of the detected wavevector k in the scattering plane. This uncertainty, or probability distribution, can be separated into two contributions: one tied to the monochromator and another, similarly, tied to the analyzer crystal[1]. Once these two contributions are calculated it is possible to combine them using the condition of elastic scattering in the sample, to a final in-plane resolution function R_i.

In the following it will be assumed that all probability distributions are Gaussian, thus making it possible to use the concepts of half contour ellipses and conjugate diameters[1].

The basic problem is then to calculate the conjugate diameters X_1, X_2 & X_3, X_4 in the language of reference 1 & 2. The perfect crystal set-up is shown in Figure 4.1. σ_0, σ_1 are the effective in-plane collimations before and after the monochromator, respectively. Similarly σ_3, σ_4 are the collimations before and after the analyzer crystal. To be specific σ_0, σ_1, σ_3, σ_4 are

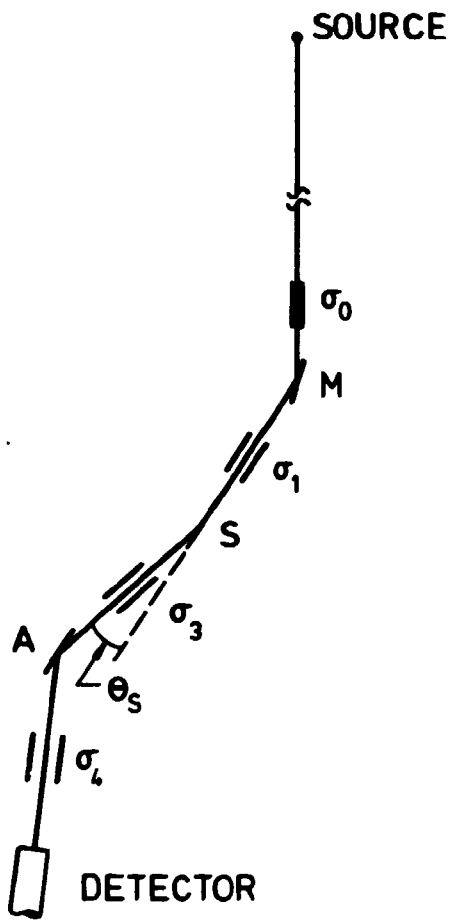

Fig. 4.1. The triple axis set-up with effective collimations.

defined by the probability expression for a ray deviating u degrees from the central ray:

$$P(u) = e^{-\frac{1}{2}\left(\frac{u}{\sigma_{0,1,3,4}}\right)^2}$$

As there are no collimators between the monochromator and the sample, σ_1 is determined by the size of the sample or the monochromator drum-exit slit and the distance between the monochromator and the sample.

The collimations before and after the analyzer crystal are determined in a manner analogous to σ_1. Thus, generally σ_1, σ_3, and σ_4 represent wide angular acceptance collimators, compared to the angular acceptance of a monochromatic beam by a perfect crystal. Representing the square-like reflectivity curves in Figure 3.4 in Chapter 3 by Gaussian functions with the same FWHM, one can introduce, the probability of transmission of a photon of wavevector k in a perfect crystal as:

$$P(m) = e^{-1/2\left(\frac{m}{\sigma_D}\right)^2} \qquad (4.3)$$

where m is the deviation from the Bragg angle corrected for refraction $\equiv \theta_o$ (see Chapter 3) and according to the above:

$$\sigma^2_{1,3,4} >> \sigma^2_{D(arwin)} \qquad (4.4)$$

The characteristics of the source, specifically the energy content of the emerging radiation, play a significant role. In this respect, the synchrotron source and the rotating anode, or simply the X-ray tube, represent two extreme cases. At the synchrotron, where the wavelength of the emerging radiation extends over several decades, one may essentially treat the source as white or in the appropriate language as follows. The probability of emergence of a photon of wave $k+\Delta k$, where k is the mean k-value picked out by the monochromator crystal, can formally be written as

$$P(\Delta k) = e^{-1/2\left(\frac{\Delta k}{k \cdot \sigma_{k-s}}\right)^2} \qquad (4.5)$$

where $\sigma^2_{k-s} >> \sigma^2_{0,1,3,4}$. The subscript -s in σ_{k-s} refers to the source. Since the synchrotron radiation is white, the degree of monochromatization in the monochromator is determined by σ_0, which is given by the distance between the source and monochromator, and the spot size or width of the beam-defining slit (whichever is larger. See Fig. 4.6). With a typical distance of 20 m (DORIS-HASYLAB) between the source and monochromator and a typical source size/width of beam-defining slit of 2-5 mm, one sees that at the synchrotron:

$$\sigma_0^2 << \sigma_{1,3,4}^2 \tag{4.6}$$

At the rotating anode the characteristic $k\alpha_1$-, $k\alpha_2$-, $k\beta$- ... lines of the anode material are sharply confined in energy or k, and for a rotating anode:

$$\sigma_{k-s}^2 << \sigma_{0,1,3,4}^2 \quad ; \quad \sigma_{k-s}(Cuk\alpha_1) = 2.35 \cdot 4 \cdot 10^{-4} = 10^{-3} \tag{4.7}$$

Also it is essentially to note that before the monochromator the slit system usually served only to help separate $k\alpha_1$- from $k\alpha_2$- radiation and thus all of the collimations represented by σ_0, σ_1, σ_3, and σ_4 obey:

$$\sigma_{0,1,3,4}^2 >> \sigma_D^2 \tag{4.8}$$

The above considerations are summarized in Table 4.1.

Table 4.1. Relations among the essential parameters determining the resolution function at the synchrotron and at the rotating anode.

	Relations among σ's
Synchrotron	$\sigma_{k-s}^2 >> \sigma_{1,3,4}^2 >> \sigma_{0,D}^2$
Rotating anode	$\sigma_{0,1,3,4}^2 >> \sigma_{k-s,D}^2$

From Table 4.1 one sees that at the synchrotron the essential parameters are σ_0 and σ_D, while at the rotating anode the essential parameters are σ_{k-s} and σ_D, results which agrees with what one would expect a priori. In the next section the conjugate diameters $\vec{X}_1$, $\vec{X}_2$, $\vec{X}_3$ and $\vec{X}_4$ are determined using the above relations.

4.3. Calculation of X_1, X_2, X_3, X_4 - the conjugate diameters

The following calculation is based on lecture notes from summer-school in Vienna 1980 on "X-ray scattering with synchrotron radiation". The notes are written by Dr. J. Als Nielsen and deals with resolution in diffraction. During the summer school it became clear that the results for the conjugate diameters for the case of an imperfect crystal with a mosaicity distribution much broader than the Darwin width, could not be carried over directly to the case of a perfect crystal with only the Darwin range of reflectivity. What follows is a calculation of the conjugate diameters for the perfect monochromator crystal and the perfect analyzer crystal. The calculation of the conjugate diameters is based on the method outlined in the above-mentioned notes.

Starting with the monochromator crystal and assuming that the Darwin width is zero gives the situation in Fig. 4.2a, for the central ray and a slightly deviating one.

One has generally:

$$P(u) = e^{-1/2\left(\frac{u}{\sigma_M}\right)^2 - 1/2\left(\frac{u\cdot\cot\theta_M}{\sigma_{k-s}}\right)^2} \quad ; \quad \sigma_M^2 = \frac{\sigma_1^2\sigma_0^2}{\sigma_1^2+\sigma_0^2}$$

where it is used that $\Delta k = k\cdot u\cdot\cot\theta_M$. Using the relations in Table 4.1 one gets at the two sources of interest:

$$\begin{aligned} &\text{Synchrotron: } P(u) = e^{-1/2(u/\sigma_0)^2} \\ &\text{Rot. anode: } P(u) = e^{-1/2\left(\frac{u}{\sigma_{k-s}/\cot\theta_M}\right)2} \end{aligned} \qquad (4.9)$$

Giving the conjugate diameter $\vec{X}_1$ parallel to the scattering planes (Als-Nielsen 1980):

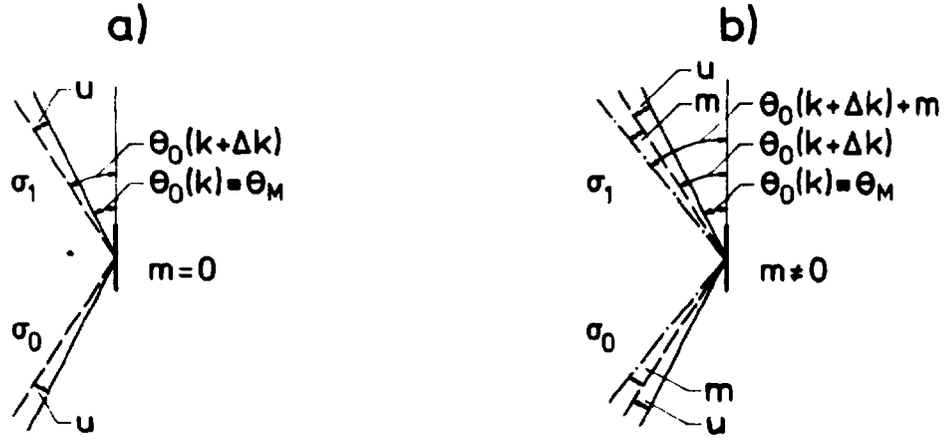

$P(u) = e^{-1/2(u/\sigma_0)^2 - 1/2(u/\sigma_1)^2 - 1/2(\Delta k/k\sigma_k)^2}$

$\Delta k = k \times u \times \cot\theta_M$

$P(u,m) = e^{-1/2((u+m)/\sigma_0)^2 - 1/2((u+m)/\sigma_1)^2 - 1/2(m/\sigma_0)^2 - 1/2(\Delta k/k\sigma_k)^2}$

$\Delta k = k \times u \times \cot\theta_M$

Fig. 4.2. a) Negligible Darwin width. b) Finite Darwin width.

$$X_{1,syn} = C \cdot \frac{k\sigma_0}{\sin\theta_M}$$

$$C = \sqrt{2\ln 2} \qquad (4.10)$$

$$X_{2,rot.\ anode} = C \cdot \frac{k \cdot \sigma_{k-s}/\cot\theta_M}{\sin\theta_M}$$

Introducing a Darwin width ≠ zero or equivalently $\sigma_D \neq 0$ gives the picture in Figure 4.2b, <u>provided</u> that the asymmetry parameter of the reflection ≡ b = -1 (see Chapter 3, Section 3.2). Maintaining $\vec{X}_1$ as one of the conjugate diameters the direction and magnitude of the other $\vec{X}_2$, can be found by looking at the probability distribution P(u,m) (see Figure 4.2b).

$$P(u,m) = e^{-1/2\left(\frac{u+m}{\sigma_M}\right) - 1/2\left(\frac{m}{\sigma_D}\right)^2 - 1/2\left(\frac{u}{\sigma_{k-s}/\cot\theta_M}\right)^2} \qquad (4.11)$$

Using the relation $\sigma^2_{k-s} >> \sigma^2_1 >> \sigma^2_0$ for the synchrotron and the relation $\sigma^2_{0,1} >> \sigma^2_{k-s}$ for the rotating anode, one gets:

$$\text{Synchrotron: } P(u,m) = e^{-1/2\left(\frac{u+m}{\sigma_0}\right)^2 - 1/2\left(\frac{m}{\sigma_D}\right)^2}$$

$$\text{Rot. anode: } P(u,m) = e^{-1/2\left(\frac{u}{\sigma_{k-s}/\cot\theta_M}\right)^2 - 1/2\left(\frac{m}{\sigma_D}\right)^2} \cdot$$

$$e^{-\left(\frac{u \cdot m}{\sigma_M}\right) - 1/2\left(\frac{m}{\sigma_M}\right)^2}$$

These two expressions may be brought on a common form:

$$\text{Synchrotron: } P(u,m) = e^{-1/2\left(\frac{m}{\sigma_D}\right)^2 - 1/2\left(\frac{u-\gamma m}{\sigma_0}\right)^2} \quad ; \quad \gamma = -1$$

$$\text{Rot. anode : } P(u,m) = e^{-1/2\left(\frac{m}{\sigma_D}\right)^2 - 1/2\left(\frac{u-\gamma m}{\sigma_{k-s}/\cot\theta_M}\right)^2} \quad ;$$

$$\gamma = -\frac{\sigma_{k-s}/\cot\theta_M}{\sigma_M} \simeq 0$$

The direction and magnitude of the other conjugate diameter $\vec{X}_2$ can now be found by letting $u = \gamma m$ and setting $m = C \cdot \sigma_D$; $C = 2\sqrt{2\ln 2}$.

For the synchrotron this leads to the following:

$$u = -m \Rightarrow u+m = 0$$

Noting that $\Delta k = k u \cot\theta_M$ one gets that $\vec{X}_2$ for the synchrotron is <u>along $\vec{k}$</u> with a magnitude:

$$X_{2,syn} = C \cdot k \cdot \sigma_D \cdot \cot\theta_M \qquad (4.12)$$

For the rotating anode one gets:

$$u = \gamma m \Rightarrow u = 0$$

Noting again that $\Delta k = k u \cot\theta_M$ one gets that $\vec{X}_2$ for the rotating anode is <u>perpendicular to $\vec{k}$</u> with a magnitude:

$$X_{2,rot.anode} = C \cdot k \cdot \sigma_D \qquad (4.13)$$

Table 4.2 and Figure 4.3 summarize the result for the conjugate diameters for the monochromator at the synchrotron and at the rotating anode.

Table 4.2. The conjugate diameters for the monochromator at the synchrotron source and at the rotating anode.

	x_1	dir. of $\vec{x}_1$	x_2	dir. of $\vec{x}_2$
Synchrotron	$C \cdot \frac{k\sigma_0}{\sin\theta_M}$	along scatt. planes	$Ck\sigma_D\cot\theta_M$	along $\vec{k}$
Rotating anode	$C \cdot \frac{k\sigma_{k-s}/\cot\theta_M}{\sin\theta_M}$	- " -	$Ck\sigma_D$	$\perp$ to $\vec{k}$

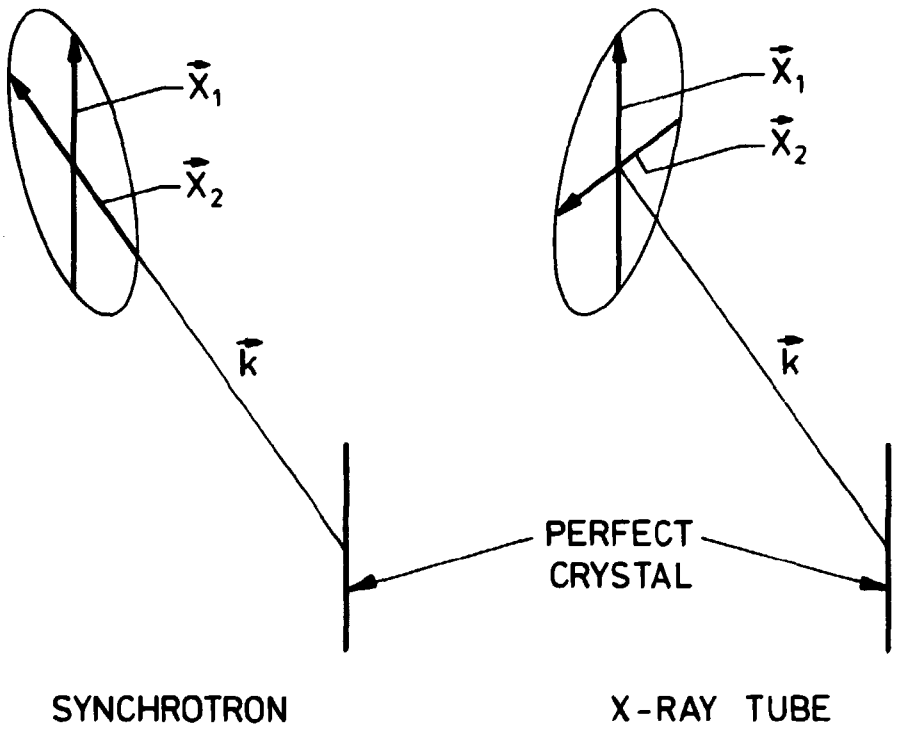

Fig. 4.3. The conjugate diameters $\vec{x}_1$ & $\vec{x}_2$ at the synchrotron and at the rotating anode.

Concerning the difference between the two sources it is interesting to notice that if one transforms the $\vec{X}_{1,syn}$, $\vec{X}_{2,syn}$-set of conjugate diameters to a $\vec{X}_{1,syn}$, $\vec{X}_{2,syn}$-set, where $\vec{X}_{2,syn} \perp \vec{k}$ just like $\vec{X}_{2,rot.anode} \perp \vec{k}$, one finds, by using the formulae in Appendix B, that <u>if $\sigma_0^2 >> \sigma_D^2$</u>:

$$X'_{1,syn} = C \cdot \frac{k\sigma_0}{\sin\theta_M} \quad ; \quad \vec{X}_1 \text{ parallel to scatt. planes}$$

$$X'_{2,syn} = C \cdot k\sigma_D \quad ; \quad \vec{X}_2 \perp \vec{k}$$

or exactly the same as at the rotating anode. The only difference is that $\sigma_{k-s}/\cot\theta_M$ is substituted with σ_0. This result tells us that if σ_D represents the most narrow collimation in the whole set-up, then the two sets of conjugate diameters are alike except that σ_0 plays the role of $\sigma_{k-s}/\cot\theta_M$ and vice versa. This is a perfectly reasonable and expected result.

For the analyzer crystal, the analogue of σ_0 is σ_4 and the analogue of σ_{k-s} is the energy discrimination of the detector $\equiv \sigma_{k-d}$, where subscript -d refers to <u>d</u>etector. Thus, for a scintillation detector one has:

$$\sigma_{k-d}^2 >> \sigma_D^2 \quad \text{and} \quad \sigma_{3,4}^2 >> \sigma_D^2$$

which in accordance with the above gives the conjugate diameters $\vec{X}_3$, $\vec{X}_4$ or X'_3, X'_4 for the analyzer crystal, where:

$$X_3 = \text{"}\infty\text{"} \text{ (or rather } X_3 >> X_{1,2,4}) \quad ; \quad \vec{X}_3 \text{ is parallel to scatt. planes}$$

$$X_4 = C \cdot k\sigma_D \cdot \cot\theta_M \quad ; \quad \vec{X}_4 \text{ is along } \vec{k}$$

or equivalently:

$\vec{x}_3'$ = "-" (see above) ; $\vec{x}_3'$ is parallel to scatt. planes

$\vec{x}_4' = C \cdot \vec{k} \cdot \vec{\sigma}_D$; $\vec{x}_4' \perp \vec{k}$

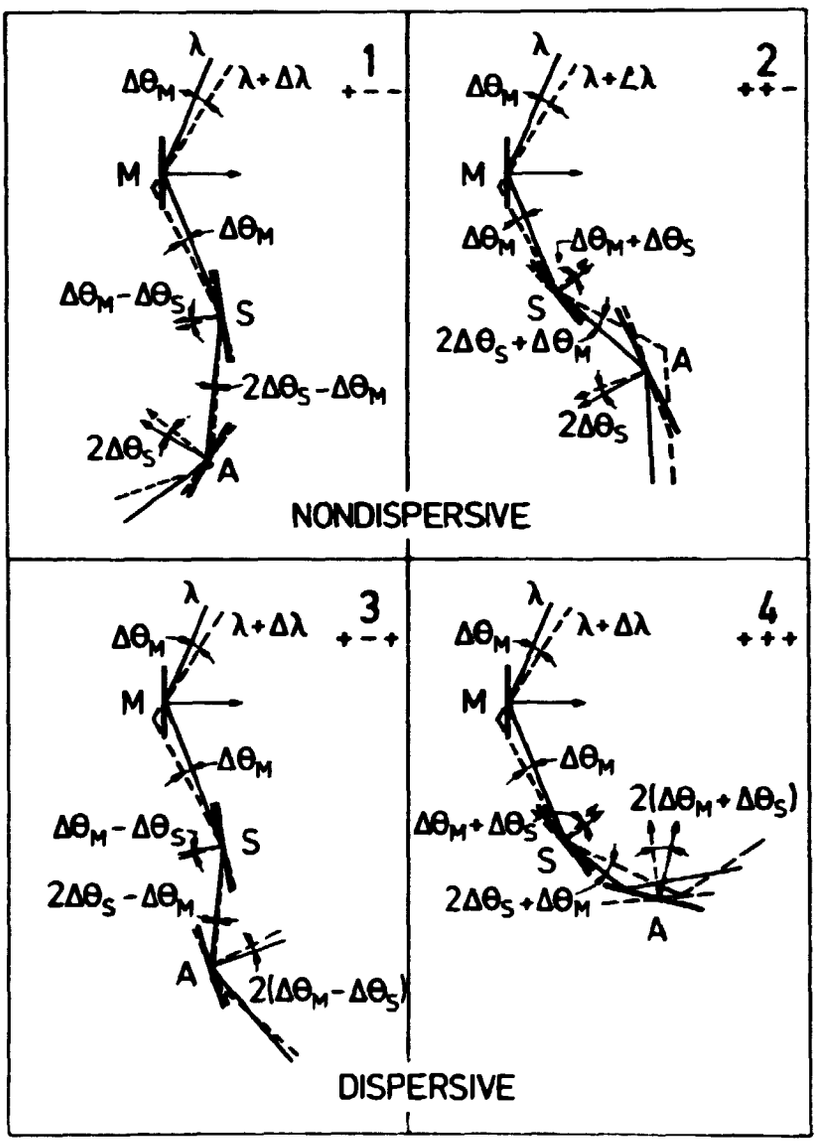

Fig. 4.4. The four different configurations of the spectrometer.

The orientation of the two ellipses, the X_1, X_2- and X_3, X_4-ellipses, relative to each other is determined by the configuration of the triple-axis spectrometer. There are four different configurations of the spectrometer. These are shown in Figure 4.4. 1 & 2 will be called nondispersive or parallel set-ups and 3 & 4 will be called dispersive- or antiparallel set-ups. For each configuration two rays are shown Bragg reflected in M, S, and A. For these reflections it is assumed that $\sigma_D = 0$. This uniquely determines how the sample and analyzer must be rotated in order to allow the ray of wavelength $\lambda+\Delta\lambda$ to be transmitted through the system, and evidently $\Delta\theta_M$ and $\Delta\theta_S$ is related to $\Delta\lambda$, θ_S and θ_M by: $\Delta\theta_M = (\Delta\lambda/\lambda)\cdot\tan\theta_M$; $\Delta\theta_S = (\Delta\lambda/\lambda)\cdot\tan\theta_S$ or $\Delta\theta_S = \tan\theta_S = \tan\theta_S/\tan\theta_M\cdot\Delta\theta_M$. The in-plane resolution will, apart from X_1, X_2, X_3, X_4, also depend on which set-up is chosen.

4.4. Combination of the two resolution ellipse in the synchrotron case

The two resolution ellipses must be combined under the condition of elastic scattering in the sample and it is straightforward, though somewhat lengthy, to combine the two resolution ellipses. Therefore, the detailed combination is derived in Appendix D in the synchrotron case, where general formulae for the in-plane resolution are given. It is a simple matter to carry over the result to the rotating anode case. In fact, as we have seen, if $\sigma_{k-s}^2 >> \sigma_D^2$ at the rotating anode, the results are readily applicable if σ_0 for the synchrotron is substituted with $\sigma_{k-s}/\cot\theta_M$ for the rotating anode. The result is expressed in terms of the two conjugate diameters Y_1 and Y_2 and angles α and δ (see Figure 4.5).

As expected, the resolution function depends only on θ_S, θ_M, σ_0, σ_D and the set-up that is chosen. It is easy to derive expression for Y_1, Y_2, α & δ in a number of limits, from the general formulae of Appendix D. Among the interesting limiting cases at the synchrotron are the ones in Table 4.3. Since one often deals with the limit $\sigma_0^2 >> \sigma_D^2$ in practice, I have concentrated on

this. For example, at DORIS σ_0 = 4 mm/20 m = 0.2 mrad ~ 11 mdeg (see next chapter) and $\sigma_{Si(111)}$ = 2 mdeg.

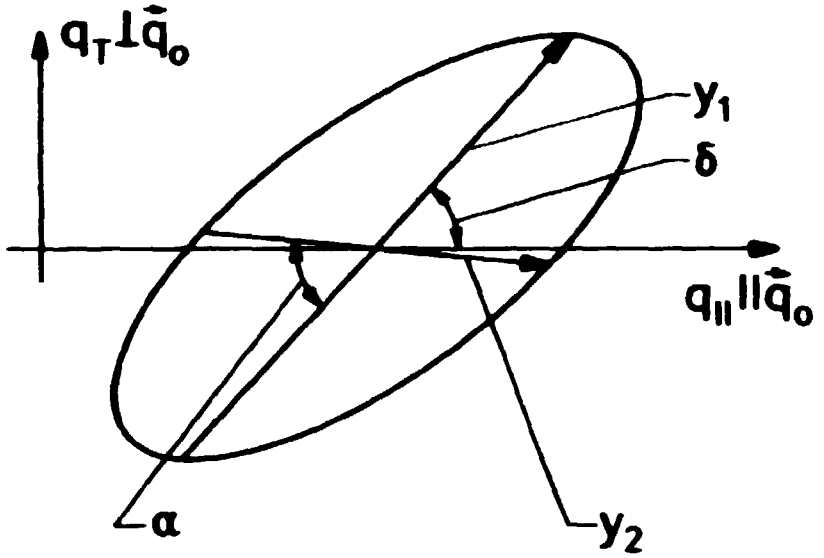

Fig. 4.5. A schematic drawing of the in-plane resolution ellipse. The conjugate diameters $\vec{Y}_1$, $\vec{Y}_2$, δ ≡ the angle from $\vec{q}_o$ to $\vec{Y}_1$ going counterclockwise and α ≡ the angle from $\vec{Y}_1$ to $\vec{Y}_2$ going counterclockwise, determines the ellipse relative to $\vec{q}_o$.

It is obvious from Table 4.3 that one will choose one of the two non-dispersive set-ups if $\theta_s \ll \theta_M$, and only if $\theta_s = \theta_M$ will one choose the +-+ configuration.

In the case of the liquid crystal set-up, where $\theta_s \ll \theta_M$ and where $\theta_M \ll \pi/2$ for Si(111/220) and Cu-kα-radiation, a rather good approximation to R_i can be obtained by neglecting the lack of parallelism of Y_1 with the $q_\parallel$-axis. In this case R_i can be written:

$$R_i = R_\parallel(q_\parallel) \cdot R_T(q_T)$$

Table 4.3. Interesting limiting cases of the resolution ellipse. $\vec{Y}_1$ & $\vec{Y}_2$ are the conjugate diameters of the resolution ellipse. δ = angle from $\vec{q}_o$ to $\vec{Y}_1$ going counterclockwise. α = angle from $\vec{Y}_2$ to $\vec{Y}_1$ going counterclockwise. k is the wavevector and $C = 2\cdot\sqrt{2\cdot\ell n2}$.

Conf.	limit	Y_1^2	Y_2^2	α	δ
+-- ~ 1	$\sigma_0^2 >> \sigma_D^2$ $\theta_s << \theta_M$	$(2Ck\cdot\sigma_0 \frac{\sin\theta_s}{\sin\theta_M})^2$	$2\cdot(C\cdot k\sigma_D)^2$	θ_M	θ_M
++- ~ 2	- " -	$(2C\cdot k\sigma_0 \frac{\sin\theta_s}{\sin\theta_M})^2$	$2\cdot(C\cdot k\cdot\sigma_D)^2$	$\P-\theta_M$	$\P-\theta_M$
+-+ ~ 3	$\sigma_0^2 >> \sigma_D^2$ $\theta_s \approx \theta_M$	$(C\cdot k\cdot\sigma_D)^2$	$(C\cdot k\cdot\sigma_D)^2$	$2\theta_s$	θ_s
+++ ~ 4	$\sigma_0^2 >> \sigma_D^2$ $\theta_s << \theta_M$	$(2Ck\sigma_0)^2$	0	irrelevant	0

where $R_T(q_T)$ is a delta function and $R_\parallel(q_\parallel)$ is a Gaussian with width Y given by:

$$Y^2 = 2(C\cdot k\sigma_D)^2 + (2Ck\sigma_0 \frac{\sin\theta_s}{\sin\theta_M})^2 \quad ; \quad C = 2\sqrt{2\ell n2}$$

$R_\parallel$ then corresponds to a convolution of the direct beam profile, the first term, with the $\Delta\lambda/\lambda$-contribution (as it will be called), the second term.

Since $\theta_M << \pi/2$ the second term can further be approximated by:

$$(2\cdot C\cdot\sigma_0\cdot k \frac{\sin\theta_s}{\sin\theta_M})^2 = (2\Delta\theta_M\cdot k\cdot \frac{\tan\theta_s}{\tan\theta_M})^2 = (2\Delta\theta_s k)^2$$

where $\Delta\theta_s$ and $\Delta\theta_M$ are defined in Figure 4.4. and $\Delta\theta_M$ is set to be $C\cdot\sigma_0$, or in words, $\Delta\theta_M$ is the FWHM of the angular acceptance

of the slit system before the monochromator. As mentioned earlier, if $\sigma^2_{k-s} >> \sigma^2_D$ for the rotating anode, one can subsitute σ_0 with $\sigma_{k-s}/\cot\theta_M$ in the above formula. Doing so gives the same result as above, with $\Delta\theta_M = \mathrm{tg}\theta_M \cdot (\Delta\lambda/\lambda)_{FWHM}$, where $(\Delta\lambda/\lambda)_{FWHM}$ is the FWHM-λ content of the specific anode line.

Within the above-mentioned approximation, R* can be measured. This can be seen from Figure 4.4. If the sample is left out in either of configurations 1) or 2), scanning the analyzer-crystals will give the direct beam profile. The λ-content will <u>not</u> broaden this curve. Leaving out the sample in any of 3) or 4) will give $\Delta\theta_M$(FWHM), or equivalently at the rotating anode, $(\Delta\lambda/\lambda)_{FWHM}$ provided that $(2\cdot\Delta\theta_M(\mathrm{FWHM}))^2 >>$ (D.B.-FWHM)^2 or equivalently at the rotating anode $(2\cdot\Delta\lambda/\lambda(\mathrm{FWHM})\ \tan(\theta_M)\cdot 180/\pi)^2$ >> (D.B.-FWHM)^2. If $\Delta\theta_M$(FWHM) has been measured in this way, the line distribution ℓ from Appendix D, can be obtained by scaling the abscissa with the ratio $\tan\theta_S/\tan\theta_M$. If $2\Delta\theta_S >>$ D.B.-FWHM one may directly measure the line distribution. This <u>cannot</u> be done with liquid crystal samples since $2\Delta\theta_S \sim$ D.B.-FWHM: To check the scaling procedure[3] one can put in a perfect crystal, as sample, with a Bragg angle fulfiling the condition that $(2\Delta\theta_{S,test})^2 >>$ (D.B.-FWHM)^2. One can then scale the abscissa of these data with the ratio $\tan\theta_S/\tan\theta_{S,test}$, which is the procedure normally used in case of the liquid crystal set-up[2].

These detailed measurements may reveal non-Gaussian behaviour of the two elements contribiting to R_i. Depending on the wanted degree of accuracy, it is reasonable to assume that it is still a good approximation to represent R* by a convolution of the two contributions (the direct beam profile and $\Delta\lambda/\lambda$-line distribution).

4.5. The out-of-plane resolution

The out-of-plane resolution is not correlated to the in-plane resolution and can be calculated independently. $R_v(q'_v, q_o)$ is determined by the out-of-plane divergence of the beam on either side of the sample. This divergence can be calculated as shown

in Figure 4.6, that is, in case the divergence is determined by two slits only. If the trapezoidal curve in Figure 4.6 is approximated with a Gaussian of FWHM = $\sigma_{i,v}$ for the incoming side and a FWHM = $\sigma_{o,v}$ for the outgoing side, then the out-of-plane resolution function is a convolution of two Gaussians, yielding a Gaussian of FWHM = $\sqrt{\sigma_{i,v}^2+\sigma_{o,v}^2}$.

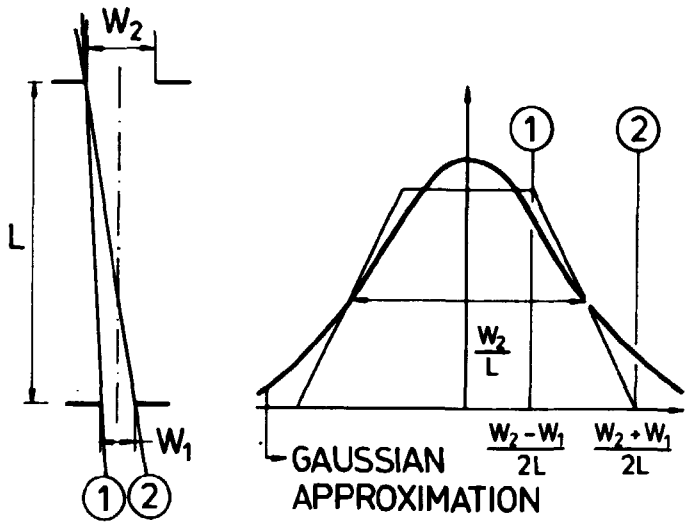

Fig. 4.6. The angular acceptance of a two-slit system. Note that the FWHM is given by the largest slit only.

The resolution function is now determined in terms of the in-plane resolution function R_i and the out-of-plane resolution function R_o. One more contribution may be added to the total resolution function if the sample is imperfect. The effect of mosaicity in the sample is to add an extra component to the in-plane resolution in the transverse direction and to add an extra one to the out-of-plane resolution as outlined in Appendix E.

4.6. The resolution for a typical liquid crystal set-up

To make the previous considerations concrete one can take one of the two nondispersive set-ups at the rotating anode and put in a liquid crystal sample, like 8OCB (q_o = 0.197 $Å^{-1}$), and try to

see what resolution this will give if the radiation is $CuK_{\alpha 1}$-radiation and M ≡ A = Si(220); m = 3. For this set-up, the following conditions approximately apply:

$$\sigma^2_{k-s} >> \sigma^2_D \; ; \; \theta_S << \theta_M << \frac{\pi}{2}$$

From Appendix E and Section 4.4 it is clear that the transverse in-plane resolution is given by the mosaicity and for intensity reasons one will have to open up the vertical slits to get a large vertical resolution R_v. $R_\parallel$ is, as noted earlier, approximately a convolution of the direct beam profile and the $(\Delta\lambda/\lambda)$-contribution. For a realistic calculation the mosaicity M_T is assumed to be Gaussian with FWHM = 0.00515 $Å^{-1}$ and R_v is assumed to be Gaussian with FWHM = 0.00807 $Å^{-1}$. (see Table 4.4, where functions and parameters are given for the resolution function at q_o and $2q_o$.) The longitudinal resolution function $R_\parallel$ has been experimentally measured by performing a direct beam profile scan, putting in a perfect Si(111)-crystal as test-sample, and rotating the analyzer crystal. The Si(111)-crystal was rotated along with the analyzer-crystal, the ratio of rotations being $-2\,tg\theta_{Si(111)}/(tg\theta_{Si(220)}-tg\theta_{Si(111)})$ (see Figure 4.4). In Figure 4.7 the scaled Si(111)-data numerically convoluted with the direct beam profile, is compared with two analytic curves. The sharpest one approximates the experimental data well down to ~ 10% of the peak-value. This curve is simply the convolution of two Gaussians, one with the width ≡ α of the direct beam profile and one with the width ≡ β of the scaled Si(111)-curve. The convolution gives a Gaussian with width = $\sqrt{\alpha^2+\beta^2}$. The second curve, which approximates the experimental points quite well down to 10^{-3} of the peak-value is a convolution of a Gaussian with the width of the direct beam profile and an exponential which describes very well the scaled Si(111)-curve. The parameters are given in Table 4.4. Figure 4.8 shows the result and two components of this convolution, together with experimental points. Clearly the exponential wings of $R_\parallel$ seems to be a property of the natural lineshape of the $CuK_{\alpha 1}$-line. Theoretically[4] the lineshape should have the form:

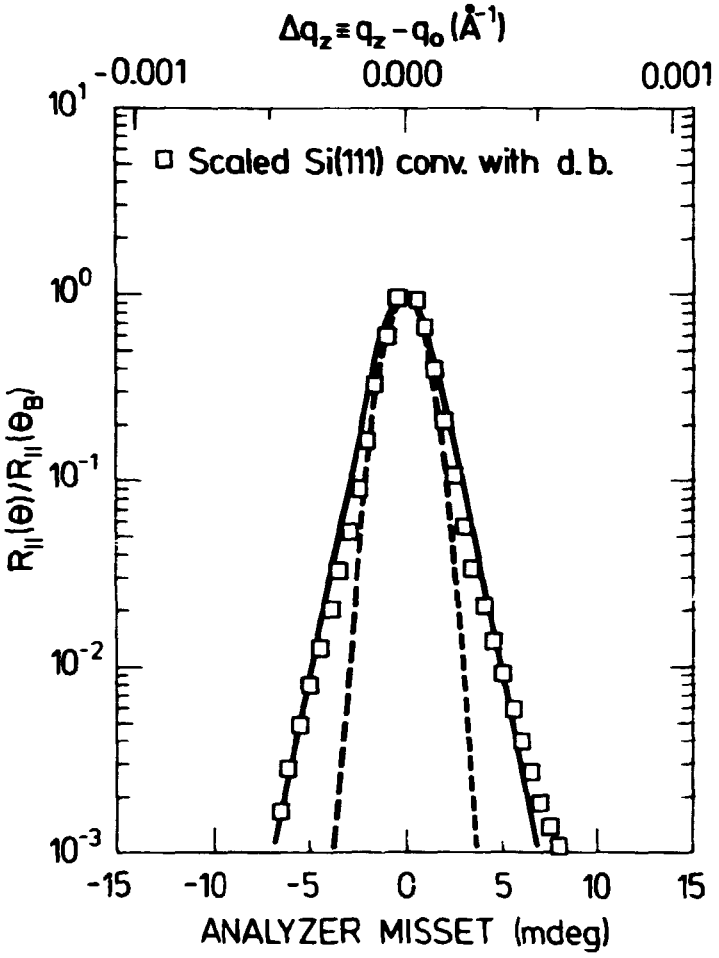

Fig. 4.7. The longitudinal resolution function. The points are the direct beam profile convoluted, numerically, with the scaled Si(111)-data, giving the ($\Delta\lambda/\lambda$)-contribution. The two curves are analytical approximations. See text.

$$I(\lambda) = \frac{a}{b+\left(\frac{1}{\lambda} + \frac{1}{\lambda_o}\right)^2}$$

where λ_o is the nominal $CuK_{\alpha 1}$ wavelength and a & b are constants. With (2·FWHM of the unscaled Si(111)-data)^2 >> (D.B.-FWHM of the two Si(220); m = 3-crystals)^2 the unscaled (and scaled) Si(111)-data should be a Lorentzian intensity distribution versus the offset-angle $\Delta\theta$:

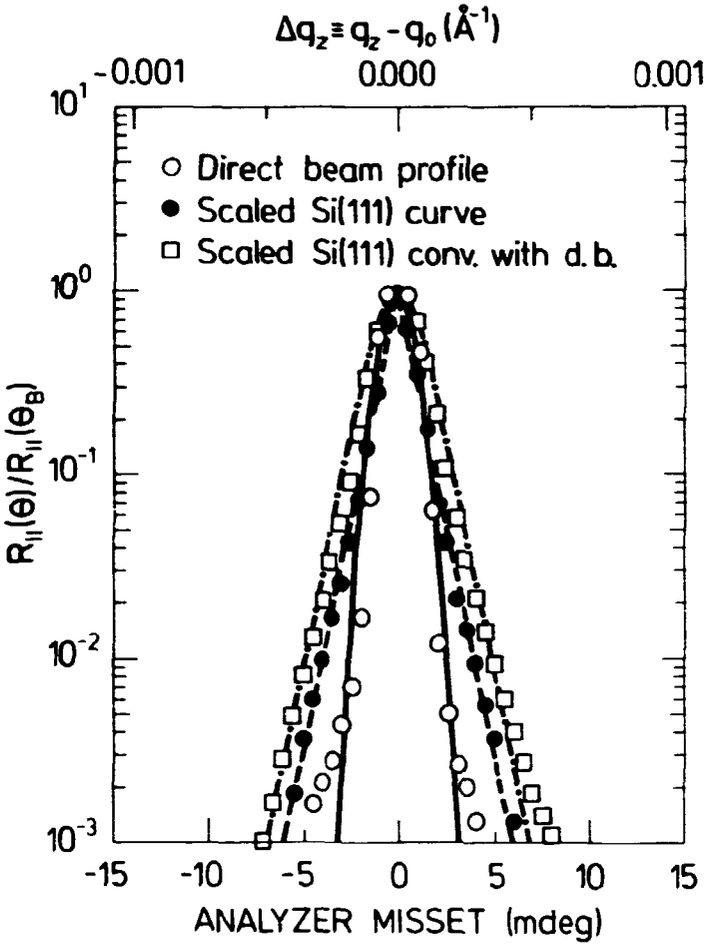

Fig. 4.8. The result and the two components of the longitudinal resolution function. Measured points and analytic curves. Parameters for the analytic curves are given in Table 4.4.

$$I(\Delta\theta) = \frac{4\pi^2 a}{4\pi^2 b + (k-k_o)^2}$$

$$= \frac{a}{b + \dfrac{\cot^2\theta_M}{\lambda_o^2} \cdot (\Delta\theta)^2} \qquad ; \; \Delta k \equiv k-k_o = k_o \cdot \cot\theta_M \Delta\theta$$

$$\Delta\theta = \theta - \theta_M$$

The reason for the apparent exponential lineshape is unclear. An attempt to fit the unscaled Si(111)-data to a Lorentzian is unsuccesful. The goodness of fit parameter $\chi^2 = 2.9 \cdot 10^4$.

It is often unnecessary to know the resolution function accurately down to 10^{-3} of the peak-value. In these cases one can use the Gaussian approximation. At the synchrotron the $(\Delta\lambda/\lambda)$-contribution will probably not have the exponential wings and in this case the Gaussian approximation may be better than at the rotating anode.

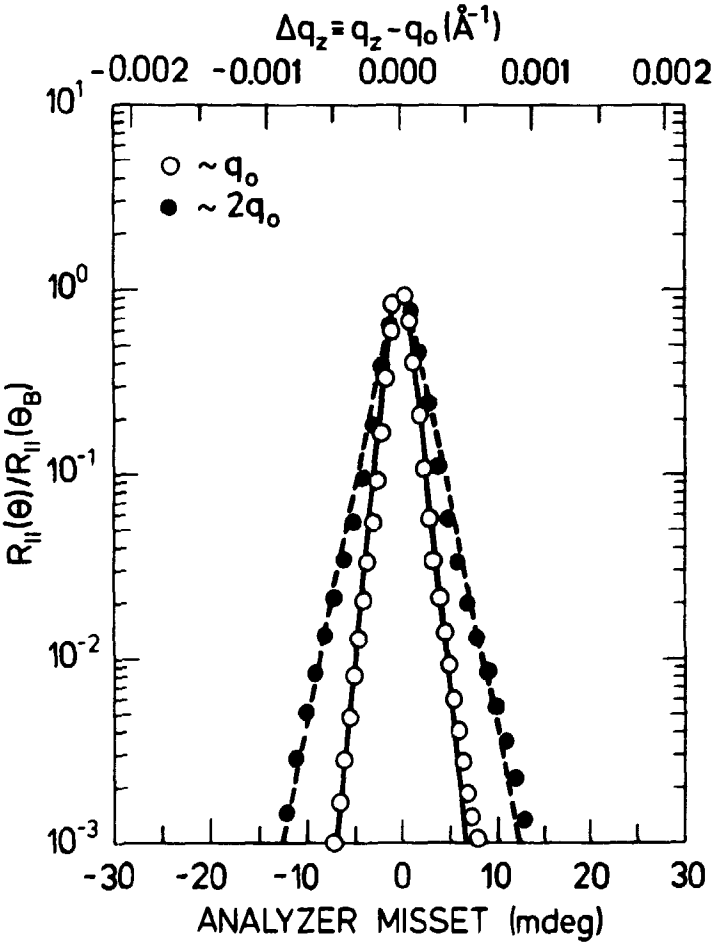

Fig. 4.9. Experimental points and analytical curves for the longitudinal resolution function at $\vec{q} \approx \vec{q}_o$ and $\vec{q} \approx 2\vec{q}_o$. Filles points are for $\vec{q} \approx 2\vec{q}_o$.

Figure 4.9 shows R= at q_o and at $2q_o$. Experimental data are shown together with the analytic curves used to deconvolute exp. data.

The typical functions and parameters from Table 4.4 are the ones used to calculate experimental line shapes in Chapter 8. This calculation has not used (4.1) directly in the numerical convolution. This is so because no analytical form of S(q) is known, but the Fourier transform G(r) is known (Appendix A). Therefore, the convolution was performed in real space, using the folding theorem, followed by a Fourier transformation (see also Ref.[3]).

Table 4.4. A typical resolution for high-solution liquid crystal X-ray experiments at the rotating anode.

Res.fct.	ANALYTICAL FORM		Parameters	FWHM (in $\vec{q}$-space)
	$q \sim q_o$	$q \sim 2q_o$		
Transverse R_T	$e^{-q_T^2/2\sigma_T^2}$	$e^{-q_T^2/2\sigma_T^2}$	$\sigma_T = 0.0111 \cdot q_o = 2.1867 \cdot 10^{-3}$ Å^{-1}	$2 \cdot \sqrt{2 \ln 2} \cdot \sigma_T = 0.00515$ Å
Vertical R_V	$e^{-q_V^2/2\sigma_V^2}$	$e^{-q_V^2/2\sigma_V^2}$	$\sigma_V = 0.0174 \cdot q_o = 3.4278 \cdot 10^{-3}$ Å^{-1}	$2 \cdot \sqrt{2 \ln 2} \cdot \sigma_V = 0.00807$ Å^{-1}
Longitudinal $R_\parallel$	convolution of: $e^{-q_\parallel^2/2\sigma_\parallel^2}$ and $e^{-\sqrt{2}\lvert q_\parallel \rvert / \sigma_\parallel \cdot \sigma_1}$	convolution of: $e^{-q_\parallel^2/2\sigma_\parallel^2}$ and $e^{-\sqrt{2}\lvert q_\parallel \rvert / \sigma_\parallel \cdot \sigma_2}$	$\sigma_\parallel = 5.9888 \cdot 10^{-5}$ Å^{-1} $\sigma_1 = 1.446$ $\sigma_2 = 2.89$	$\sim \vec{q}_o$: $2.03 \cdot 10^{-4}$ Å^{-1} $\sim 2\vec{q}_o$: $2.50 \cdot 10^{-4}$ Å^{-1}

4.7. The two-axis spectrometer with P.S.D.

The foregoing discussion has dealt with the X-ray spectrometer in the horizontal triple-axis mode. Another high-resolution set-up can be obtained by the use of a position-sensitive detector (P.S.D.). The Physics Department at Risø bought a P.S.D. a few years ago and it has been used mainly to study the adsorption of two-dimensional layers of gases on graphite-substrates. With the P.S.D. the spectrometer operates essentially as a two-axis spectrometer, with a monochromator part that may be either one crystal or a set of crystals and where the scattered radiation is detected in a certain angular range by the P.S.D. The collimation between the sample and P.S.D. is determined by the resolution of the detector-wire (typically < 100 μ), the distance between the sample and the P.S.D. and the slit-system after the sample.

The in-plane resolution one obtains for this set-up can be found using the standard procedure for the two-axis spectrometer, which in short involves the following steps:

1) Construct the X_1, X_2-set of conjugate diameters for the monochromator part. For perfect crystal(s) the method in Figure 4.2 must be used. For crystals with a mosaicity >> Darwin width, the method in reference[2] can be used.
2) Transform this resolution-ellipse to the end of $\vec{q}_0$, under the assumption of infinitely good collimation between the sample and the detector. (see Reference[2]).
3) The effect of a finite collimation of the detecting system can then be included simply by the use of transformation of conjugate diameters and the rule of sum-of-squares for Gaussian distributions. (see Reference[2]).

The out-of-plane resolution is determined similarly to the triple-axis case.

REFERENCES

1) H.B. Møller, M. Nielsen (1969) Acta Crystallogr. A, 25, 547.
2) J. Als-Nielsen (1980) Resolution in diffraction. An outline of the method of conjugate diameters. Lecturenotes from a summerschool on X-ray scattering with synchrotron radiation. 7-17 Sept. 1980 in Vienna.
3) J. Als-Nielsen, J.D. Litster, R.J. Birgenau, M. Kaplan, C.R. Safinya, A. Lindegaard-Andersen and S. Mathiesen (1980) Phys. Rev. B, 22, 312.
4) A.H. Compton and S.K. Allison (1935) X-rays in theory and experiment. 2nd ed. (Van Nostrand, New York) 842 p.

5. TRIPLE-AXIS X-RAY DIFFRACTION AT THE SYNCHROTRON; THE TECHNIQUES AND QUALITATIVE AND EXPERIMENTAL COMPARISONS WITH THE ROTATING ANODE

The radiation emitted by accelerated electrons or positrons with ultrarelativistic velocities in a storage ring is well suited to the study of condensed matter. The wavelength of the radiation extends from the visible to the hard X-ray region. One of the dedicated synchrotron laboratories is HASYLAB in Hamburg. This laboratory uses the radiation from the DORIS storage ring, which is part of the hierarchy of electron/positron rings at the high-energy physics center DESY (Deutsches Elektronen Synkrotron).

This chapter will describe the techniques employed when working with the triple-axis spectrometer at DORIS and further describes the properties of the synchrotron radiation and compares them, partly experimentally, with a conventional source, a 12-kW rotating anode.

5.1. General properties of synchrotron radiation

When electron/positrons, with ultra-relativistic energy E, traverse a circular trajectory, they emit radiation tangential to the orbit. The electron/positron is confined to the circular orbit of radius R by a magnetic field B perpendicular to the horizontal orbit plane. Figure 5.1 shows a schematic drawing of the set-up.

If the electron beam is perfectly confined to the orbit plane, the vertical collimation (FWHM) of radiation with wavelength λ is given by:

$$\Delta\psi = 2 \cdot \sqrt{2\ln 2} \cdot \sigma_\gamma(\lambda) = 2\sqrt{2\ln 2} \cdot \frac{0.289}{E(\mathrm{GeV})} \cdot \left(\frac{\lambda}{\lambda_c}\right)^{0.425} \text{ mrad} \qquad (5.1)$$

$$\Delta\Psi \approx \frac{0.5\,\mathrm{MeV}}{E} \qquad \text{(E-electron energy)}$$

Ex.: E = 5GeV

$\Delta\Psi = 10^{-4}$ rad = 0.1mrad

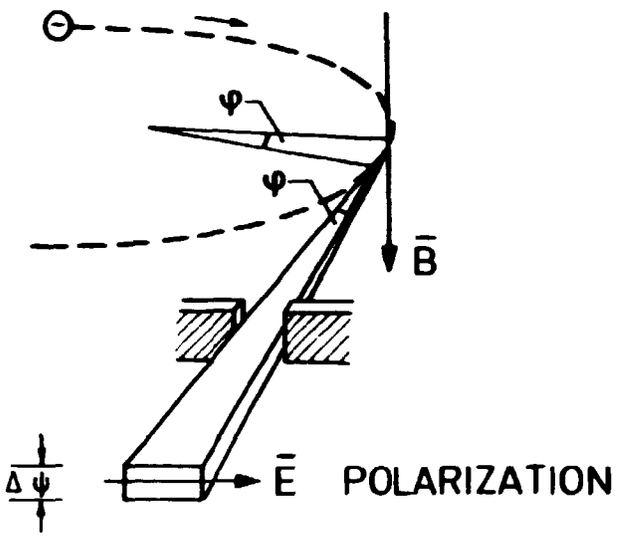

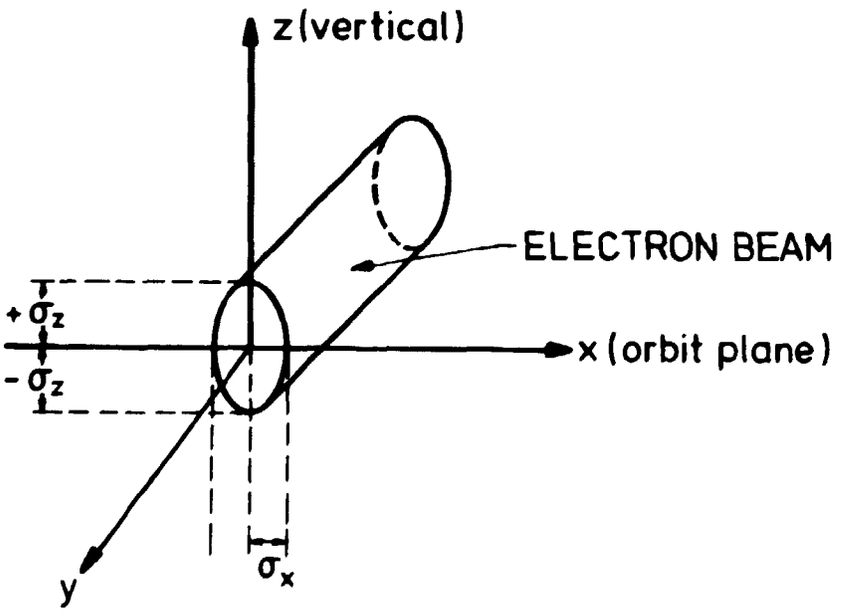

Fig. 5.1. The synchrotron radiation.

where the critical wavelength λ_c is given by:

$$\lambda_c = 5.59 \cdot R(m) \cdot \frac{1}{[E(GeV)]^3} \text{ Å} \; ; \; R \text{ is orbit radius} \tag{5.2}$$

The spectral intensity distribution from the storage ring can be calculated exactly from theory, and the result can be expressed in terms of simple, universal, functions. The function relating to a typical horizontal triple-axis set-up at the synchrotron is:

$N(\lambda)$ = number of photons/sec./0.1% energy bandwidth/mrad horizontal

$$= 2.236 \cdot 10^{10} \cdot I \cdot E \cdot G\left(\frac{\lambda_c}{\lambda}\right)^{2)} \tag{5.3}$$

where I is the beam current in mA and E is the electron energy in GeV, and where $G(\lambda_c/\lambda)$ is given by:

$$G\left(\frac{\lambda_c}{\lambda}\right) = 1.1 \cdot \left(\frac{\lambda_c}{\lambda}\right) \int_{\lambda_c/\lambda}^{\infty} K_{5/3}(x)dx \; ; \; K_{5/3} \text{ is the modified Bessel function of degree = 5/3.} \tag{5.4}$$

Figure 5.2 shows calculations[1] of $N(\lambda)$ for DORIS, NSLS (National Synchrotron Light Source-design, Brookhaven, U.S.A.); ESRF (European Synchrotron Radiation Facility design).

The electrons/positrons are not completely confined to the average orbit plane. They perform oscillations in and out of the average orbit plane; furthermore, the electron beam is not infinitely thin, but has a spatial distribution. This is shown in Figure 5.1, where Gaussian distributions are assumed in the x and z-directions with $FWHM_{x,z} = 2 \cdot \sqrt{2 \ln 2} \cdot \sigma_{x,z}$. The above-mentioned oscillations give rise to an electron beam divergence, characterized by the standard deviation σ'_z. The full divergence of the X-ray beam in the vertical plane is then given by:

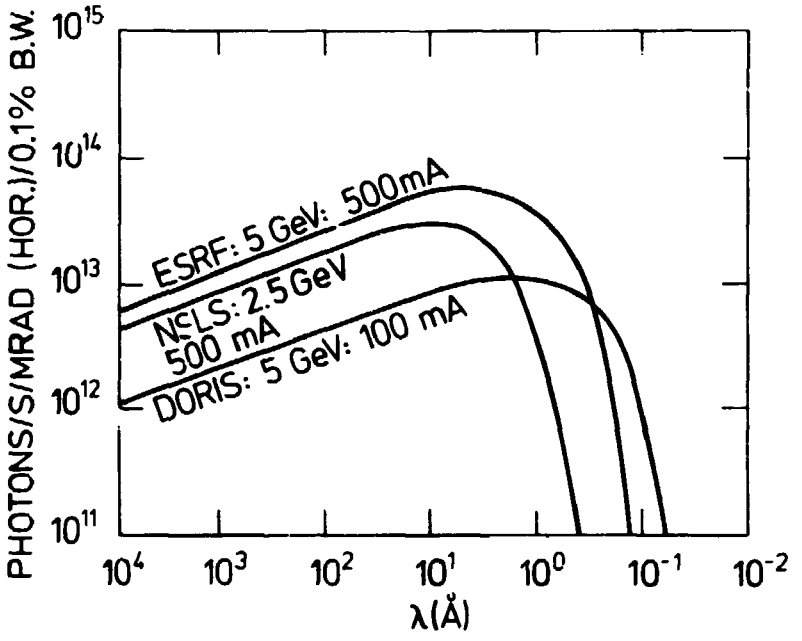

Fig. 5.2. N(λ) for DORIS, NSLS and ESRF.

$$\sigma_{z,tot}^2 = \sigma_\gamma^2 + \sigma_z'^2 \qquad (5.5)$$

At DORIS $2 \cdot \sqrt{2 \ell n 2} \cdot \sigma_{z,tot}$ is ≈ 0.3 mrad for E ≈ 3 GeV.

If one assumes that the intensity distribution in the x-direction is uniform within a range $2 \cdot \sqrt{2 \ell n 2} \cdot \sigma_x$ and zero outside, then the beam divergence in the horizontal direction is determined by the slit width before the experimental apparatus or $2 \cdot \sqrt{2 \ell n 2} \cdot \sigma_x$, whichever is the larger (see Figure 5.5 in Chapter 4). σ_x is whown in Table 5.1 for DORIS, NSLS, and ESRF. During a dedicated running period, the energy of the electrons/positrons is fixed, while the current gradually decays. This decay is due to collisions between electrons/positrons and residual gas molecules in the ring. The lifetime of the current at a storage ring like DORIS can be as high as ~ 12 hours under optimal conditions, but normally new electrons/positrons are injected after 3-4 hours, thus maintaining a high intensity level. After a new filling of the ring the source might have moved, both in the horizontal and vertical directions. For the DORIS storage ring a typical energy

is 3.3 GeV with the current, typically, decaying from 100 mA to 20 mA.

In Table 5.1. DORIS is compared to an NSLS- and ESRF-design.

Table 5.1. DORIS-, NSLS- and RDTG-parameters.[1)]

	DORIS	ESRF	NSLS
$2\cdot\sqrt{2\ell n2}\cdot\sigma_x$	4.0 mm	0.49 mm	0.94 mm
$2\cdot\sqrt{2\ell n2}\cdot\sigma_z$	2.8 mm	0.28 mm	0.235 mm
ELECTRON-BEAM DIVERGENCE $2\cdot\sqrt{2\ell n2}\cdot\sigma_z'$	0.26 mrad	0.021 mrad	0.0235 mrad
R(radius)	12.12 m	22.4 m	6.93 m
MAX. CURRENT	100 mA	500 mA	500 mA
MAX. ENERGY	5 GeV	5 GeV	2.5 GeV

5.2. General properties of the rotating-anode radiation

The radiation generated by electrons striking a metal anode, like Cu, consists of the well-known line spectrum superimposed on a low-intensity bremsstrahlung. The bremsstrahlung comes from the deceleration of the electrons in the target. The line spectrum is generated by a process where an electron has enough energy to remove, say, a K-electron from a Cu-atom whereupon an L-electron jumps to the K-shell. This latter process is followed by the generation of X-rays with the characteristic $CuK\alpha_1$ and $CuK\alpha_2$ lines. Typical anode materials are Cu and Mo. The origin of the $K\alpha_1$ and the $K\alpha_2$-splitting is the spin-orbit coupling in the L-shell, which splits up into two energetically close eigen-

states, giving rise to the $K\alpha_1$- and the $K\alpha_2$-lines. The $K\alpha_1$-line is approximately two times more intense than the $K\alpha_2$[2].

The intensity from the anode is limited, in practise, by anode heating. This can be reduced by letting the anode rotate, thus distributing the heat over a larger area.

The radiation from the anode is almost completely uncollimated[2] and both the vertical and the horizontal divergence of the radiation incident on the monochromator is determined by slit widths or source dimensions (see Figure 5).

The characteristic lines from the rotating anode are not infinitely sharp but have a natural line width. For the $CuK\alpha_1$-line this is:[2]

$$(\frac{\Delta\lambda}{\lambda})Cuk\alpha_1 \approx 4 \cdot 10^{-4} \text{ (FWHM)}$$

When running properly, the rotating anode is an extremely stable source with the possibility of controlling the intensity over at least 1 decade of the full range, by varying the voltage over the anode and filament and/or varying the current from the anode to the filament.

5.3. Detection of the X-ray beam at the storage ring and rotating anode

There are a number of ways one can detect an X-ray beam. X-ray detectors are available for different purposes. Among these are scintillation detectors, solid state detectors, and position sensitive detectors. When an actual experiment is running, one of these will be used to collect data, but during alignment of the spectrometer they are not very useful. The main reason is that during alignment it is often necessary to detect very intense X-ray beams and all the detectors mentioned will either be destroyed or become saturated if the intensity gets beyond 10^4-10^5 photons/sec. To deal with this, one could use various

beam attenuators. Since it is crucial to be able to align the spectrometer at either source, fast and accurately, one can alternatively use other ways of detecting intense X-ray beams. One of these is the ion-chamber, which at the same time can be used as a beam monitor, when doing the actual experiment. The beam monitor is shown in Figure 5.3. It has been constructed by Dr. J. Als-Nielsen at Risø and used at the rotating anode and, especially at the storage ring.

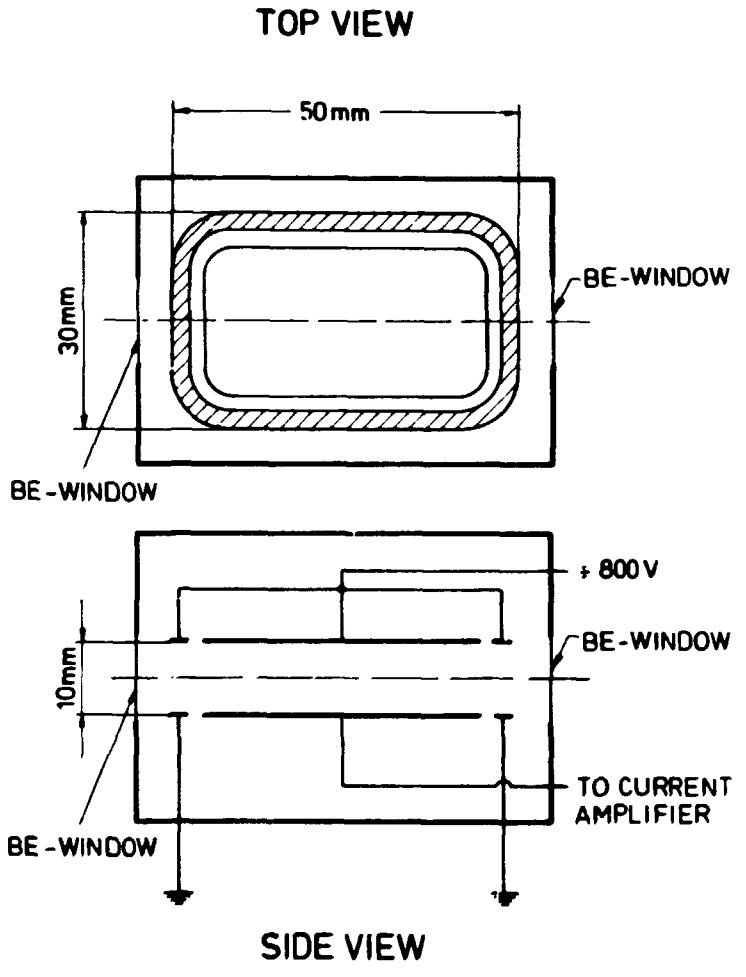

Fig. 5.3. The ion chamber. Note the outer ring, which will catch possible leak currents.[3)]

The detector is filled with gas of 90% argon and 10% methane to a pressure of 0.1 atm. If necessary, the pressure can be changed easily. An example of its use is given in Figure 5.5 and Table 5.2. The transmission of the detector is 92% for CuKα_1-radiation. The current generated in the ionization chamber is converted to a voltage by a Keithley-amplifier. The maximum gain of the amplifier is 10^{11} V/A, thus ~ 10^{-12} ampere can be detected.

Other ways of detecting intense X-ray beams employ what could be called visual detectors. Among these are: films, fluorescent screens, and X-ray sensitive paper ("green paper"). Any of these can be very helpful when aligning the spectrometer. In the direct beam from the storage ring, they will all give a signal almost immediately. The fluorescent screen will light up so brightly that a prescise determination of the beam spot is impossible due to the smearing out of the picture. At the rotating anode, both films and the fluorescent screen can detect the direct beam. The "green paper" is too insensitive to be useful at the rotating anode. In a monochromatic beam (λ = 1.542 Å) from the storage ring, where the monochromator is either a perfect Si-crystal or a perfect Ge-crystal, both the film and the fluorescent screen will show a sharp spot with well-defined edges. In the monochromatic CuKα-radiation from the rotating anode, sensitive films can be used and to some extent the fluorescent screen.

5.4. A procedure for aligning the triple-axis spectrometer at the storage ring

For a universal X-ray spectrometer it is crucial to develop techniques which can facilitate a rapid alignment of the spectrometer, especially at the storage ring where source movements during refilling of DORIS calls for the need of ways to trace the beam and perhaps realign the spectrometer rapidly. The following alignment procedure is for a triple-axis, nondispersive, elastic, X-ray experiment at the storage ring (see Figure 3.1 in Chapter 3).

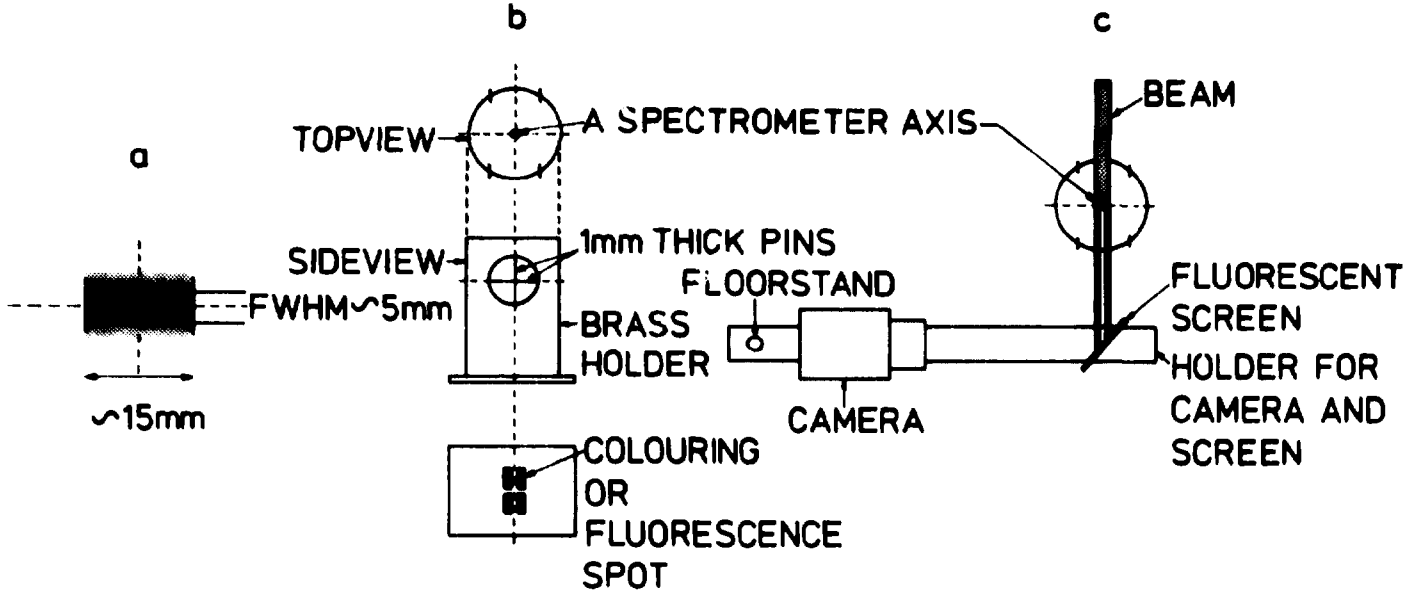

Fig. 5.4. Devices and/or techniques for aligning the spectrometer. a) The beam colouring of a X-ray sensitive paper, placed in front of the beam definer. b) The pin cross. c) The arrangement of the fluorescence screen and the camera behind the pin cross.

The direct beam from the storage ring DORIS at the spectrometer site in HASYLAB is limited in the vertical plane by its natural divergence. In the horizontal plane the beam is limited by a 10-mm wide Cu-aperture, approximately 14 meters from the source. This leads to a beam with the intensity distribution just before the beam-defining slit shown in Figure 5.4a.

This can be checked by exposing X-ray sensitive paper for ~ 10 seconds. Since the source moves every now and then, it is essential to be able to trace the beam without having to realign the whole spectrometer. For this purpose a beam-finder is installed in front of the beam-defining slit. The beam-finder is essentially four small ion-chambers, one above, one below, one to the right, and one to the left of the beam-defining slit. The beam-defining slit and the beam-finder are fixed to the monochromator axis, and the beam-defining slit and monochromator axis are aligned once and for all, so that when the current in the ion-chambers is balanced two and two, the spectrometer is in the correct position, meaning that the center of the intense, white synchrotron beam is exactly over the monochromator axis. The spectrometer can be brought into this central position by moving the spectrometer floor up or down, which can be done by remote motor control and by moving the whole spectrometer horizontally perpendicular to the beam. This is done by gliding the spectrometer along a sledge bolted to the spectrometer floor.

When the spectrometer as a whole is brought into the right position and a beam-defining slit, typically with dimensions 2-mm wide and 5-mm high, is chosen, the spectrometer is aligned by the following steps:

1) With the center of the direct beam over the monochromator axis, the next step is to direct the center of the direct beam over the sample axis or, equivalently, find the zero-position of the monochromator arm (M.A.). This may be done by placing X-ray sensitive paper after a 1 mm pin cross on the sample goniometer (see Figure 5.4b).
2) M.A. is moved to $2 \cdot \theta_M$, twice the Bragg angle of the monochromator for the chosen wavelength.

3) The monochromator crystal is set in place, rotated (M.R.) and tilted until the monochromatic beam falls over the sample axis at the correct height. This can be checked using the 1-mm pin cross and the fluorescent screen arrangement in Fig. 5.4c). The picture of the beam spot on the fluorescent screen of the TV-monitor should look exactly like the sensitive paper colouring of Figure 5.4b).
4) The zero-position of the sample arm (S.A.) can now be determined by bringing the analyzer axis into the center of the monochromatic beam. This is done in the same way as under point 3). The only difference being that in this case, the beam is fixed in space and the pin cross is moved through the beam to find the correct position, whereas under 3) the beam is moved and the pin cross is fixed.
5) The analyzer arm (A.A.), with the ion chamber as far back as possible, is scanned through the monochromatic beam to find the zero-position of A.A.
6) The analyzer arm is rotated nondispersively to $2 \cdot \theta_A$, twice the Bragg angle of the analyzer crystal, for the chosen wavelength.
7) The analyzer crystal is put in and rotated (A.R.) until the monochromatic beam is reflected into the ion chamber of the analyzer arm.
8) The analyzer crystal is tilted until the intensity in the ion chamber is maximised.

Unfortunately, 7) and 8) are coupled, since the narrow Darwin-width of the perfect crystals makes it impossible, with the present goniometer, to tilt the crystal and at the same time maintain the position of the rotation to within 1 mdeg. The solution to this is to scan A.R. for a number of settings of the tilt of the analyzer crystal, thus finding the position of the tilt which gives maximum intensity. The spectrometer is aligned, and the sample can be placed in position. The alignment procedure at the rotating anode is similar, but films and ion chamber would be used instead of fluorescent paper. The full alignment can be completed in ~ 20 minutes.

5.5. Measurement of properties of the synchrotron radiation and rotating-anode radiation relevant to triple-axis X-ray diffraction

The properties measured and compared in this section are related specifically to the demands of a triple-axis X-ray spectrometer. In X-ray diffraction experiments it is crucial to obtain a high resolution of the spectrometer, while maintaining the necessary intensity.

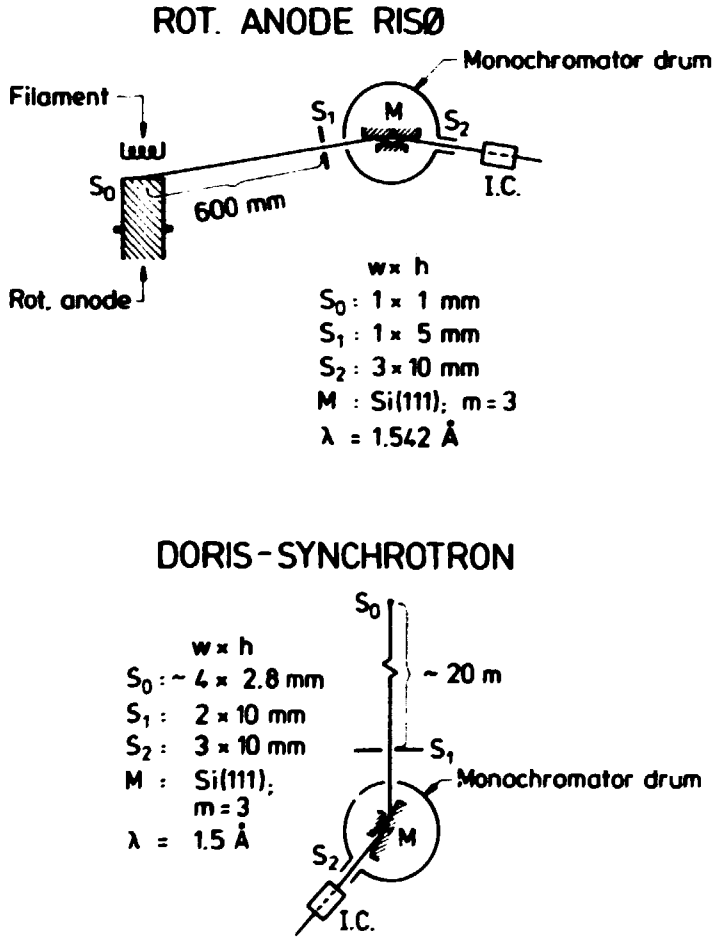

Fig. 5.5. The experimental set-up at the rotating anode and at the synchrotron referring to Table 5.2.

Table 5.2. Intensity comparison between the rotating anode and the synchrotron source. The set-ups are shown in Figure 5. The intensity is ~ 500 times larger at the synchrotron than at the rotating anode. Furthermore, the vertical and horizontal beam divergence is reduced by a factor ~ 10. Note the difference in beam size.

	ROT.ANODE	DORIS
Measured $(\frac{\Delta\lambda}{\lambda})$ FWHM	$3.1 \cdot 10^{-4}$ [4]	$1.06 \cdot 10^{-3}$
Horizontal beam divergence (FWHM)	$\frac{1}{600}$ = 1.4 mrad	$\frac{4}{20}$ mrad = 0.2 mrad
Vertical beam divergence (FWHM)	$\frac{5}{600}$ = 8.3 mrad	0.32 mrad
Intensity in I.C.	15 kc/sec	7.8 kc/sec
Gain in current to voltage amp.	10^{11} V/A	10^{8} V/A
Beam size	w × h 1 × 5	w × h 2 × 10
Source	Tube voltage 55 kV Electron current: 190 mA	Electron energy 3.3 GeV Electron current: 50 mA

The entire set of critical data for the mixture $5CT_9:7CB_x:8OCB_{91-x}$ were taken during a 10-day period at the DORIS-ring. A complete set of data for one mixture could be obtained in 3-4 hours. In these experiments the monochromator and analyzer were Si(111), m=3 crystals. Similar critical data have been obtained over much longer time scales and with a somewhat relaxed longitudinal resolution given by m=1 Ge-crystals at the rotating anode. A more direct measurement of the intensity difference between similar

set-ups at the synchrotron and at the rotating anode is displayed in Figure 5.5 and Table 5.2. The transmission of the ion chamber for λ = 1.5422 Å-radiation is calculated to be 91%. The transmission has been measured at the rotating anode to be 92%.

Higher-order contributions to the synchrotron intensity in Table 5.2 are negligible, since the transmission of the third-order reflection Si(333) is 99% and from Figure 5.2 the third-order λ = 0.5 Å intensity is at least a factor of 10 lower than λ = 1.54 Å radiation. (Note that the spectrum in Figure 5.2 for DORIS must be shifted to the left for E = 3.3 GeV.)

When calculating $\Delta\lambda/\lambda$ for the synchrotron it is assumed that the source is uniform within $2\sqrt{2\ln 2}\cdot\sigma_x$ and zero outside. The measured values, both at the synchrotron and rotating anode, were obtained by rotating the analyzer crystal in the dispersive mode without a sample (See Figure 4.3 in Chapter 4). The good agreement between the measured and calculated values of $\Delta\lambda/\lambda$ at the synchrotron indicates that the FWHM of the source width is given rather accurately by $2\sqrt{2\ln 2}\cdot\sigma_x$ from Table 5.1. The measurements indicate that it is slightly broader. Preliminary, independent measurements of the source width, performed by scanning a photodiode across the beam close to the source, agree with our measurements to within 10%. The photodiode measurements were made by Dr. Zietz in HASYLAB.

The characteristic exponential decay of the $(\Delta\lambda/\lambda)$-curve for the CuKα-line (see Figure 4.7 in Chapter 4) is not expected to be found at the synchrotron, if the Gaussian approximation holds for the spatial distribution of the source, but a detailed experimental check still needs to be made.

Clearly, Table 5.2 shows that the synchrotron is by far a better X-ray source on all points apart from the bandwidth $(\Delta\lambda/\lambda)$. This bandwidth for the synchrotron can be reduced by moving further away from the source. The effect of moving further away is displayed in Figure 5.6, which shows measurements of $(\Delta\lambda/\lambda)$ at two different sites. While the triple-axis spectrometer was located at EMBL-outstation next to HASYLAB, the distance to the ring was

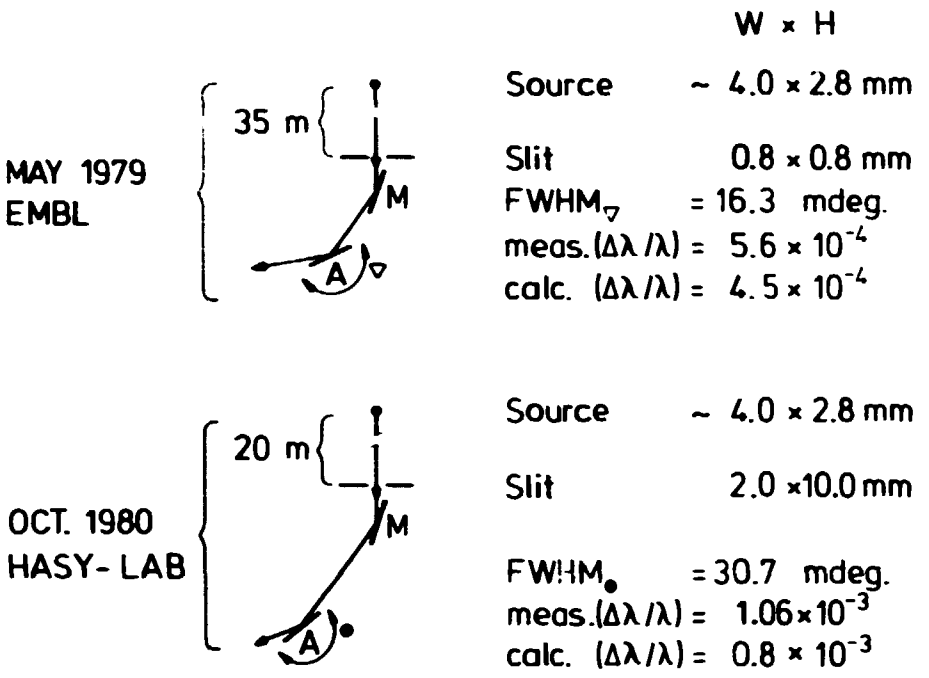

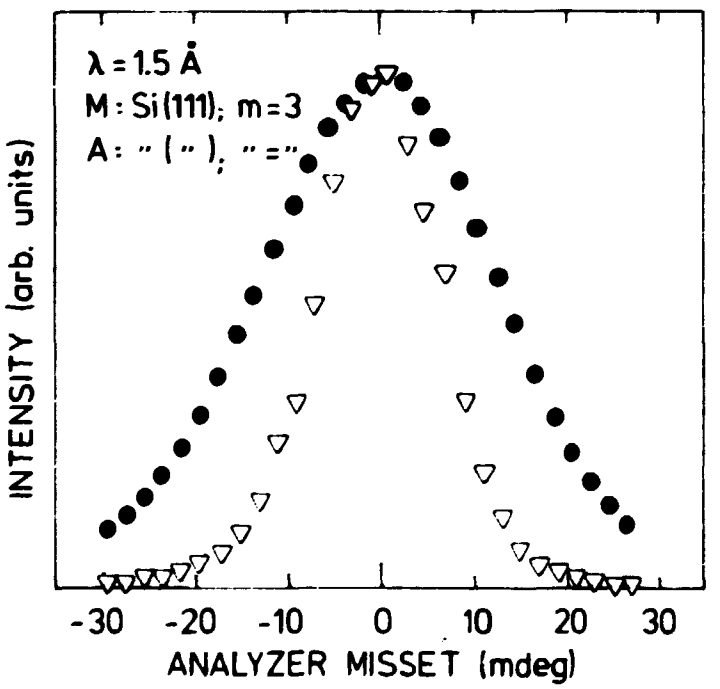

Fig. 5.6. The effect of moving further away from the synchrotron source. The monochromator and the analyzer are Si(111); m = 3-crystals.

35 m. This reduces ($\Delta\lambda/\lambda$) to a value comparable to the intrinsic line width of the CuKα-line.

REFERENCES

1) European synchrotron radiation facility (ESRF)-design as outlined by a European Science Foundation (ESF)-committee. Supplements II and III. May 1979.
2) U. Bonse (1979) X-ray sources. DESY SR-79/29, 19 p.
3) B. Rossi and H.H. Staub (1949) Ionization chambers and counters (McGraw Hill, New York) 243 p.
4) J. Als-Nielsen, J.D. Litster, R.J. Birgeneau, K. Kaplan, C.R. Safinya, A. Lindegaard Andersen and S. Mathiesen (1980) Phys. rev. B, 22, 312.

6. HIGH-RESOLUTION X-RAY STUDY OF THE SECOND-ORDER NEMATIC-SMECTIC-A PHASE TRANSITION IN THE MONOLAYER LIQUID CRYSTAL $\overline{8}S5$

The second-order phase transition from nematic to smectic-A in liquid crystals has been studied in detail in recent years using different experimental techniques. Until recently[2] the x-ray studies have concentrated on the so-called bilayer liquid crystals. Examples of these materials are CBOOA, 8OCB (see Chapter 2).

This chapter reports on a study of the monolayer liquid crystal $\overline{8}S5$, performed at the DORIS storage-ring in Hamburg, using synchrotron radiation. The material $\overline{8}S5$ is out of the C_nH_{2n+1}-Ø-COS-Ø-C_5H_{11} family, where Ø denotes a benzene ring. For $12 \geq n \geq 8$ these materials exhibit the following sequence of phases: isotropic → nematic → smectic-A → smectic-B → solid. $T_{NS}/T_{NI} \approx 0.72$ well below the limiting value of 0.87 above which the transition should become first order as predicted by McMillan[3].

To some extent the monolayer nature of this compound in the smectic-A phase will change the length/width-ratio of the basic building block. See Figure 6.1 and an increase of the ratio of longitudinal correlation length to transverse correlation length is expected ($\xi_{||}/\xi_{\perp}$; see Chapter 2), compared to the bilayer compounds. In Figure 6.1 a schematic picture of the nematic phase in the critical region is also shown. In this figure $\xi_{||}/\xi_{\perp} \approx 4$. The situation in bilayer compounds such as CBOOA, 8OCB, and 8CB is that $\xi_{||}/\xi_{\perp} \approx 5\text{-}8$[2].

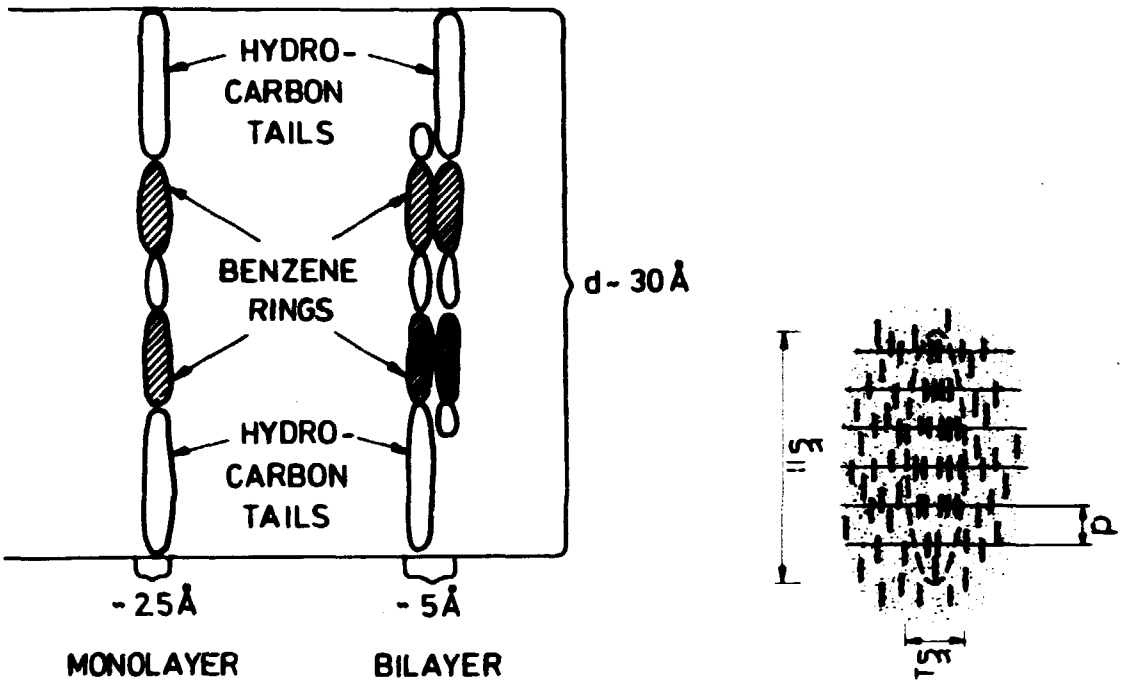

Fig. 6.1. A schematic drawing of a tentative model of the monolayer and the bilayer B.B.B.[1] and a schematic drawing of the nematic phase in the critical region.

6.1. Theoretical

The theoretical model for the transition from the nematic to smectic-A phase is outlined in Chapter 2. In short, the following theoretical predictions are made: The scattering cross section is given by:

$$S(\vec{q}) = \frac{S(\vec{q}_o)}{1 + \xi_{\parallel}^2(T)(q_{\parallel}-q)_o)^2 + \xi_{\perp}^2(T)\cdot q_{\perp}^2} \qquad (6.1)$$

where

$$q_\perp^2 = q_x^2 + q_y^2 \quad ; \quad q_{||} = q_z \quad ; \quad q_o = \frac{2\pi}{d} \quad \text{and}$$

$$\xi_{||} \equiv \sqrt{\frac{M_v}{2a}} \quad ; \quad \xi_\perp \equiv \sqrt{\frac{M_t}{2a}}$$

$$S(\vec{q}_o) \equiv a(\vec{q}_o) = k_B T/a = \frac{k_B T \cdot \xi_{||}^2}{2M_v} \equiv a \cdot \xi_{||}^2 \quad ; \quad a \equiv \frac{k_B T}{2M_v}$$

The notation refers to the free energy expression, describing the phase transition, given in Chapter 2. In De Gennes's superfluid-helium model for the nematic to smectic-A transition the following exponents are predicted:

$$\xi_{||,\perp} \sim t^{-\nu} \quad ; \quad a(\vec{q}_o) \sim t^{-\gamma} \quad ; \quad a \sim t^{-\nu\eta}$$

where

$$\nu = 0.66 \quad ; \quad \gamma = 1.30 \quad ; \quad \eta = 0.04$$

As opposed to the mean field result:

$$\nu = 1/2 \quad ; \quad \gamma = 1 \quad ; \quad \eta = 0$$

originating from assuming that: $a \sim (T-T_c)$.

6.2. Experimental

The experimental set-up is shown in Figure 3.1 in Chapter 3. It basically consists of the triple-axis spectrometer build at Risø. This spectrometer has been described elsewhere[4] and was only (during these initial experiments at the synchrotron) slightly modified to meet the requirements of operation at a storage ring as opposed to a rotating anode. Two important

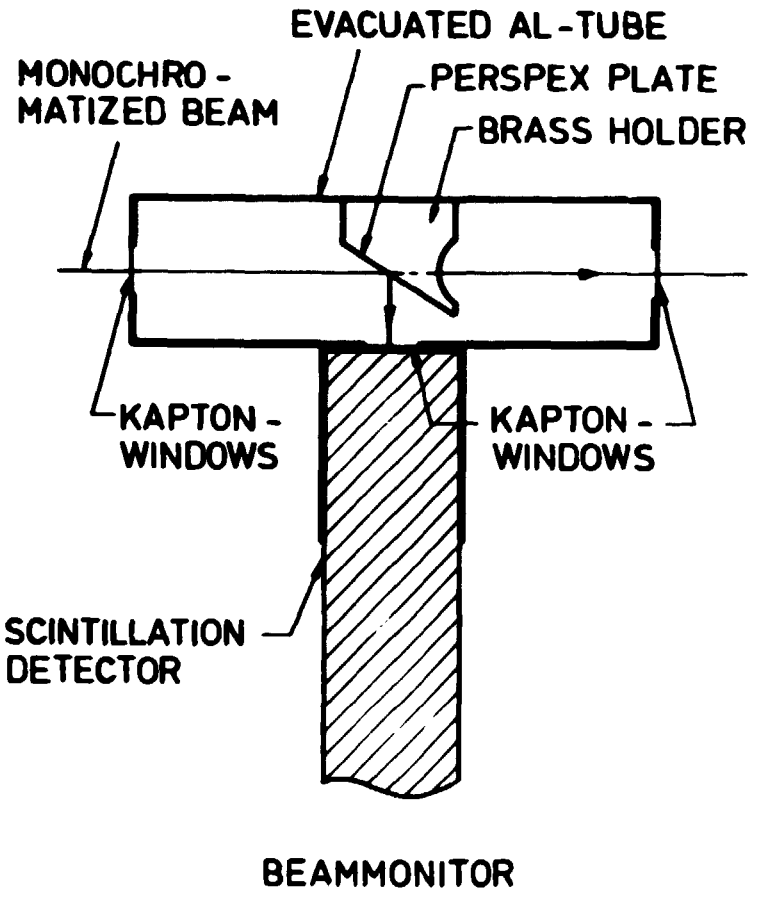

Fig. 6.2. The beam monitor. Unfortunately the scintillation detector (the photo multiplier) is sensitive to magnetic fringe fields.

changes were the addition of a beam monitor and a TV camera. The beam monitor is shown in Figure 6.2. Unfortunately, the magnetic fringe field from the sample magnet made this beam monitor ineffective. It turned out that with the geometry we had to use one gets a decreasing pulse height from the sodium-iodide detector with increasing magnetic fringe field. This effect must be due to electrons being bent away from their normal trajectory in the photomultiplier by the magnetic fringe field. This effect depends critically on the distance between magnet and monitor. Due to lack of space and the rather large magnet we used with a field of approximately 3000 gauss to grow the smectic liquid

crystal, it became impractical to use the beam monitor; thus we had to resort to the storage ring current in normalizing the counts. Later, we used an ion chamber, which have proved extremely useful. The width and height of the beam defining slit were 2 and 3 mm, respectively.

The full experiment took place during two sessions that were a few months apart and under differing beam conditions. During the first session (July 1979) DORIS ran under the following conditions: positron energy = 5.2 GeV giving a critical wavelength of 0.52 Å. The current was from 30 to 100 mA, with a lifetime of approximately 4 hours. During the second session (November 1979) DORIS ran under the conditions: positron energy = 4.73 GeV giving a critical wavelength of 0.57 Å. The current was from 10 to 20 mA with a lifetime of approximately 3-4 hours.

In Table 6.1 the experimental parameters employed in the two sessions are displayed. Note that the influence of the mosaicity of the sample is not included in the resolution function. This is because the convolution of $S(\vec{q})$ with the mosaicity distribution was done directly, using a measured mosaicity distribution which was often non-Gaussian. (See Appendix C for a description of the numerical deconvolution procedure.)

The longitudinal resolution function $R_{||}(q_{||})$ is approximated by a Gaussian with a width $W_{||}^2 = \alpha^2 + \beta^2$, where α is the width of the direct beam contribution and β the width of the $\Delta\lambda/\lambda$-contribution. The transverse resolution function $R_{\perp}(q_{\perp}) \approx \delta(q_{\perp})$ and the vertical resolution function $R_V(q_V)$ are approximated by a Gaussian with a width, calculated from the out-of-plane beam divergence allowed by the Soller-collimator.

The sample was contained in a flat 1.5 × 5 × 10 mm cell made of an Al-frame with Be-windows. The sample oven had two stages. It consisted of two heating elements, an inner and outer one, where the inner element contained the flat Be-cell with the liquid crystal. Each heating element was connected to a separate thermistor-controlled temperature regulator. By setting the outer element approximately 5 K below T_c and keeping an ultra-low gain

Table 6.1. Important experimental parameters during the sessions. The resolution functions are: $R_{||}(q_{||}) = e^{-(q_{||}/\sigma_{||})^2}$. $R_v(q_v) = e^{-(q_v/\sigma_v)^2}$. $R_T(q_T) = \delta(q_T)$ with the same notation as in Chapter 4. The values of T_c are the best judgement from the FWHM in $q_{||}$-scan and $q_\perp$-scan vs. T, when going up in temperature. (2mr) means that the Soller collimator giving the vertical resolution was a 2 mrad Soller collimator.

	λ/Å	$k_i = k_o/Å^{-1}$	Monochromator = analyzer	$\sigma_v/Å^{-1}$	FWHM of $R_v/Å^{-1}$ $= 2\sqrt{\ln 2}\cdot\sigma_v$	$\sigma_w/Å^{-1}$	FWHM of $R_w/Å^{-1}$ $= 2\sqrt{\ln 2}\cdot\sigma_w$	T_c/k
Session I (Jul. 79)	1.54	4.07	Si(111);m=1	$4.89\cdot10^{-3}$(2mr) $1.22\cdot10^{-2}$(5mr)	$8.14\cdot10^{-3}$(2mr) $2.03\cdot10^{-2}$(5mr)	$1.71\cdot10^{-4}$	$2.85\cdot10^{-4}$	333 060
Session II (Nov. 79)	1.54	4.07	Si(111);m=3	$7.35\cdot10^{-3}$(3mr)	$1.224\cdot10^{-2}$(3mr)	$1.12\cdot10^{-4}$	$1.86\cdot10^{-4}$	332 372

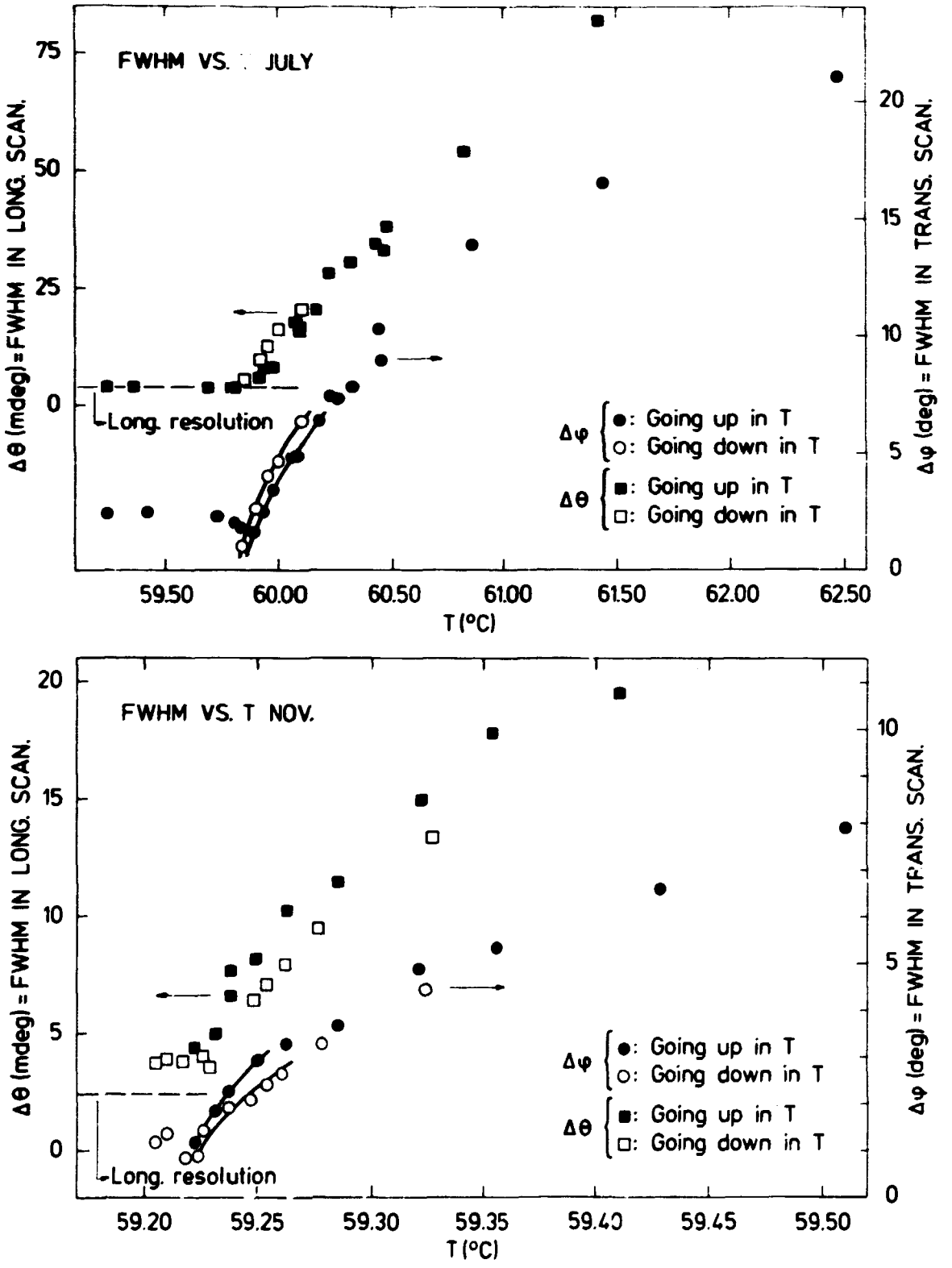

Fig. 6.3. The FWHM of longitudinal and transverse scans versus temperature.

in its control system, it was possible to control the temperature (near T_c) accurately using only the inner element. In this way one was able to obtain a temperature stability of ± 10 mK during the first session and after some modification ± 1.5 mK during the second session.

With the resolution and temperature stability we obtained, it turned out that neither of these became the limiting factor as far as probing close to T_c was concerned. The limiting factor was the difficulty of growing a perfect smectic-A phase. Even with a rather large magnetic field it was not possible to grow a smectic-A phase with a mosaicity lower than 1^o as can be seen from Figure 6.3, showing the sample-rocking curves versus T from the two sessions.

Since there is no way one can measure the mosaicity above T_c we had to assume a specific mosaicity in deconvoluting the data. As we shall see in the next section the correction, close to T_c, one gets by putting in mosaicity above T_c is rather large as opposed to assuming it is zero.

6.3. Data-analysis

The data were taken by performing longitudinal ($\vec{q}_{||}\vec{q}_o$) and transverse ($\vec{q}_{\perp}\vec{q}_o$) scans going through the critical region. In Figure 6.3 the FWHM's of longitudinal and transverse scans are shown. As one can see, there is a slight hysteresis when going down and going up in temperature indicated by the guide for the eye lines through the $\Delta\phi$ points. The data analysed are for increasing T in both sessions. A rather precise T_c can be read off from Figure 6.3 (the kink in the sample-rocking curves). A typical set of scans is shown in Figure 6.4, indicating the large $\xi_{||}/\xi_{\perp}$-ratio. The data were analysed by fitting the lineshape, convoluted with the mosaicity distribution (if included) and convoluted with the resolution function (Table 6.1) to the experimental data.

The data have thus been analysed for $T > T_c$ assuming 1) no mosaicity and 2) the same mosaicity as the one <u>at</u> $T = T_c$.

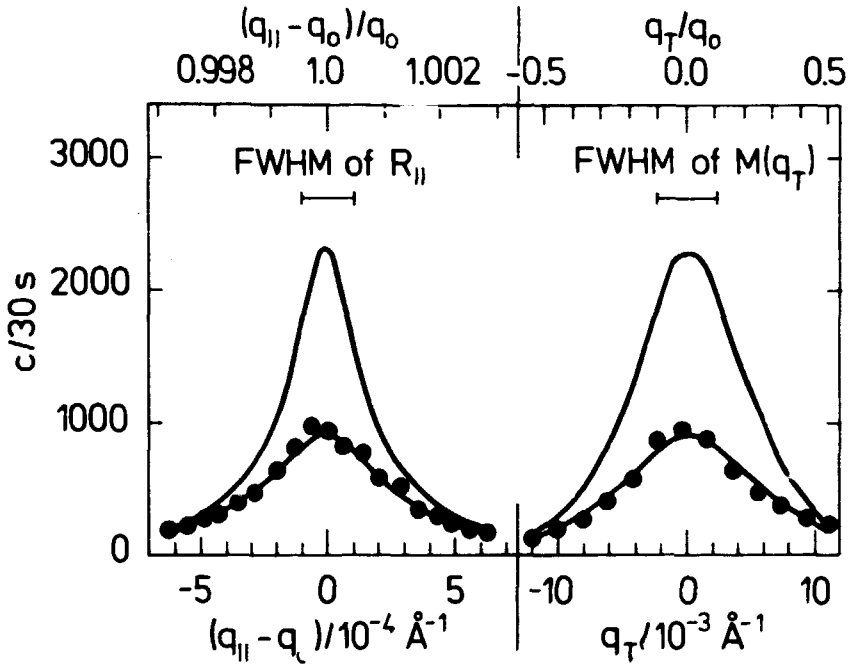

<u>Fig. 6.4</u>. Experimental data and fit for the set of data with the largest resolution correction. $T = T_c + 0.03^{\circ}C$; $t = 9 \cdot 10^{-5}$. FWHM of longitudinal scan is $5.8 \cdot 10^{-4}$Å^{-1}. FWHM of transverse scan is $11.4 \cdot 10^{-3}$Å^{-1}. Mosaicity is included in the fit and the <u>scattering crossection convoluted with the mosaicity is also shown</u>.

In Figure 6.5 the results of the fitting are displayed. The vertical line at the points close to T_c gives the correction to $\xi_{||,\perp} \cdot q_o$, when mosaicity is included. It is clear from this that the limiting factor in probing close to T_c is the inability to grow a perfect smectic-A phase.

An attempt to include a term + $c\xi_{\perp}^4 q_{\perp}^4$, in the numerator of the scattering cross section as done in the paper of J.D. Litster et al.[2], did not significantly lower the goodness-of-fit-parameter χ^2 and in any case c became negative. χ^2 was typically of

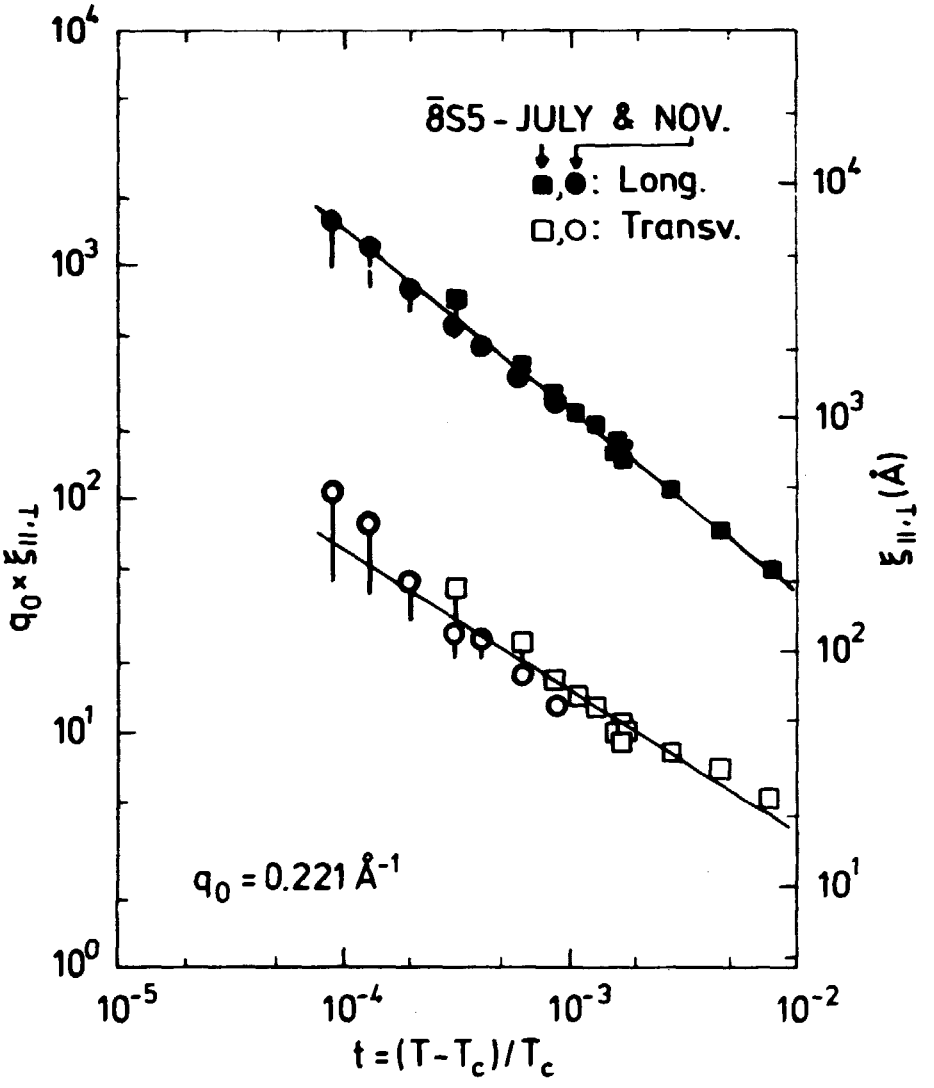

Fig. 6.5. The complete set of deconvoluted data from the two sessions.

the order of 2.5. This rather large value of χ^2 one may partly ascribe to the crude normalization of the data. With T_c fixed on the value obtained from Figure 6.3, the full dataset from the two sessions deconvoluted with mosaicity included, were fitted to $\xi^0_{\parallel,\perp} \cdot t^{-\nu_{\parallel,\perp}}$, yielding the following parameters:

$$\nu_{\parallel} = 0.77 \pm 0.04 \quad ; \quad \nu_{\perp} = 0.60 \pm 0.04 \text{ Å}$$

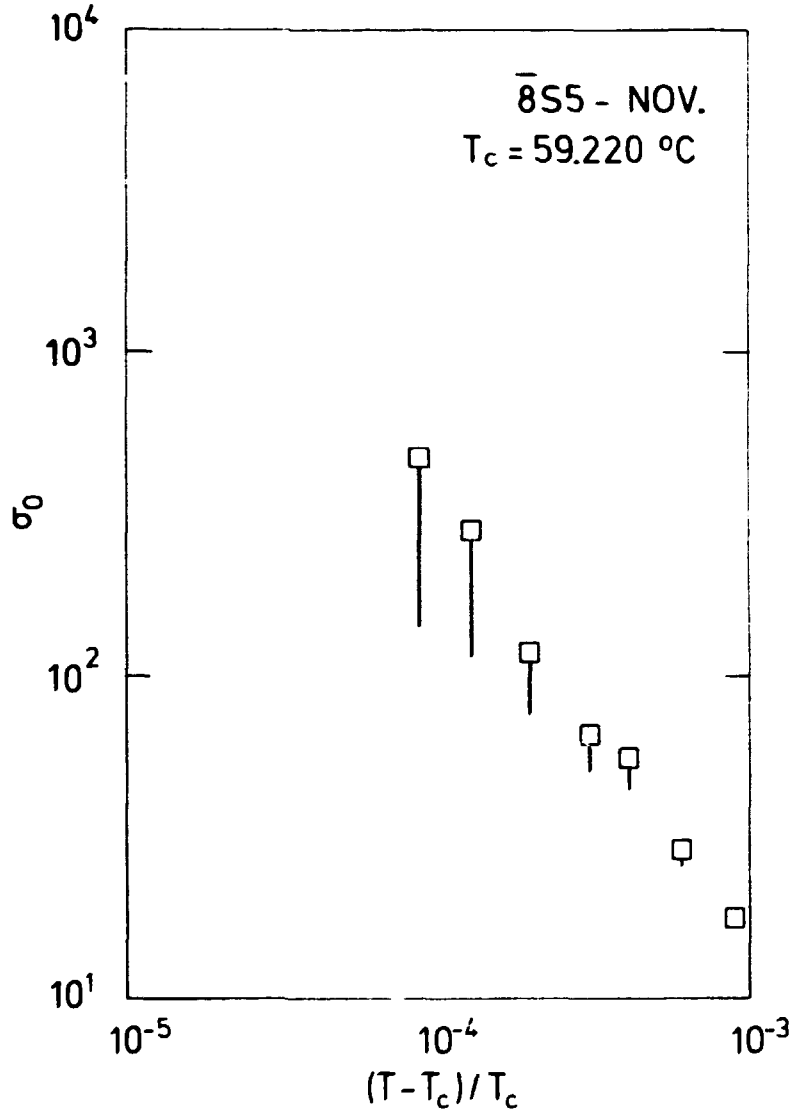

Fig. 6.6. The susceptibility $\sigma_o \sim t^{-\gamma}$ from the November-run. $\gamma \approx 1.35$.

The full lines in Figure 6.5 are the fitted curves. It is important to notice that the assumed mosaicity is the mosaicity at T_c and that this probably gives a larger correction to $\xi_{||,\perp} \cdot q_o$ than it should, since the mosaicity just above T_c, due to the magnetic field, probably is smaller than at T_c. The quoted uncertainties do not include this, of course, but only the uncertainties in T and $\xi_{||,\perp} \cdot q_o$.

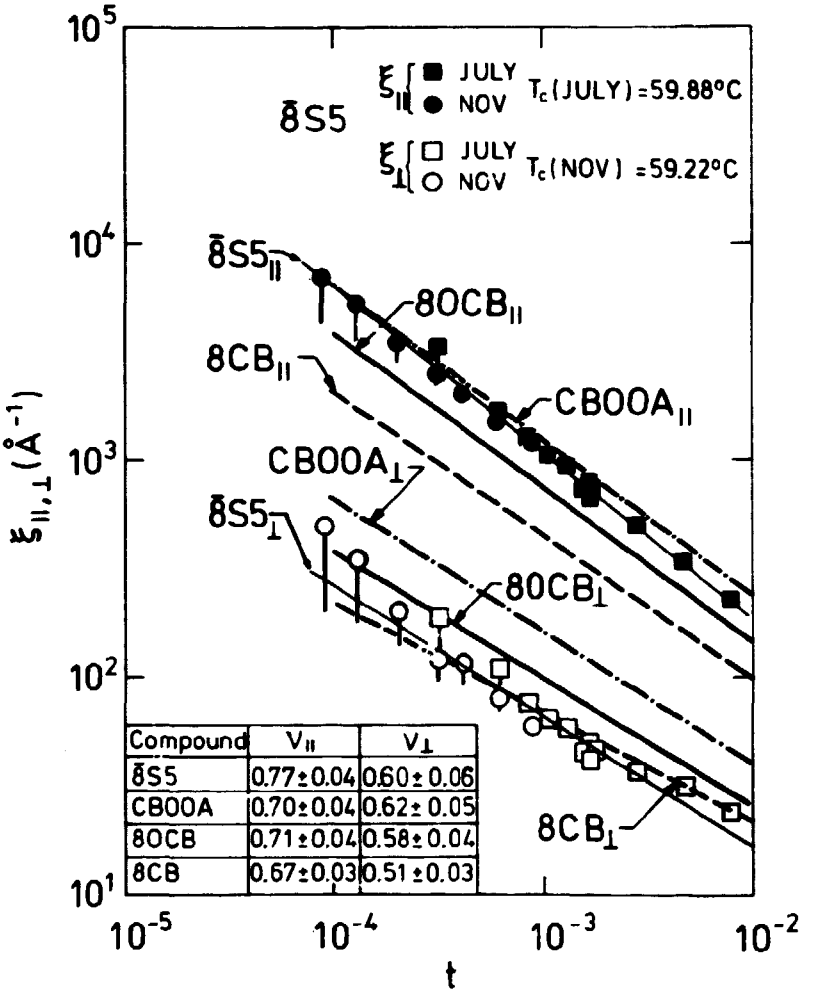

Compound	$V_{\parallel}$	$V_{\perp}$
$\bar{8}$S5	0.77±0.04	0.60±0.06
CBOOA	0.70±0.04	0.62±0.05
8OCB	0.71±0.04	0.58±0.04
8CB	0.67±0.03	0.51±0.03

Fig. 6.7. The correlation length for $\bar{8}$S5 compared with the correlation length for bilayer compounds 8CB, 8OCB and CBOOA. The full lines for 8S5 represent the fitted curve.

Lastly, the bilayer smectic-A compounds are compared to $\bar{8}$S5 in Figure 6.7; furthermore, the $\xi_{\parallel}/\xi_{\perp}$-ratio of $\bar{8}$S5 is shown in Figure 6.8. The difference in magnitude of this ratio for this monolayer smectic-A compound and bilayer smectic-A compounds as 8OCB, CBOOA and 8CB, is, intuitively, in good agreement with the assumption that the basic building block of the smectic-A phase of $\bar{8}$S5 is a single $\bar{8}$S5 molecule, while the basic building block of the smectic-A phase of f.ex. 8OCB is an overlapping

configuration of two 8OCB-molecules, as mentioned in the introduction to this chapter.

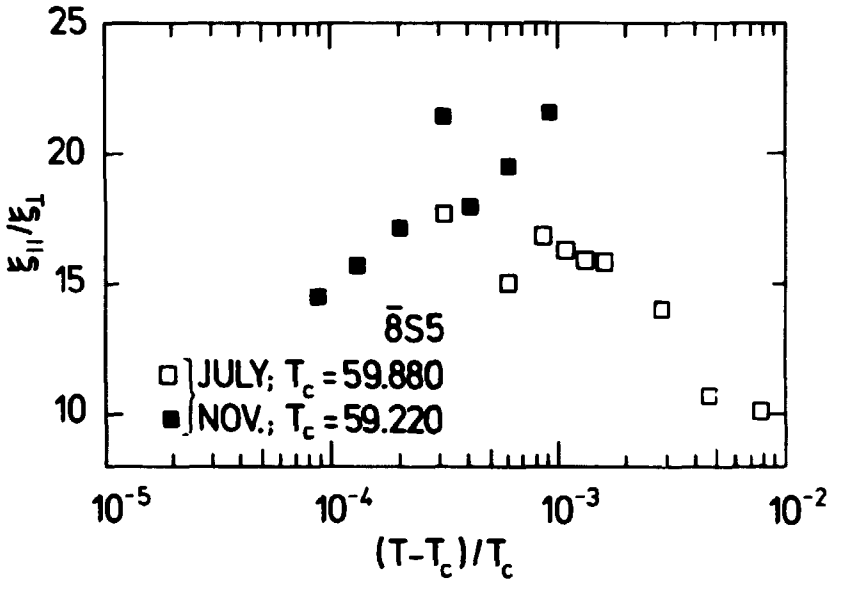

Fig. 6.8. The ratio between longitudinal correlation length $\xi_{||}$ and transverse correlation length $\xi_{\perp}$.

6.4. Conclusions

This study of the monolayer compound $\bar{8}S5$ deviates slightly from similar studies on bilayer compounds[1] as far as critical exponents are concerned. In all of the bilayer compounds 8CB, 8OCB and CBOOA, it was found that $\nu_{\perp} < \nu_{||}$, $\nu_{\perp}$ being close to 0.60 and $\nu_{||}$ close to 0.70. This is not quite the case for the monolayer compound $\bar{8}S5$, where $\nu_{\perp} = 0.60 < \nu_{||} = 0.77$. It must be noted, however, that the mosaicity correction is rather large compared with the case of the bilayer compounds. Pretransitional mosaicity seems to be a characteristic feature of the transition in the current sample geometry. It seems plausible to assume that the mosaicity function $M(q_{\perp},T) \rightarrow \delta(q_{\perp})$ for $T >> T_c$. A reasonable assumption to make about $M(q_{\perp},T)$ would be that $M(q_{\perp},T)$ is a Gaussian with a FWHM = $M_o \cdot F(T) \rightarrow 0$ as $T \rightarrow T_c$. Without any specific model for the decay rate of F(T) it seems rather dubious to guess at random and try to reanalyze the data with

this kind of $M(q_\perp,T)$. A "simple" way to avoid this difficulty in the analysis is to learn to grow better samples.

It was noted in Ref. 2 that the length/width ratio of an associated pair of molecules in a bilayer compound is smaller than $\xi_{||}/\xi_\perp$. This also appear to be the case for the monolayer liq. crystals, since $\xi_{||}/\xi_\perp$ for $\bar{8}S5$ is in the range 13 to 20 and the length/width ratio of $\bar{8}S5$ is ~ 10.

REFERENCES

1) P.E. Cladis, R.K. Bogardus and D. Aadsen (1978) Phys. Rev. A, 18, 2292.
2) J.D. Litster, J. Als-Nielsen, R.J. Birgeneau, S.S. Dana, D. Davidov, F. Garcia-Golding, M. Kaplan, C.R. Safinya & R. Schaetzing (1979) J. Colloq. Orsay, Fr. 40, C3, 339.
3) W. McMillan (1971) Phys. Rev. A, 4, 1238.
4) J. Als-Nielsen, F. Christensen & B. Buras (1980) Synchrotron News, No. 4, 11.

7. AN EXPERIMENTAL STUDY OF THE NEMATIC TO SMECTIC-A PHASE DIAGRAM OF THE MIXTURE $5CT_9:7CB_x:8OCB_{9\,1-x}$

The phenomenon, of reentrance in solid-state physics is known from a few, quite different, physical systems. Among these are superconductors, doped with magnetic inpurities, and liquid crystals, where the sequence: nematic → smectic-A → nematic is

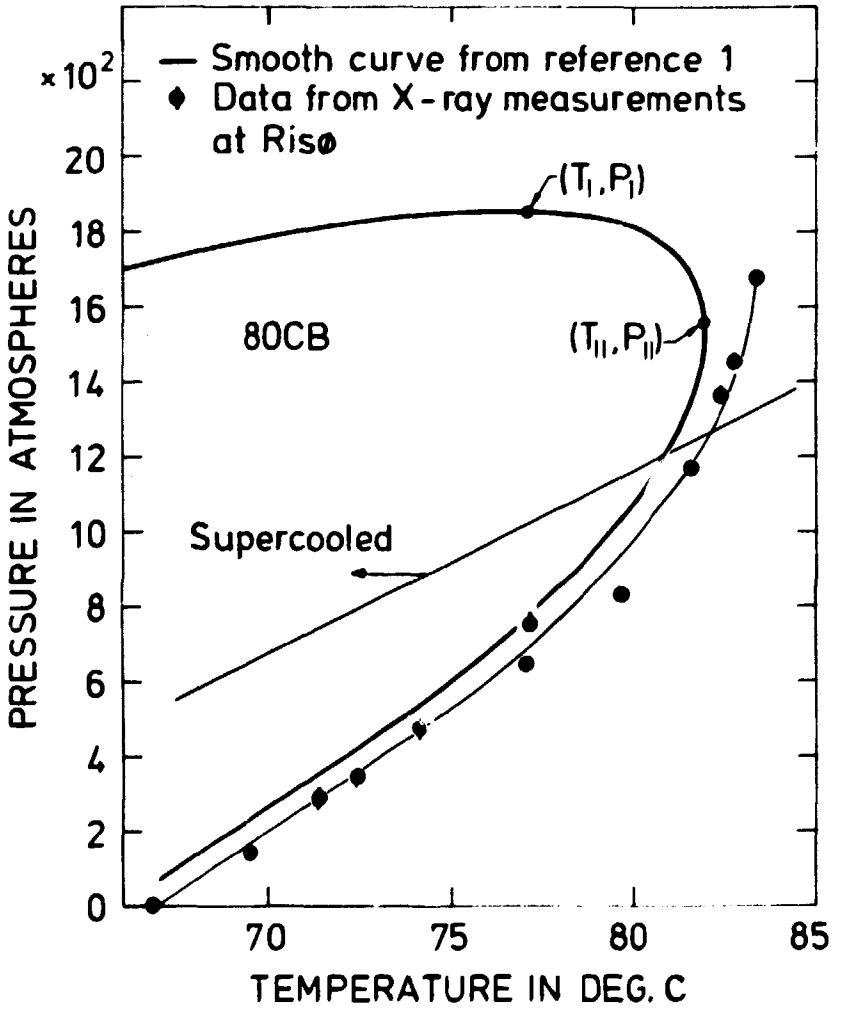

Fig. 7.1. The reentrance phenomena in 8OCB under pressure. Notice the supercooled region.

observed upon cooling. The liquid crystal systems exhibiting the reentrant nematic phase are certain pure bilayer materials[1] under pressure and various mixtures of liquid crystals at atmospheric pressure. One of the pure systems is 8OCB, which has been studied in some detail by P.E. Cladis et al..[1] (see Figure 7.1). One of the mixtures is the ternary mixture: $5CT_9$:$7CB_x$:$8OCB_{91-x}$, which exhibits a reentrant nematic phase for $x \leq 76.74$, where x is weight percent. 5CT is acronym for pentylcyanoterphenyl with the chemical formula C_5H_{11}-Ø-Ø-Ø-CN, 7CB is acronym for heptylcyanobiphenyl with the chemical formula C_7H_{15}-Ø-Ø-CN. 8OCB is acronym for oxycyanobiphenyl with the chemical formula C_8H_{17}-O-Ø-Ø-CN. This mixture has the advantage over the P-T phase diagram of the pure systems, like 8OCB, that the re-entrant nematic phase is stable and the phase transitions are second order.

A flow behaviour investigation of the mixture $5CT_9$:$7CB_x$:$8OCB_{91-x}$ has been made by S. Bhattacharya and S. Letcher.[3] It is the purpose of this chapter to report on a high-resolution X-ray study of the same mixture, performed using synchrotron radiation from DORIS in Hamburg. Table 7.1 summarizes the phases and the transition temperatures for the three components of the mixture.

Table 7.1. The transition temperatures (°C) of the three components of the ternary mixture $5CT_9$:$7CB_x$:$8OCB_{91-x}$. Note that 5CT & 7CB do not possess a smectic-A phase.

Material	$T_C \rightarrow S_A$	$T_C \rightarrow N$	$T_{S_A} \rightarrow N$	$T_N \rightarrow I$
5CT	./.	131	./.	240
7CB	./.	30	./.	42.8
8OCB	54.5	./.	67	80

7.1. Experimental

The full experiment was done during a prolonged session of dedicated beam time at DORIS. The beam conditions were: electron energy = 4.3 GeV, with the electron current typically between

100 mA and 20 mA. The experimental setup was the triple-axis arrangement displayed in Figure 3.1 in Chapter 3, except that there was no Soller collimator after the sample. The monochromator and analyzer were Si(111) m = 3 crystals and the beam-defining slit had the dimensions: w × h = 2 × 10 mm. The three components of the mixture were purchased from BDH Chemicals, with no additional treatment before use. The sample was mixed on location, heated up to the isotropic phase, and pumped on for approximately one hour. After the sample cell was installed in the oven, the entire oven was evacuated.

The oven had to be cooled down to ~ 5°C. This was done by water cooling. Figure 7.2 shows the oven.

The fine control of the temperature was performed by using a thermistor-controlled heating element symmetrically placed above and below the sample cell. The gold foil on either side of the sample cell diminished temperature gradients across the sample. A temperature stability of ± 1 mK could be obtained.

Six mixtures were investigated. Table 7.2 gives relevant experimental parameters for all six.

Table 7.2. Relevant experimental parameters for the six mixtures. The resolution function is
$R(q') = \delta(q_T) \cdot e^{-(q_\parallel/\sigma_\parallel)^2} \cdot e^{-(q_V'/\sigma_V)^2}$.
$\sigma_\parallel$ is obtained from the direct beam profile and the $\Delta\lambda/\lambda$-contribution as outlined in Chapter 4. σ_V is calculated from the vertical collimation after the sample, given by the height of the detector window and the distance between sample and detector.

Mixture #	x Weight percent	λ Å	$2\sqrt{\ln 2}\cdot\sigma_\parallel$ $Å^{-1}$	$2\sqrt{\ln 2}\ \sigma_V$ $Å^{-1}$	T_{N-A} °C	T_{N^*-A} °C
1	72.17	1.468	$2.62\cdot10^{-4}$	$1.68\cdot10^{-2}$	26.41	7.00
2	73.03	1.523	- " -	- " -	25.41	8.00
3	74.92	1.468	- " -	- " -	22.06	10.43
4	76.45	1.523	- " -	- " -	18.00	10.43
5	76.80	1.468	- " -	- " -	./.	./.
6	77.05	1.523	- " -	- " -	./.	./.

Data were taken by performing longitudinal and transverse scans going through the critical region. Correlation lengths were obtained by fitting the experimental data to the Lorentzian scattering cross-section (Chapters 2 and 4, and Appendix C) convoluted with the resolution function.

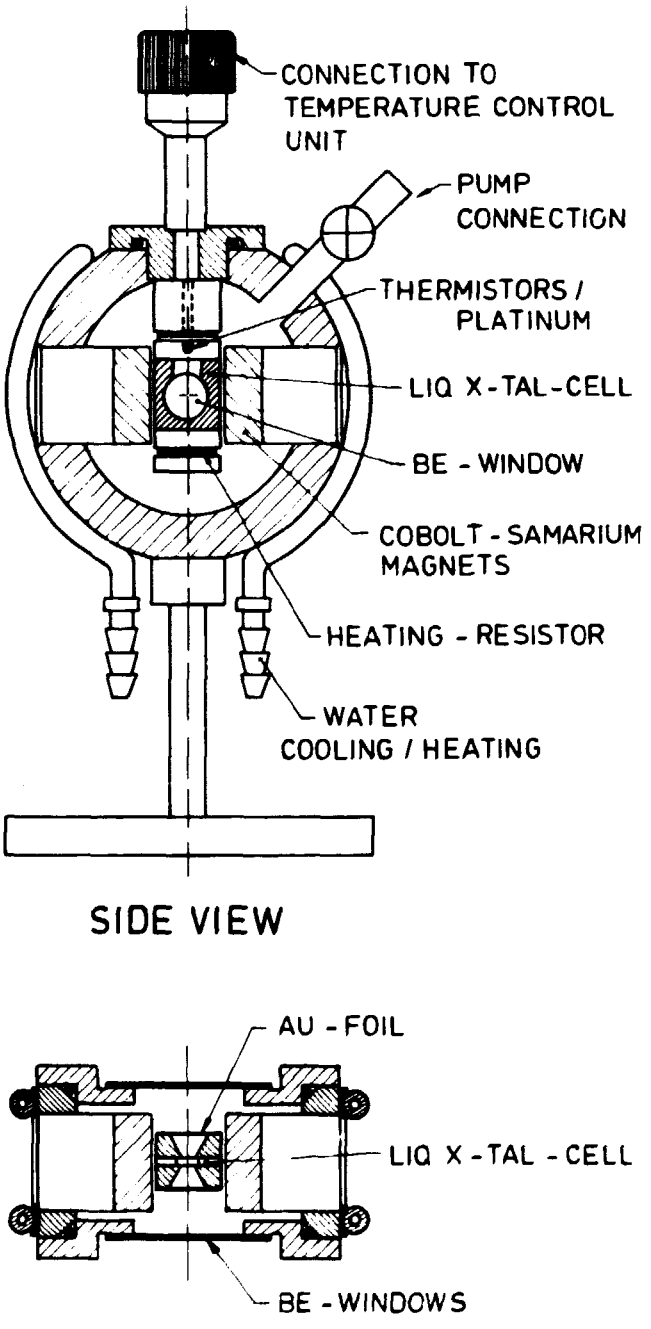

Fig. 7.2. The sample oven. The permanent Cobalt-Samarium magnet gave a magnetic field of approximately 1kG.

7.2. Results

The FWHM of longitudinal and transverse scans versus temperature is displayed in Figure 7.3a) & b) for the total set of data. From this plot, critical temperatures are obtained and the phase diagram determined.

This is shown in Figure 7.3c. T_c is read off from Figure 7.3a & b and a conservative estimate of the uncertainty on T_c is found as 0.2^oC. Three more points on the phase diagram have been obtained by a somewhat cruder method. The occurrence of the N-Sm-A transition can namely be seen directly, when cooling down through the transition. This is because the nematic phase, due to director-fluctuations, appears turbid, while the Sm-A phase, with damped director-fluctuations, is transparent. In this way, the following three points, with an uncertainty of 0.5^oC, have been found (these are not shown in Figure 7.3c):

i) $x = 0.66$; $T_c = 3.5^oC$
ii) $x = 0.66$; $T_c = 34.0^oC$
iii) $x = 0.0$; $T_c = 75^oC$

The three components were mixed as powders. The uncertainty in x comes from the weighing procedure; a conservative estimate of this uncertainty is 0.01%. Two different fits to the phase boundary are shown. The dotted-line parabola can be predicted by Landau theory and the full-line rotated-parabola represents a better fit.

The raw data were deconvoluted using the procedure described in Appendix C. The fit of experimental data to the scattering cross-section convoluted with the resolution function was generally good with the goodness-of-fit parameter $\chi^2 \approx 1$-2. In Figure 7.4 this is shown for a set of data of mixture #4. The FWHM of the longitudinal resolution is shown for reference. As can be seen from Figure 7.7, showing a comparison between 8OCB, $\bar{8}S5$, and mixture #2-correlation lengths, the mosaicity correction is not the limiting factor in probing close to T_c for the mixture-experiments. $q_o\xi_{||}$ is so large, compared to $\bar{8}S5$ that the

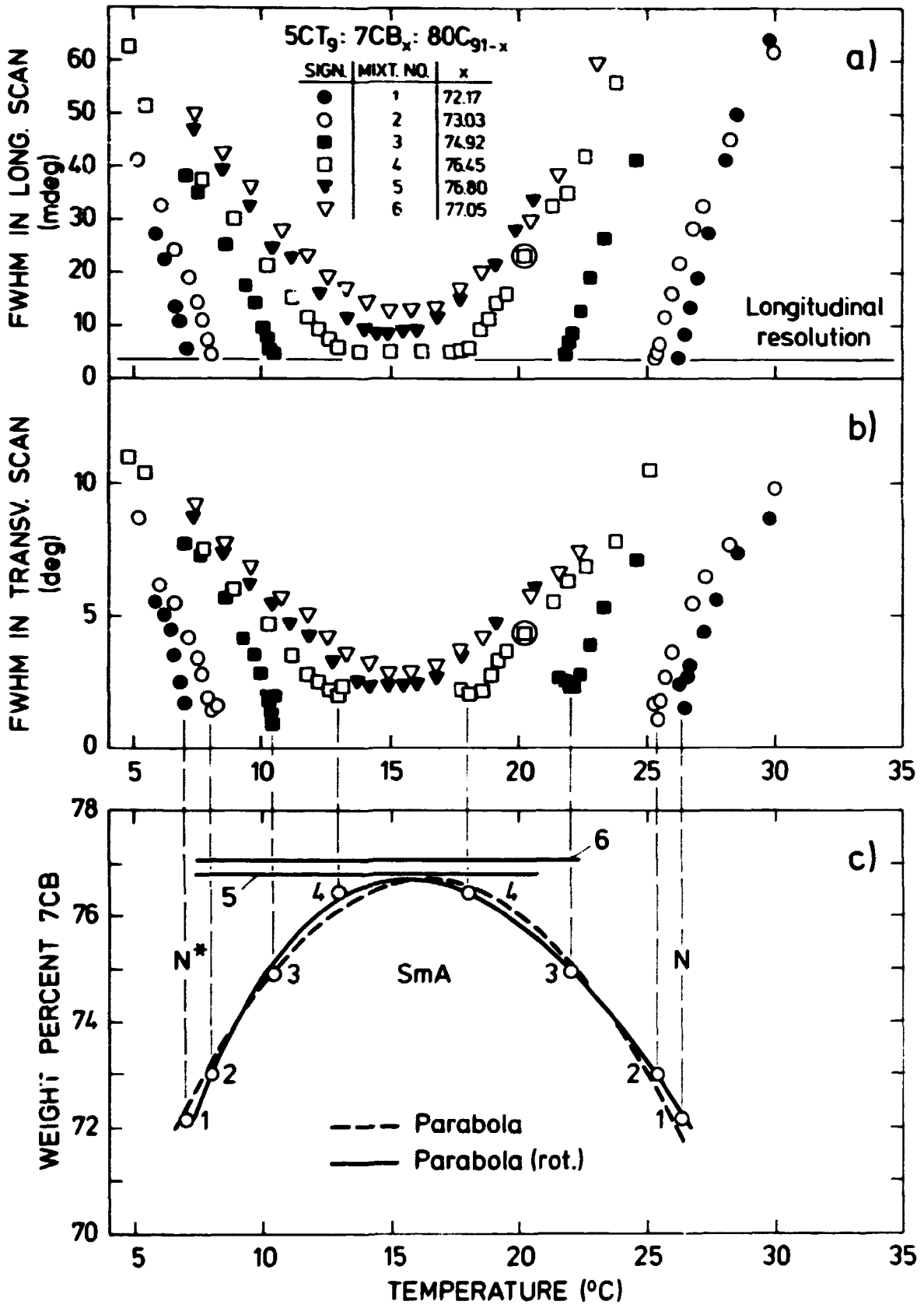

Fig. 7.3. FWHM of longitudinal and transverse scans versus temperature. Especially interesting are mixtures 5 and 6 where the correlation length grows, but never grows to infinity. The deconvolution of the scans, corresponding to the encircled points, is shown in Figure 7.3c). The T-x phase diagram deduced from a) & b). Two fits are shown. A parabola with axis perpendicular to the temperature axis and a rotated parabola, which represents a better fit to the data.

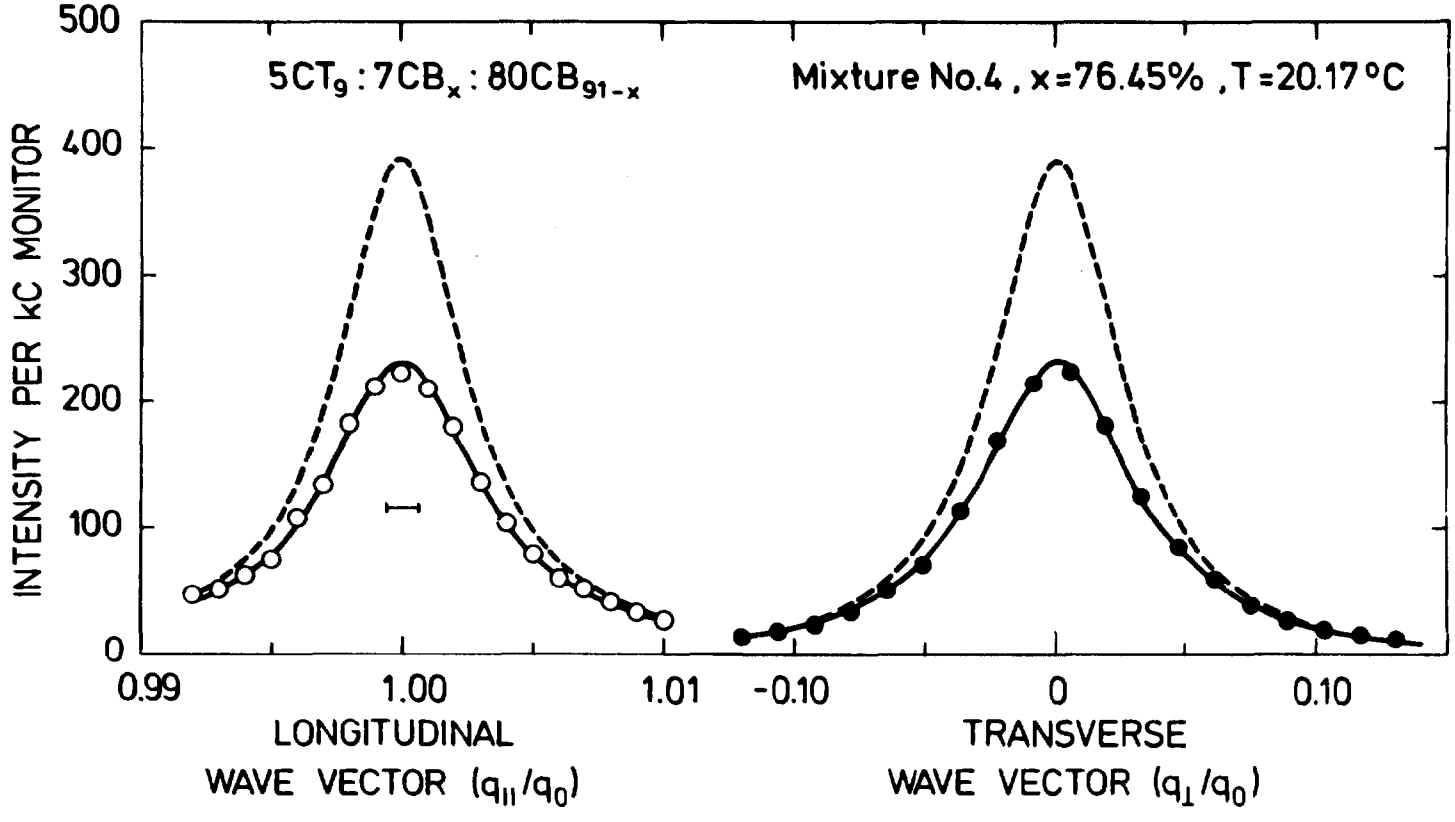

Fig. 7.4. Longitudinal and transverse scans through the (0,0,1) reciprocal lattice point show the smectic-A fluctuations in the nematic phase of liquid crystal mixtures at 20.17°C. Full lines are least squares fits of the cross section (dashed curve) folded with the resolution.

longitudinal resolution sets the limit for the mixture experiments. Therefore, mosaicity was not included in the fit and the transverse resolution is a delta function.

The correlation lengths versus reduced temperature for the six mixtures are shown in Figures 7.5 and 7.6.

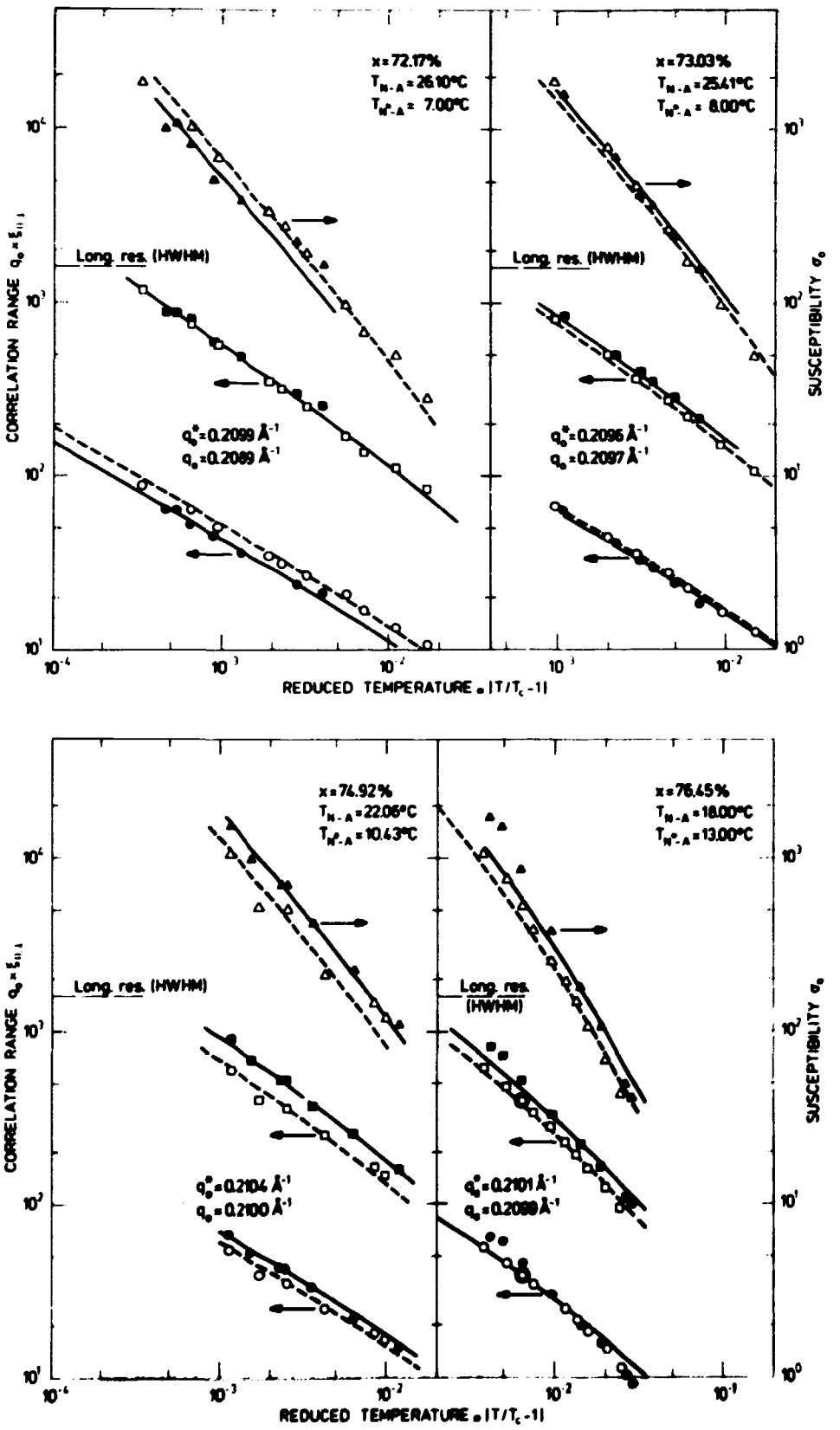

Fig. 7.5. $q_o \cdot \xi_{||}$, $q_o \cdot \xi_{\perp}$ and σ_o for mixtures No. 1-4. Filled points are for the N* → A-transition. The encircled point corresponds to the encircled point in Figure 7.3. The q_o and q^* are $2\pi/d$ at T_{N-A} and at T_{N^*-A}.

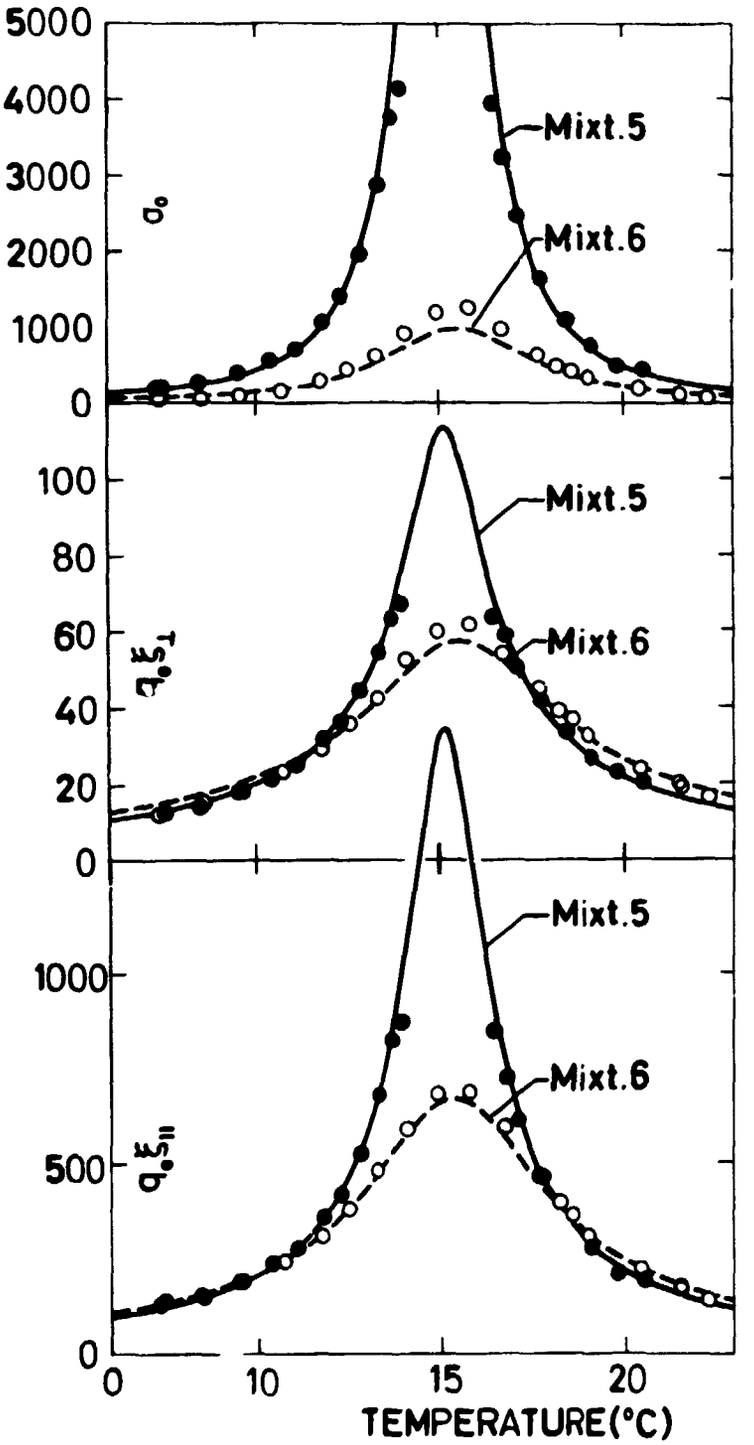

Fig. 7.6. $q_o \cdot \xi_{||}$, $q_o \cdot \xi_\perp$ and σ_o for x = 76.80 & 77.05%.

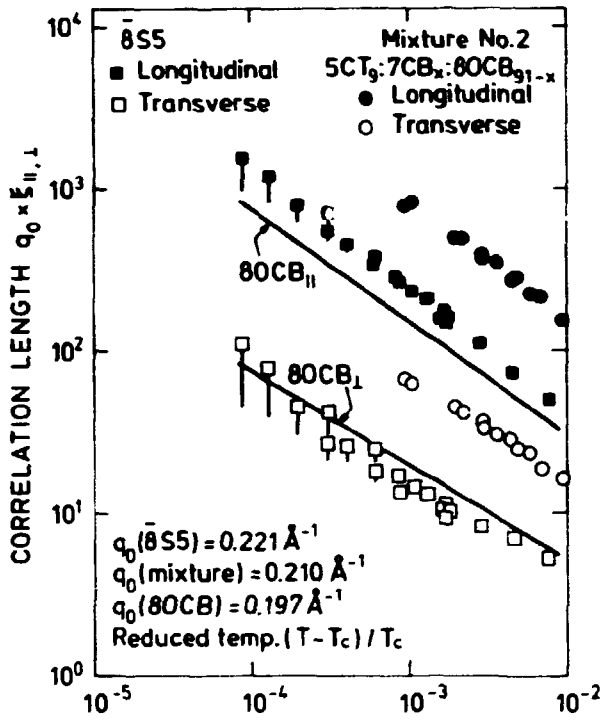

Fig. 7.7. A comparison between correlation lengths for two pure materials, $\bar{8}$S5 and 8OCB, and mixture No. 2. Notice that for the mixture the longitudinal resolution sets the limit for probing close to T_C, not the mosaicity, as in the $\bar{8}$S5-experiments.

7.3. Comparison with theoretical predictions

A Landau theory of the reentrant nematic-smectic-A phase transition is given by P.S. Pershan and J. Prost[4]. Their work is based on the assumption of the existence of an optimum density for smectic ordering; on the microscopic level this means that above the optimum density, the interactions stabilizing smectic order are suppressed by steric effects and the reentrant nematic phase are obtained. The Landau theory was primarily proposed in an attempt to explain the P-T phase d agram of 8OCB[1], but the mixtures are treated by the theory as well.

The Landau theory of P.S. Pershan and J. Prost involves a coupling between the smectic order parameter $|\psi|$ and the two parameters; the density ρ and the relative concentration of one of the components of a binary mixture x. The coupling is introduced by adding a term $g(\rho,x)\cdot|\psi|^2$ to the usual form of the power expansion in $|\psi|$ of the free energy F.

$$F-F_N = \frac{1}{2} A|\psi|^2 + g(\rho,x)|\psi|^2 + \frac{1}{4} B|\psi|^4 + \frac{1}{6} C|\psi|^6 \qquad (7.1)$$

where F_N is the nematic free energy. $A = a\cdot(T-T_o)$.

Expanding $g(\rho,x)$ in a power series in $(\rho-\rho_o,\ x-x_o)$ and keeping only leading terms yields

$$F-F_N = \frac{1}{2} A'|\psi|^2 + \frac{1}{4} B|\psi|^4 + \frac{1}{5} C|\psi|^6 \qquad (7.2)$$

with $A' = a(T-T^*(x,\rho))$ where

$$T^*(x,\rho) = T_o(x) + t_2(\rho-\rho_o)^2 \ ;\ t_2 < 0 \qquad (7.3)$$

Evidently T* is a measure of the interactions favouring smectic order and the above relation contains the basic physics of the Pershan-Prost theory, namely the existence of an optimum density ρ_o, favouring smectic order. The phase diagram is determined[4] by the condition:

$$T-T^*(x^N,\rho^N) = K$$

where K is 0 for a second-order transition or $3\cdot B^2/16aC$ for a first-order transition.

With

$$(\rho^N-\rho_o)/\rho_o = -\alpha_N(T-T_o) + \beta_N(P-P_o)$$

where α_N and β_N are, respectively, the thermal expansion and the compressibility for the nematic phase, the following expression for the phase boundary is obtained:

$$T_3(T_1(x)-T) = (T_2-T + (\beta_N/\alpha_N/\alpha_N)P)^2 \text{ or} \tag{7.4}$$

$$(T_m-T_m')(T_m-T) = \left[(T_m-T) + \left(\frac{\beta_N}{\alpha_N}\right)(P-P_m)\right]^2$$

where $T_1(x)$ is either $T_o(x)$ for a second-order transition or $T_o(x) + 3B^2/16aC$ for a first-order transition and $T_2 = T_o - \beta_N/\alpha_N P_o$ and

$$T_3 = -\frac{1}{t_2 \rho_o^2 \alpha_N^2} \tag{7.5}$$

and the following relations hold where (T_t,P_t) and (T_m,P_m) are indicated on Figure 7.1.

$T_m = T_1(x)(= T_o(x)$ for a second-order transition) ; $T_m - T_m' = T_3$

$$P_2 = \frac{\alpha_N}{\beta_N}(T_m-T_2) \quad ; \quad P' = \frac{\alpha_N}{\beta_N}[T_m + T_3/4-T_2]$$

$$T_t = T_m - T_3/4$$

The P-T phase diagram of 8OCB is fitted accurately by the expression, with the ratio (β_N/α_N) close to experimental values.

In order to obtain an expression for the x-T phase diagram at 1 atm, it is necessary to assume a specific form of $T_o(x)$. The simplest assumption is to assume that $T_o(x)$ is linear in x:

$$T_o(x) = T_1 - t_1 \cdot x \tag{7.6}$$

Alternatively, one can follow Pershan and Prost and assume $T_o(x)$ is linear in y = the weight ratio of the two components of a binary mixture = $\frac{x}{1-x}$.

Inserting the x-linearity in the expression for the phase diagram and letting $P=P_o$ (1 atm.) gives the T-x phase diagram

$$C(x_o-x) = (T_M-T)^2 \qquad (7.7)$$

with

$$T_M = T_o-T_3/2 \text{ and } C = t_1T_3$$
$$t_1x_o = T_1-T_o + T_3/4 \qquad (7.8)$$

Thus, the existence of an optimum density for smectic ordering and the simple ad hoc assumption of linearity of $T_o(x)$ leads to a parabolic T-x-phase diagram or alternatively a parabolic T-y-phase diagram.

Carrying over the above theory for a binary mixture to a ternary one like $5CT_{.09}:7CB_{.x}:8OCB_{.91-.x}$ should give a parabolic T-x' phase diagram with x' = weight(7CB)/(weight(7CB) + weight(8OCB)). Since $x' = x\ \frac{100}{91}$ one may as well talk of a parabolic T-x phase diagram. Alternatively, (if $T_o(x)$ is linear in y) the theory predicts a parabolic T-y phase diagram, with y = weight(7CB)/weight(8OCB) = 0.x/(0.91-0.x).

When looking at the datapoints obtained over the <u>whole</u> x or y range in the present study of the ternary mixture, it is obvious that neither a T-x nor T-y fit of the simple form (7.7) is reasonable. Leaving out the points at x = 0 and x = 0.66 gave the following parameters in a parabolic T-x fit of the form (7.7):

$$T = T_M \pm (C(x_o-x))^{1/2} \ ; \ T_M = 16.29^oC \ ; \ x_o = 0.7674 \ ; \ C = 2018 \qquad (7.9)$$

This fit is not too bad but a better fit to the <u>whole</u> set of data could be obtained with a rotated parabola:

$$T = T_M + K(x_o-x) \pm (C(x_o-x))^{1/2} \qquad (7.10)$$

The fit was acceptable with an uncertainty of 0.2^oC in T_c and no uncertainty on x. It yielded the following parameters:

$$T_M = 15.62^{o}C \; ; \; x_o = 0.7674 \; ; \; C = 2036 \; ; \; K = 26.02 \qquad (7.11)$$

As is obvious from Figure 7.3c the rotated parabola represents a better fit also to the eight datapoints investigated with X-rays. Thus, one may conclusively infer that the phase diagram is rather well described by a parabola of form (7.7) in the vicinity of x_o, but not over the whole range investigated. The experiments reported on for 8OCB-6OCB by A.R. Kortan et al. do in fact exhibit a parabolic phase diagram of the form (7.7) in a T-y fit as originally proposed[4] by J. Prost and P. Pershan, but not in a T-x fit.

One of the most spectacular features of the phase diagram is the apparent doubling of the critical exponents ν and γ when approaching a locally parabolic phase boundary tangentially. This can be seen by writing down the free energy for the $P=P_{'}$-isobar, the $T=T_{''}$-isoterm and the $x=x_o$-isodensity curves in case of a second-order phase transition. One gets:

$$\text{P=P}_{'}\text{-isobar:} \qquad F-F_N = \frac{a(T-T_{'})^2}{2 \cdot T_3} \cdot |\psi|^2 + \frac{1}{4} B|\psi|^4 + \frac{1}{6} C|\psi|^6$$

$$\text{T=T}_{''}\text{-isoterm:} \qquad F-F_N = \frac{a \cdot (P-P_{''})^2}{2 \cdot T_3} \left(\frac{\beta_N}{\alpha_N}\right) \cdot |\psi|^2 + \frac{1}{4} B|\psi|^4 + \frac{1}{6} C|\psi|^6$$

$$\text{x=x}_o\text{-isodensity:} \quad F-F_N = \frac{a}{2} (T-T_M)^2 \; \beta|\psi|^2 + \frac{1}{4} B|\psi|^4 + \frac{1}{6} C|\psi|^6$$

These Landau expansions are quite unusual. The coefficient of the quadratic term goes to zero without changing sign or physically the fluctuations go to infinity, but no phase transition takes place.

The critical points $(T_{'},P_{'})$, $(T_{''},P_{''})$ and (T_M,x_o) themselves are not special, but the approach along either the $P=P_{'}$-isobar, or $T=T_{''}$-isoterm or the $x=x_o$-isodensity is special and leads, accor-

ding to the free energy expressions, to an apparent doubling of the critical exponents ν and γ over the usual mean field values 1, 1/2. Note that the critical exponent η is defined <u>at</u> T_c and is therefore <u>not</u> influenced by the special approach.

The above indicates that there must be dramatic crossover effects when going from $x<x_o$ to $x=x_o$. In order to account for this quantitatively, A.R. Kortan et al. have proposed a modified free energy expansion. To allow for non-mean field exponents and different exponents $\nu_{||}$ and $\nu_{\perp}$ the following expansion is introduced:

$$F-F_N = \alpha|\psi|^2 + M_v\left|\frac{\partial\psi}{\partial z}\right|^2 + M_t\left|\left[\left(\frac{\partial}{\partial x} + iq_o n_x\right) + \left(\frac{\partial}{\partial y} + iq_o n_y\right)\right]\psi\right|^2 + \beta|\psi|^4 + \ldots \qquad (7.12)$$

where:

$$\alpha = a(T-T^*)^{\gamma} \quad ; \quad \beta = b(T-T^*)^{\gamma-2\beta}$$
$$M_v = M_{v,o}(T-T^*)^{\gamma-2\nu_{||}} \quad ; \quad M_t = M_{t,o}(T-T^*)^{\gamma-2\nu_{||}} \qquad (7.13)$$

and where T^* is the T^* from the Pershan-Prost free energy. $F-F_N$ predicts the following expression for the correlation lengths and the susceptibility:

$$\xi_{||} = \sqrt{\frac{M_v}{\alpha}} = \sqrt{\frac{M_{v,o}}{a}}\,(T-T^*)^{-\nu_{||}} \quad ; \quad \xi_{\perp} = \sqrt{\frac{M_t}{\alpha}}\,(T-T^*)^{-\nu_{\perp}}$$
$$\sigma_o = \frac{kT}{\alpha} = \frac{kT}{a}\,(T-T^*)^{-\gamma} \qquad (7.14)$$

where T^* is given by:

$$T^* = T_1 - t_1 x - \frac{1}{T_3}(T-T_o)^2$$

Noting that (7.7) is actually an equation for a phase boundary the T in this equation is actually T_c (for a specific x).

Using the parabolic expression for T_c (7.7) it is easy to derive expressions for T-T* in the two cases $x > x_o$ and $x < x_o$:

$$x < x_o : T-T^* = (T_c\Delta T/T_3)[t + (T_c/\Delta T)t^2] \; ; \; t = |(T-T_c)/T_c|$$

$$x > x_o : T-T^* = 1/T_3[(T-T_M)^2 + (t_1T_3)(x_o-x)] \; ;$$

where: $$\Delta T = 2\cdot(C(x_o-x))^{1/2} \qquad (7.15)$$

This leads to the following expressions for $q_o\xi_{||}$, $q_o\xi_\perp$ and σ_o:

$$q_o\xi_{||} = q_o/T_3 \sqrt{\frac{M_{v,o}}{a}} (T_c\Delta T/T_3)^{-\nu_{||}} [t + (T_c/\Delta T)t^2]^{-\nu_{||}}$$

$$q_o\xi_\perp = q_o/T_3 \sqrt{\frac{M_{t,o}}{a}} (T_c\Delta T/T_3)^{-\nu_\perp} [t + (T_c/\Delta T)t^2]^{-\nu_\perp} \qquad x<x_o$$

$$\sigma_o = kT/aT_3(T_c\Delta T/T_3)^{-\gamma}[t + (T_c/\Delta T)t^2]^{-\gamma} \qquad (7.16)$$

and

$$q_o\xi_{||} = q_o/T_3 \sqrt{\frac{M_{v,o}}{a}} [(T-T_M)^2 + C(x_o-x)]^{-\nu_{||}}$$

$$q_o\xi_\perp = q_o/T_3 \sqrt{\frac{M_{t,o}}{a}} [(T-T_M)^2 + C(x_o-x)]^{-\nu_\perp} \qquad x>x_o$$

$$\sigma_o = kT/aT_3[(T-T_M)^2 + C(x_o-x)]^{-\alpha} \qquad (7.17)$$

Notice that the apparent doubling of critical exponents for $x=x_o$ is inherent in (7.16) & (7.17). The data in Fig. 7.5 & 7.6, where $x<x_o$ were fitted to (7.16). $q_o \cdot \sqrt{M_{v,o}}/a$, $q_o \cdot \sqrt{M_{t,o}}/a$ and kT/a were allowed to vary for each dataset, while $\nu_{||}, \nu_{\perp}$ and γ were constrained to be independent of x. The result for the exponents $\nu_{||}, \nu_{\perp}$, and γ is:

$$\nu_{||} = 0.667 \pm 0.011; \quad \nu_{\perp} = 0.553 \pm 0.038; \quad \gamma = 1.114 \pm 0.036$$

Using these exponents, the data in Figure 7.5 where $x > x_o$ were fitted to (7.17) ΔT, T_c and T_M were taken from experiment. ΔT is the temperature difference between the N-Sm-A transition and the N*-Sm-A transition. T_M were taken to be 15.15°C for mixture No. 5 and 15.55°C for mixture No. 6, T_M for mixture No. 5 is 0.4°C smaller than the value for mixture No. 6; this is an experimental fact, which is not understood. The result of the fit is shown as the curves on Figures 7.5 & 7.6 and the fit parameters are given in Table 7.3.

Even though the expressions (7.16) & (7.17) have been derived using the theoretical prediction of a parabolic phase boundary of form (7.7), which have been found not to fit the data rigorously, the expressions (7.16) & (7.17) nevertheless accounts quantitatively for all of the striking properties of the phase-diagram. Only the nonuniversality of the fit parameters is in discrepancy with the theory. It should be noted that in the study of the 6OCB-8OCB mixture a similar discrepancy is found.

Table 7.3. The result of the fitting of $q_o\xi_{||}$, $q_o\xi_{\perp}$ and σ_o to the theoretical prediction. The uncertainty is one standard deviation.

	$x < x_o$								$x > x_o$	
	N→ SmA				N*→ SmA					
MIXT. #	1	2	3	4	1	2	3	4	5	6
$T_c/^oC$	26.41	25.41	22.06	18.0	7.0	8.0	10.43	13.0	-	-
$\frac{q_o}{T_3}\sqrt{\frac{M_{V,O}}{a}}$	1864±70	2314±100	1608±62	2072±84	1810±72	2474±95	2143±80	2563±115	1860±20	2230±26
$\frac{q_o}{T_3}\sqrt{\frac{M_{t,C}}{a}}$	139±16	164±22	120±16	157±21	110±13	151±18	137±17	158±24	126±2	157±2
$\frac{kT}{aT_3}$	4967±486	9615± 1189	5360±573	7742±911	3518±311	10140± 807	7407±750	10051± 1332	16460± 560	7478±294

7.4. Conclusions

The flow studies of the mixture[3]) ascertained that the orientational order and the continuous translational symmetry along the director is restored in the reentrant nematic phase. The present study (see Figures 7.5 & 7.6) provide further evidence for the similarity of the two nematic phases. Figure 7.5 shows that the correlation lengths, characterizing the size of the smectic regions, continuously forming and disappearing in the nematic matrix, essentially display the same behaviour in the two nematic phases. There are only minor quantitative differences, as evidenced by Table 7.3, so generally this study confirms that the idea of the existence of an optimum density for smectic ordering provides a correct description of the reentrant nematic to smectic-A phase diagram. Furthermore, the whole set of correlation length-data could be fitted to the simple expressions derived by A.R. Kortan et al., thus accounting for the crossover effects and the increased bare correlation lengths.

It was found that $\nu_{||} > \nu_{\perp}$, which is also seen in pure bilayer compounds. Furthermore, the numerical values are quite close to bilayer compound values. The same is not true for γ which is lower than bilayer values, which are ~ 1.3.

Lastly, it is worth noting that in this ternary mixture the phase diagram is well described only <u>locally</u> by the parabola predicted by Pershan & Prost, whereas over the whole x-range it is described more accurately by a rotated parabola. This is different from the study performed on the mixture 6OCB-8OCB where the phase diagram indeed is well fitted by the predicted parabola.

REFERENCES

1) P.E. Cladis, R.K. Bogardus, W.B. Daniels and G.N. Taylor (1977) Phys. Rev. Lett. 39, 720.
2) D. Guillon, P.E. Cladis and J. Stamatoff (1978) Phys. Rev. Lett. 41, 1598.
3) S. Bhattacharya, S.V. Letcher (1980) Phys. Rev. Lett. 44, 414.
4) P.S. Pershan, J. Prost (1979) J. Phys. Lett. Orsay Fr. 40, 27.
5) A.R. Kortan, H.V. Kanel, R.J. Birgeneau, J.D. Litster (1981) Phys. Rev. Lett. 47, 1206.

8. THE SMECTIC-A PHASE

As mentioned in Chapter 2, there exists no clear-cut microscopic model for the smectic-A phase which can explain the extremely weak higher-order reflections. A few attempts to explain this unusual effect[1),2)] are known, but none of them include the effect of the proposed Landau-Peierls state of the smectic-A phase and, furthermore, they are quite different. It is the purpose of this chapter to provide a frame for discussing different models of the smectic-A phase on the basis of generally accepted assumptions.

The experimental fact one must try to explain is that essentially all liquid crystal materials, exhibiting a smectic-A phase, display extremely weak higher-order reflections[3)]. If $I(00\ell)$ denotes the peak intensity of the ℓ'th order reflection, then $I(001)/I(002) \simeq 10^{-4}$.

8.1. General model

In order to give an expression for $I(00\ell)$, which can provide the basis for discussing various models of the smectic-A phase and especifically the ratio $I(001)/I(002)$, one must impose a number of assumptions. These are:

a) The smectic-A phase consists of a regular stack of layers.
b) The basic building block (B.B.B.) of the smectic-A phase is one molecule (monolayer smectic-A's) or an overlapping configuration of two molecules (bilayer smectic-A's).
c) On the average each layer contains N_L centres of gravity of B.B.B.'s, distributed randomly in the plane of the layer.
d) Any thermal motion of a B.B.B. as a whole, apart from the layer displacement $u(z)$ introduced in Chapter 2, is neglected.

e) The layers of the smectic-A phase perform harmonic oscillations around average positions.
f) The phases of different modes of u(z) are uncorrelated.
g) The B.B.B. remains perpendicular to the layer at any point.
h) g) means that the principal axis of the B.B.B. or $\hat{n}(\vec{r})$, will not be parallel to the z-axis for a transverse undulation mode, as shown in Chapter 2 (Fig. 2.3). This effect is neglected.

The following figure plus the above-mentioned assumptions provide a general model for the smectic-A phase. Within this model is should be possible to discuss the (00ℓ)-line shape.

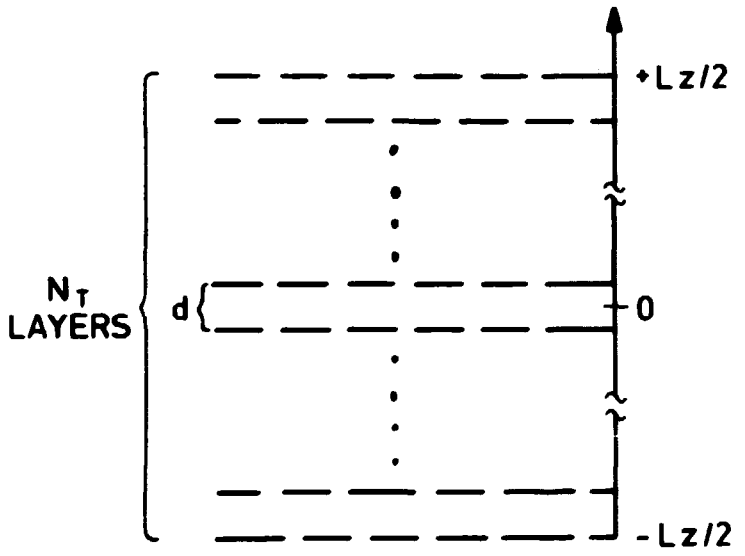

Fig. 8.1. The layering of the smectic-A phase.

The distribution of the centre positions of the B.B.B. along the z-direction will be described by the function P(z), defined by:

$P(z) \cdot dz$ = (No. of B.B.B. with centre-pos. between $z \rightarrow z+dz)/N_L$.

Note that the density $\rho(z) = N_L \cdot P(z)$.

Simple properties of P(z) are:

$$\text{i)} \int_{-d/2}^{+d/2} P(z)dz = 1 \qquad \text{ii)} \int_{-L_z/2}^{+L_z/2} P(z)dz = N_T \tag{8.2}$$

8.2. The scattering cross-section

With the definitions in the previous section it is possible to write down an expression for the scattered intensity at $\vec{q}_\ell$:

$$I(\vec{q}_\ell) \propto \left\langle \int_\Omega n(\vec{r}) \cdot e^{i\vec{q}_\ell \vec{r}} d\vec{r} \right\rangle^2 \; ; \quad \vec{q}_\ell = (0,0,\ell \cdot q_o) \tag{8.2}$$

$n(\vec{r})$ is the electron density ; $q_o = \frac{2\pi}{d}$

Inserting $n(\vec{r}) = \sum_{i'} n_{i'}(\vec{r} - \vec{R}_{i'})$ where $\vec{R}_{i'}$ = pos. of atom i' and the sum is over all atoms, gives further:

$$I(\vec{q}_\ell) \propto \left\langle \sum_{i'} f_{i'} \cdot e^{i\vec{q}_\ell \cdot \vec{R}_{i'}} \right\rangle^2 =$$

$\left\langle \sum_{i'} f_{i'} \cdot e^{iq_\ell z_{i'}} \right\rangle^2$; where $f_{i'}$ is the atomic form factor, and $z_{i'}$ the z-position of atom i'.

Inserting $z_{i'} = z_n + u(z_n) + z_{c,j} + z_{j,i}$, where:

z_n = average position of the center of the n'th layer.

$u(z_n)$ = thermal deviation of n'th layer from its average position.

$z_{c,j}$ = position of an appropriately defined center of the j'th B.B.B. relative to the layer center.

$z_{j,i}$ = position of atom i relative to the above-mentioned center of the j'th B.B.B.

gives:

$$I(\vec{q}_\ell) \propto \left(\sum_i f_i\, e^{iq_\ell z_{j,i}}\right)^2 \cdot \left(\sum_j e^{iq_\ell z_{c,j}}\right)^2 \cdot \left\langle \sum_n e^{iq_\ell (z_n + u(z_n))} \right\rangle^2 \tag{8.3}$$

$$\equiv \quad (f(q_\ell))^2 \quad \cdot \quad (O(q_\ell))^2 \quad \cdot \quad (L(q_\ell))^2$$

where

$(f(q_\ell))^2 \equiv \left(\sum_i f_i\, e^{iq_\ell z_{j,i}}\right)^2$ is a molecular form factor term

sum over all atoms in one B.B.B.

or rather a B.B.B. form factor term.

$(O(q_\ell))^2 \equiv \left(\sum_{j=1}^{N_\ell} e^{iq_\ell z_{c,j}}\right)^2$ is an intralayer order term.

sum over all B.B.B. in one layer

$L(q_\ell))^2 \equiv \left\langle \sum_{n=1}^{N_T} e^{iq_\ell (z_n + u(z_n))} \right\rangle^2$ is a Landau-Peierls term.

sum over all layers

8.3. The Landau-Peierls term

$(L(q_\ell))^2$ has been calculated in Appendix A and the result is

$$(L(q_\ell))^2 = \int e^{i\vec{q}_\ell \cdot \vec{r}} \cdot G(\vec{r})d\vec{r} \quad ; \quad \text{where}$$

$$G(\vec{r}) = e^{-2\gamma\eta} \left(\frac{2d}{\ell 2\pi}\right)^{2\eta} \cdot \left(\frac{1}{\rho}\right)^{2\eta} \cdot e^{-\eta E_1 \left(\frac{\rho^2}{4\lambda z}\right)} \qquad (8.4)$$

$$\rho^2 = x^2 + y^2 \; ; \; \gamma = \text{Euler's const.} = 0.577 \; ; \; \eta = \frac{k_B T \cdot q_o^2 \ell^2}{16\pi \bar{B}\lambda}$$

8.4. The molecular form factor term

$(f(q_\ell))^2$ can be calculated simply by performing the summation, and it is easily done for a number of materials. I have chosen the compounds CBOOA, 8OCB, 8CB, $\bar{8}$S5 and 4O.8, that is, 3 bilayer compounds and 2 monolayer compounds.

Apart from general assumptions a) - h), the following assumptions and/or approximations are made in the calculation.

a) The interatomic distances are the ones obtained from the crystalline phase of CBOOA.[4)]
b) The molecule is rigid. For bilayer smectic-A compounds the tail and head are at angle V with respect to each other and the tail is parallel to the z-direction in the smectic-A phase. The same is assumed for the monolayer compounds.
c) The z-coordinates of all the hydrogen atoms are set equal to those of the carbon atoms to which they are attached.
d) All the atomic form factors are set equal to the number of electrons in the atom, as the scattering angle is small $q_o/k \approx 1/20$ for Cukα-radiation.

In Figure 8.2 a CBOOA-molecule with interatomic distances and angles is given for reference.

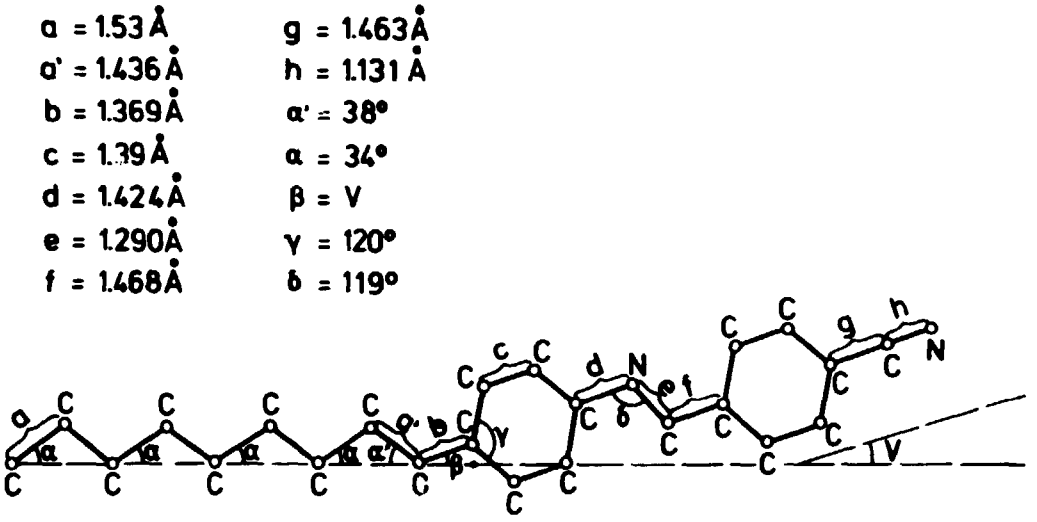

Fig. 8.2. CBOO'-molecule from reference[4]. Average values for a, c, α and γ are used in the calculations, since these values deviate less than 5% from the average value.

It is clear that $f(q_\ell)$ is sensitive only to changes in the z-position of the atoms. I have assumed that the two basic mechanisms to provide this are variation of the angle V and, for bilayer compounds, variation of the overlap parameter δ as defined in Figure 8.3, where the unit cell is shown for 8CB.

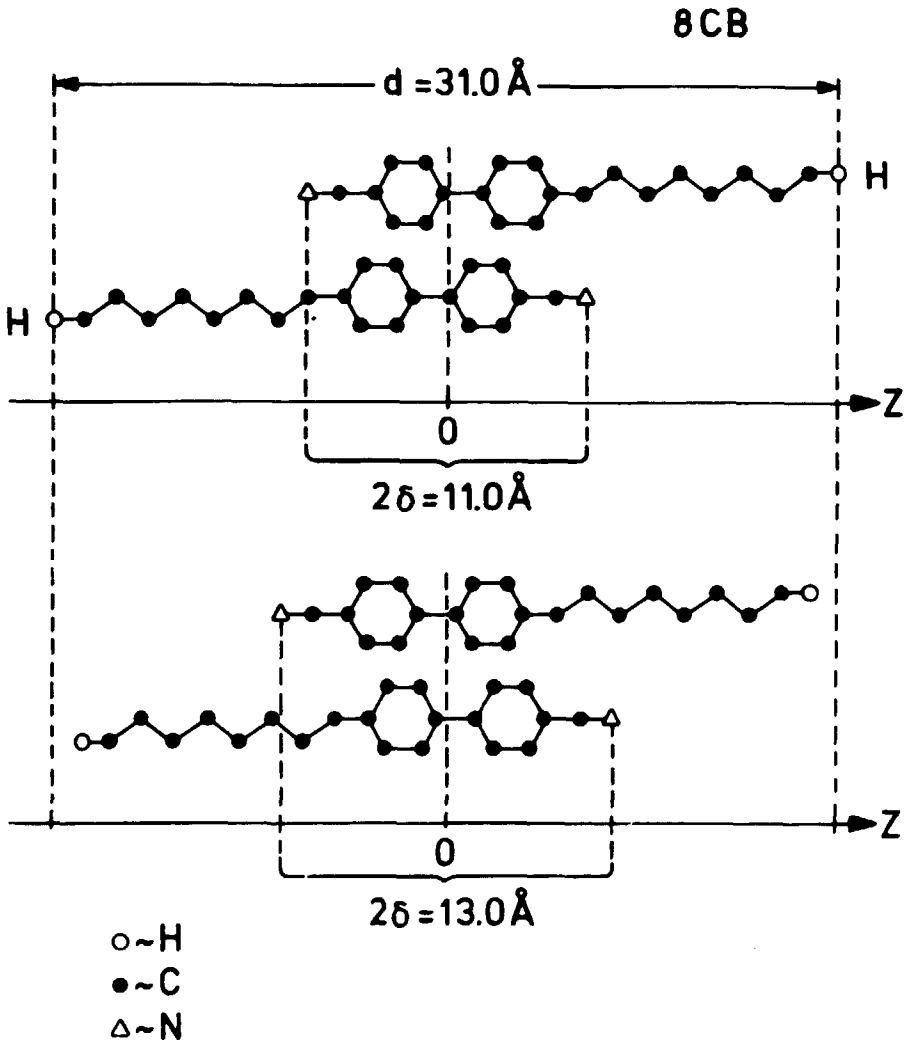

Fig. 8.3. 8CB in the unit cell for δ = 5.5. Å and δ = 6.5 Å. The C-H-distance in the end of the tails have been set to 1 Å (from the CBOOA crystalline phase).

The symmetric structure of bilayer compounds makes it quite easy to calculate $f(q_\ell)$:

$$f(q_\ell) = \sum_i f_i e^{iq_\ell z_{j,i}} =$$

$$\sum_{i,\text{TAIL 1}} f_i e^{iq_\ell (z_{\text{TAIL 1}} + z'_{j,i})} + \ldots \text{ (sums over other parts of molecule 1)}$$

$$+ \sum_{i,\text{TAIL 2}} f_i e^{iq_\ell (z_{\text{TAIL 2}} + z'_{j,i})} + \ldots \text{ (sums over other parts of molecule 2)}$$

$$= (z_{\text{TAIL 2}} = -z_{\text{TAIL 1}})$$

$$2 \cdot \cos(q_\ell \cdot z_{\text{TAIL}}) \cdot \sum_{i,\text{TAIL}} f_i e^{iq_\ell z'_{j,i}} + \ldots \text{ (similar terms for other parts of the molecule)}$$

z_{TAIL} is the z-position of an appropriately defined center of a tail, etc.

This means that if sums like $\sum_{i,\text{TAIL}} f_i e^{iq_\ell z'_{j,i}}$ have been calculated once for basic constituents like C_8H_{17} - TAIL, Benzene ring, N-C-links, etc., then it is quite easy to calculate $f(q_\ell)$ for different bilayer compounds. For monolayer compounds this cannot be done, but in any case it is a simple procedure to write a computer program performing the full summation.

The result of the calculation is displayed in Figures 8.4, 8.5 & 8.6. As is evident from the figures, the following are the main conclusions to be drawn from the calculation:

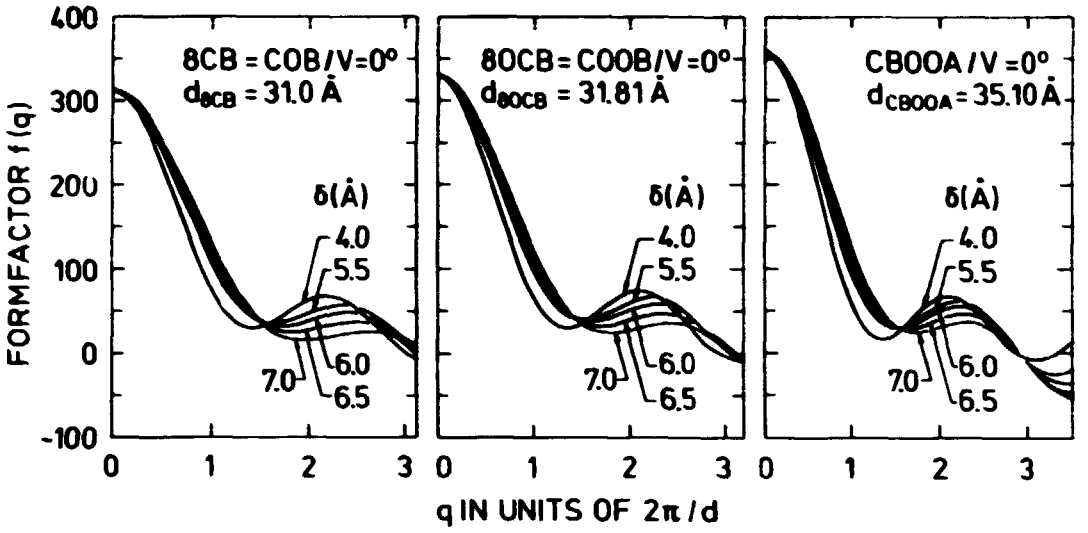

Fig. 8.4. f versus q(units of $(2\pi)/(d)$) for the three bilayer compounds 8CB, 8OCB and CBOOA and various overlapparameters. V = 0.

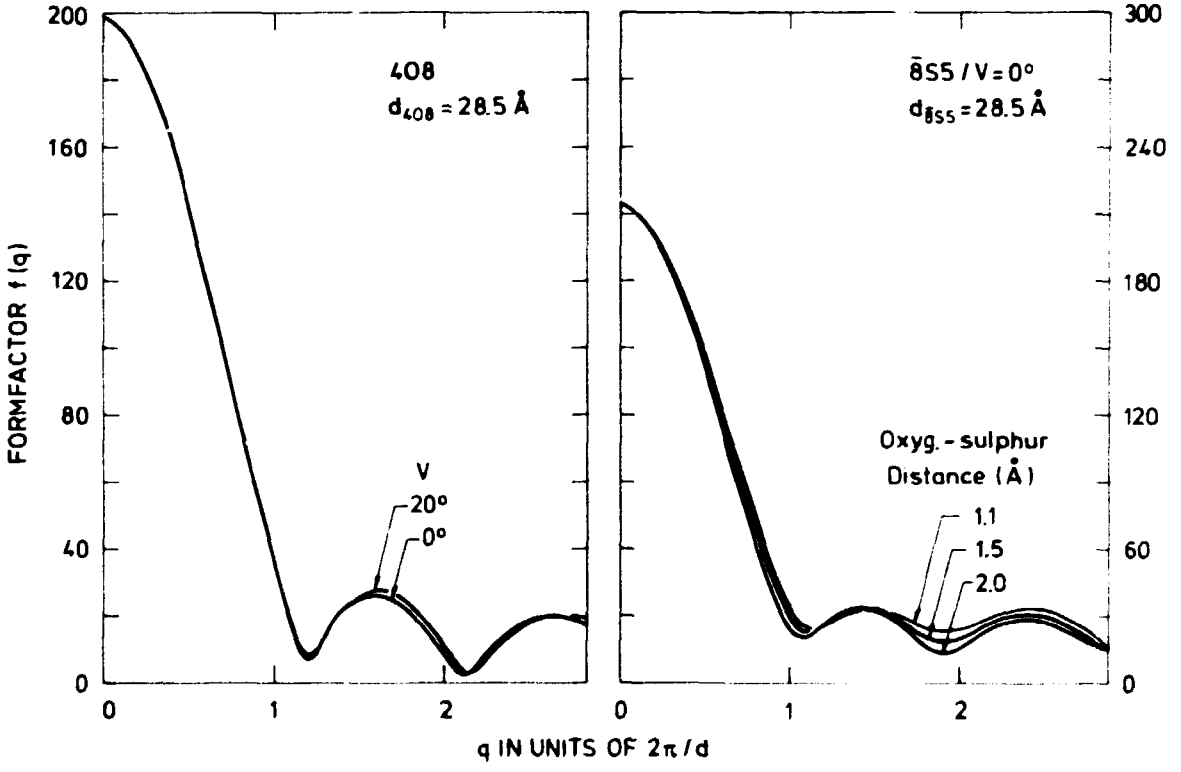

Fig. 8.5. f versus q(units of $(2\pi)/(d)$) for the two monolayer compounds 40.8 and $\bar{8}$S5. For 40.8 two curves are shown, one for V = 0 and one for V = 20. For $\bar{8}$S5 three curves are shown, each having a different oxygen-sulphur-distance. This distance is unknown, since it does not occur in crystalline CBOOA.

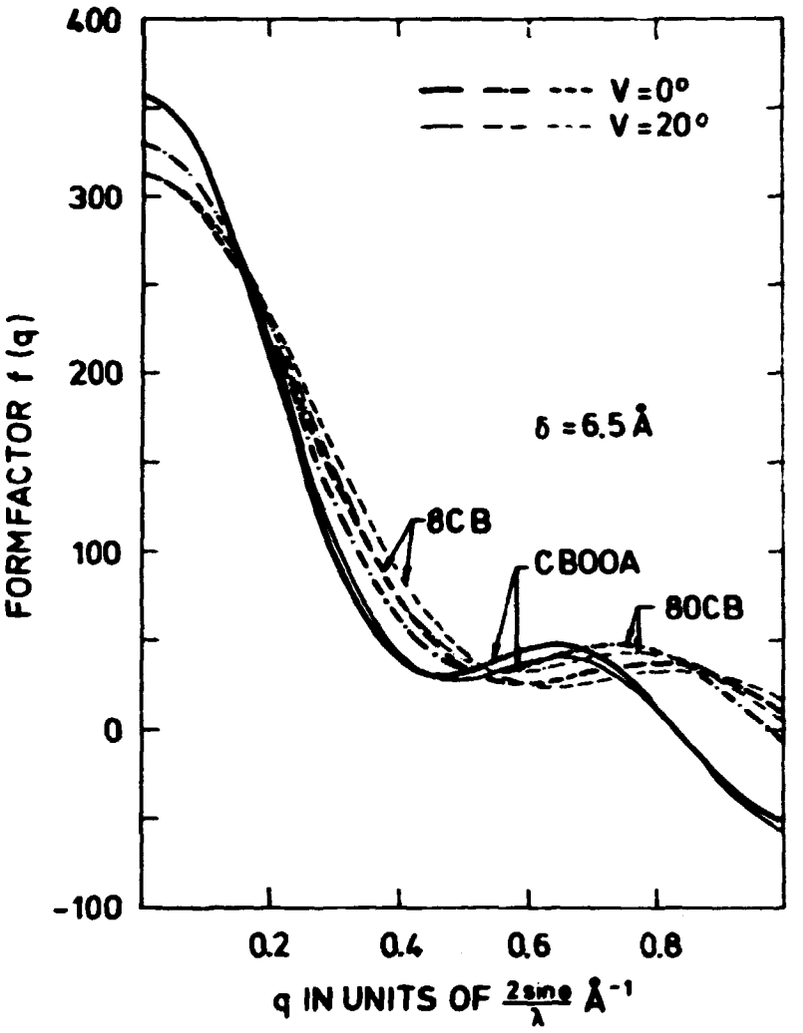

Fig. 8.6. The three bilayer compounds for one specific overlap (δ = 6.5 Å) and two values of V. V = 0^{o} and V = 20^{o}.

Although the general feature of the $f(q_{\ell})$-curves are rather similar, especially within the two categories of bilayer and monolayer compounds, then it is obvious that there is a pronounced δ-dependence for the bilayer compounds, whereas the V-dependence is less marked for all compounds. As a specific example we look at 8CB and compare the δ = 5.5 Å-curve with that of δ = 6.5 Å. The latter corresponds to a rather large overlap

of the benzene rings the former to a configuration, where the total length of the two overlapping molecules is equal to the d-spacing of the smectic-A phase (see Figure 8.3). To get a quantitative measure for the difference between these two curves, one can look at the ratio $(f(q_1)/f(q_2))^2$. From the calculation one gets, for V = 0:

$$[f(q_1)/f(q_2)]^2 = 20.7 \text{ for } \delta = 5.5 \text{ Å}$$

$$[f(q_1)/f(q_2)]^2 = 5.4 \text{ for } \delta = 6.5 \text{ Å}$$

As can be seen from Figure 8.3, I have taken the value d = 31.0 Å in order to compare with Ref. (1). It turned out that the value for $[f(q_1)/f(q_2)]^2$ (δ = 6.5 P, V = 0^o) from this reference, namely 17.54, is obtained by omitting all the hydrogen atoms, therefore yielding the difference. What is crucial to note is the rather large difference one obtains by shifting the molecules a distance as small as 1Å relative to each other.

8.5. The intralayer order term

The last term in the expression for $I(q_\ell)$, $(O(q_\ell))^2$ is not a priori given. It is necessary to assume a particular distribution of B.B.B. along the normal layer, and one can express $O(q_\ell)$ in terms of P(z) in the following way:

$$O(q_\ell) \equiv \left\langle \sum_{j=1}^{N_L} e^{iq_\ell z_{c,j}} \right\rangle = N_L \cdot \left\langle \int_{-d/2}^{d/2} e^{iq_\ell z} P(z)dz \right\rangle \qquad (8.5)$$

It is in the choice of P(z), the actual modelling of the smectic-A phase takes place.

To exemplify, one can calculate $O(q_\ell)$ for different P(z)'s:

1) $\underline{P(z) = \delta(z-nd)}$; n = 0, 1, ..., corresponding to perfect line-up of all B.B.B.-centers ~ usual text-book picture of the smectic-A phase,

$O(q_\ell) = N_L$ (independent of q_ℓ)

2) $\underline{P(z) = 1/d}$; corresponds to total smearing out of B.B.B.-centers, that is in fact a nematic phase

$O(q_\ell) = 0$ as expected

3) $P(z) = \frac{1}{\sqrt{2\pi}\sigma_z} \cdot e^{-(\frac{z}{2\sigma_z})^2}$; corresponding to a

---

Gaussian distribution of B.B.B.

$O(q_\ell) = N_L \cdot e^{-(q_\ell <\sigma_z>)^2}$ for $\sigma_z << d$

4) $P(z) = \sum_{\ell=0}^{\infty} a'_\ell \cos(\ell q_0 z)$; $a'_0 = 1/d$.

$P(z) = 1/d(1+a_1\cos(q_0 z)+a_2\cos(2q_0 z)+...$
$+a_N\cos(Nq_0 z)+...)$

corresponding to a Fourier expansion of the B.B.B.-density.

$O(q_\ell) = N_L \cdot \frac{<a_\ell>}{2}$ for $q_\ell = \ell \cdot q_0$; $\ell = 1, 2, ...$

a_1 in Example 4 can be related to the smectic-order parameter ψ, which is introduced by De Gennes (see Chapter 2). This is obvious by using that:

$$\rho(z) = N_L \cdot P(z) = \frac{N_L}{d} \cdot (1 + a_1\cos(q_o z) + \ldots + a_N\cos(Nq_o z) + \ldots)$$

Fourier expansion of P(z), Example 4

$$= \rho_o(1 + a_1\cos(q_o z) + \ldots) \; ; \; \rho_o = \frac{N_L}{d}$$

Comparing this with $\rho(z) = \rho_o[1 + \mathrm{Re}\{\psi \cdot e^{iq_o z}\}]$ from Chapter 2 yields

$$a_1 = |\psi|$$

with $O(q_\ell) = N_L \langle a_\ell \rangle / 2$ it is clear that there would be no higher-order reflections if all a_ℓ's; $\ell = 2, \ldots,$ are truly zero and only the fundamental reflection would be present with:

$$O(q_\ell) = N_L \frac{\langle |\psi| \rangle}{2}$$

Instead of describing the smectic-A structure via a Fourier expansion of P(z) one could more directly postulate that the smectic-A phase is obtained from the nematic phase by a specific <u>modulation</u> of the centres of the B.B.B. If this modulation is described by:

$$z_j' = f(z_j) \qquad (8.6)$$

where z_j is the <u>random</u> position of the centres of the B.B.B. in the nematic phase and z_j' is the position of the B.B.B. in the modulated smectic-A phase. In the nematic phase $P_N(z) = 1/d$ (Example 2). By the modulation $f(z_j)$ one will obtain a $P_s(z)$, which can be found by the following argument:

The number of B.B.B. in $[z_o;\ z_o + dz_o]$ in the nematic phase = $N_L \cdot 1/d\ dz_o$ will move by the modulation $f(z_o)$ to $[z;\ z + dz]$; where:

$$z = f(z_o) \quad \text{and} \quad \frac{dz}{dz_o} = f'(z_o)$$

This gives via the definition of P(z): $P_s(z) = 1/d \cdot [f'(z_o)]^{-1}$; $z_o = f^{-1}(z)$, which yields:

$$(O(q_\ell))^2 = \langle (\sum_j e^{iq_\ell z_j'})^2 \rangle = \langle (N_L \cdot \int_{-d/2}^{+d/2} e^{iq_\ell f(z_o)} \cdot P_s(z)dz)^2 \rangle$$

$$= \langle (N_L \cdot \frac{1}{d} \int_{-d/2}^{d/2} e^{iq_\ell f(z_o)} \cdot \frac{dz}{f'(z_o)})^2 \rangle$$

$$= \langle (N_L \cdot \frac{1}{d} \int_{-d/2}^{d/2} e^{iq_\ell f(z_o)} \, dz_o)^2 \rangle$$

The simplest modulation giving a layered structure is a sinusoidal modulation:

$$z_j' = z_j + A \cdot \sin(q_o \cdot z_j) \quad ; \quad A < \frac{1}{q_o} \tag{8.7}$$

Yielding:

$$(O(q_\ell))^2 = \langle N_L^2 \, (\frac{1}{d} \int_{-d/2}^{d/2} e^{iq_\ell (z + A\cos(q_o z + \frac{\pi}{2}))} \, dz)^2 \rangle = \tag{8.8}$$

$\underline{N_L^2 [J_\ell(q_\ell \langle A \rangle)]^2}$ (Hansen integral representation of the ℓ'th order Bessel function J_ℓ).

The above sinusoidal modulation approach to the smectic-A phase can of course also be described in terms of a Fourier expansion of P(z) or equivalently, the density. By comparing the expression for $O(q_\ell)$ in Example 4 and above, one immediately finds that the P(z) describing the sinusoidally modulated structure is given by a Fourier expansion:

$$P(z) = \frac{1}{d} \sum_{\ell=0}^{\infty} a_\ell \cdot \cos(\ell \cdot q_o z)$$

where a_ℓ is given by:

$$a_\ell = 2 \cdot J_\ell(q_\ell A)$$

and further:

$$\left.\begin{aligned} |\psi| = a_1 &= 2 \cdot J_1(q_o A) \cong q_o A \\ \text{and} \qquad a_2 &= 2 \cdot J_2(2 \cdot q_o A) \cong (q_o A)^2 \end{aligned}\right\} \text{ for } q_o A << 1 \text{ or } T \lesssim T_c$$

leading to:

$$O(q_1(=q_o)) \approx N_L \frac{\langle\psi\rangle}{2} \text{ and } O(q_2(=2q_o)) = N_L \frac{\langle\psi\rangle^2}{2}$$

for $Aq_o << 1$ or $T \lesssim T_c$.

8.6. Temperature dependence of $I(q_1)/I(q_2)$ close to T_c. An example

It is now possible to investigate the temperature dependence of $I(q_1)/I(q_2)$ close to T_c. One gets:

$$\frac{I(\vec{q}_1)}{I(\vec{q}_2)} = \left(\frac{f(q_1)}{f(q_2)}\right)^2 \cdot \frac{\int e^{i\vec{q}_1\vec{r}} G(\vec{r}) d\vec{r}}{\int e^{i\vec{q}_2\vec{r}} G(\vec{r}) d\vec{r}} \cdot \left(\frac{O(q_1)}{O(q_2)}\right)^2 \qquad (8.9)$$

The first term is temperature independent, but depends rather critically on the overlap parameter δ for bilayer compounds, which is a good argument for picking a monolayer compound for an experimental study.

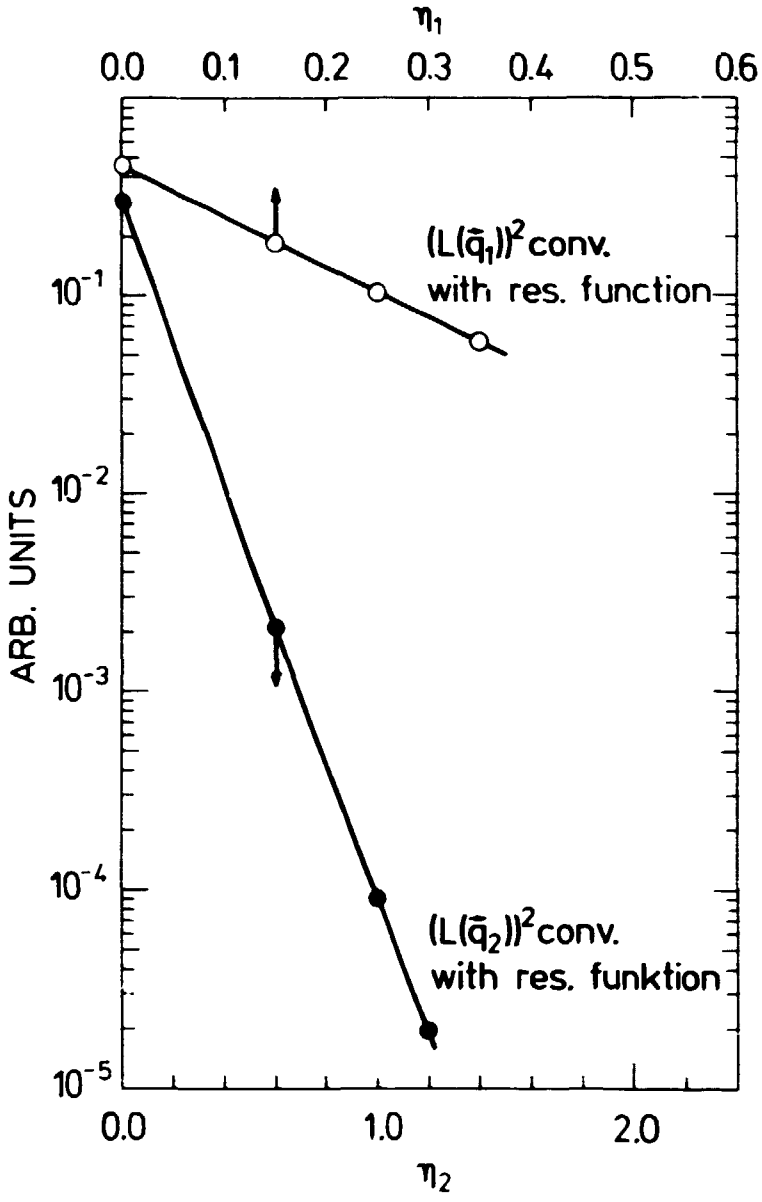

Fig. 8.7. $(L(\vec{q}_1))^2$ and $(L(\vec{q}_2))^2$ convoluted with the resolution function; $\vec{q}_1 = \vec{q}_o$ and $\vec{q}_2 = 2\vec{q}_o$. The difference for $\eta = 0$ indicates that the resolution along $\vec{q}_o$, the longitudinal resolution, is not the same for $\vec{q} = \vec{q}_1$ and $\vec{q} = \vec{q}_2$. This is due to the difference in $(\Delta\lambda)/(\lambda)$-contribution as outlined in Chapter 4. $\eta_2 = 4 \cdot \eta_1$.

$$(L(\vec{q}_\ell))^2 = e^{-2\gamma\eta} \left((2d)/(2\pi\ell)\right)^{2\eta}$$

$$\cdot \int \left((1)/(\rho^2)\right)^{\eta} \cdot e^{-\eta \cdot E_1((\rho^2)/(4\lambda z))} \cdot e^{i\vec{q}_\ell \cdot \vec{r}} \, d\vec{r}.$$

Three η_1-values were chosen 0.15, 0.25 and 0.35. For these values λ was taken from reference 5 to be 3.8, 4.5 and 8.2. The resolution functions at $\vec{q} = \vec{q}_o$ and at $q = 2q_o$ are given in Table 4.2.

The second term can be evaluated, numerically, for a specific experimental set-up. This term is temperature dependent, since η grows as $T \to T_c$.[5)]

The last term can be evaluated when a specific model has been chosen.

As a concrete example 8OCB has been chosen. For this compound the first term is calculated and the result can be taken from Figure 8.4. The second term has been calculated for a specific resolution function. This resolution is typical for the kind of resolution function one can obtain using single crystal

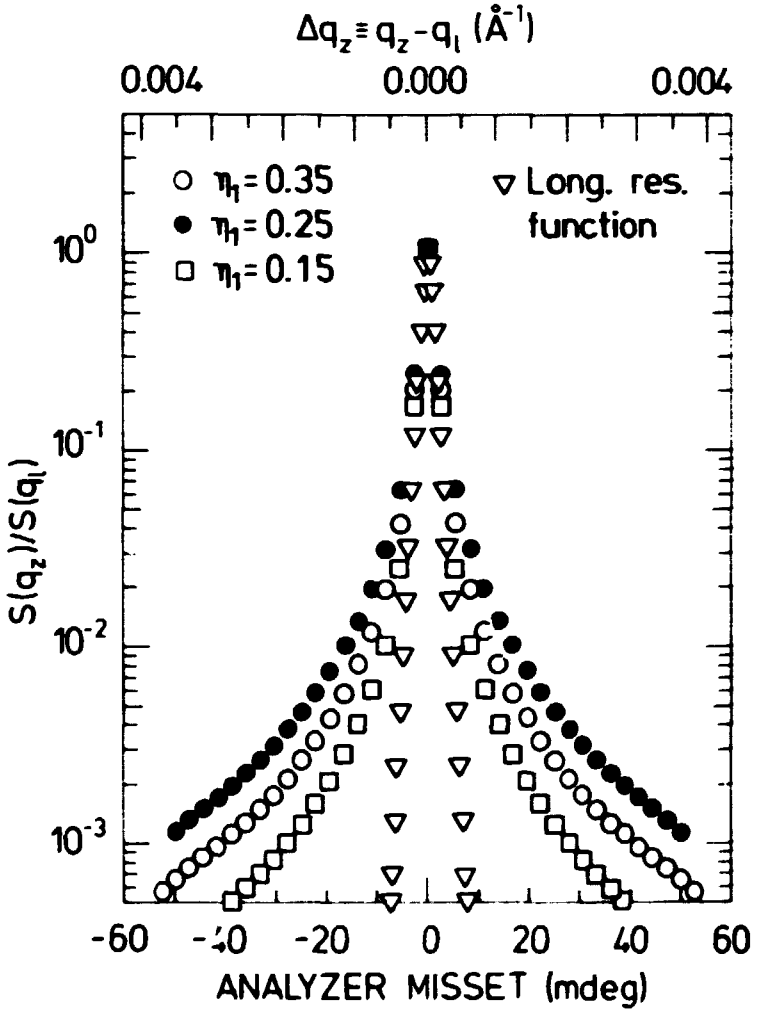

Fig. 8.8. Longitudinal (001)-lineshapes, convoluted the resolution function, for three η-values.

techniques in liquid crystal X-ray diffraction. Chapter 3 is dedicated to a description of these techniques and the resolution used here is described in detail in Chapter 4. The result for the peak value of the numerical convolution of the resolution function and $\int e^{i\vec{q}_t \cdot \vec{r}} G(\vec{r})\, dr$ is shown in Figure 8.7 for a number of η-values in the observed range[5].

In Figure 8.8 the (001)-line shape for scans along $\vec{q}_o$ is shown for different η-values. The resolution function along q_o is also shown. In Figure 8.9 the (001)- and (002)-line shapes are compared for the same value of $\bar{B} \cdot \lambda$ (see Section 8.3.), corresponding to the two η-values $\eta(q_1) \equiv \eta_1 = 0.25$ and $\eta(q_2) \equiv \eta_2 = 4 \cdot \eta_1$.

In terms of the general Fourier expansion of P(z) in Example 4 the term $(O(q_1)/O(q_2))^2$ in (8.9) is:

$$\left(\frac{O(q_1)}{O(q_2)}\right)^2 = \frac{\langle \psi \rangle^2}{\langle a_2 \rangle^2} \tag{8.10}$$

The sinusoidal modulation gives:

$$\left(\frac{O(q_1)}{O(q_2)}\right)^2 = \frac{!}{\langle |\psi| \rangle^2} = C^{-2} \cdot t^{-2\beta} \tag{8.11}$$

Without assuming the sinusoidal modulation McMillan's theory[6] for the smectic-order parameter $\langle |\psi| \rangle$ can be extended to give also $\langle a_2 \rangle$. The result is[1]

$$\langle a_2 \rangle^2 = ((1/2 + \gamma/\alpha)\, \langle \psi \rangle^2)^2 \tag{8.12}$$

where $\gamma/\alpha = 0.5(\alpha/2)^3[1-(\alpha/2)^3]$ and α is McMillan's parameter: $\alpha = 2e^{-\pi r_o/d}$. r_o denotes the length of the rigid head (or for monolayer compounds, the rigid middle section) of the constituent molecules.[1] This gives:

$$\left(\frac{O(q_1)}{O(q_2)}\right)^2 = \frac{(1/2 + \gamma/\alpha)^2}{\langle |\psi| \rangle^2} = (1/2 + \gamma/\alpha)^2 C^{-2} \cdot t^{-2\beta} \tag{8.13}$$

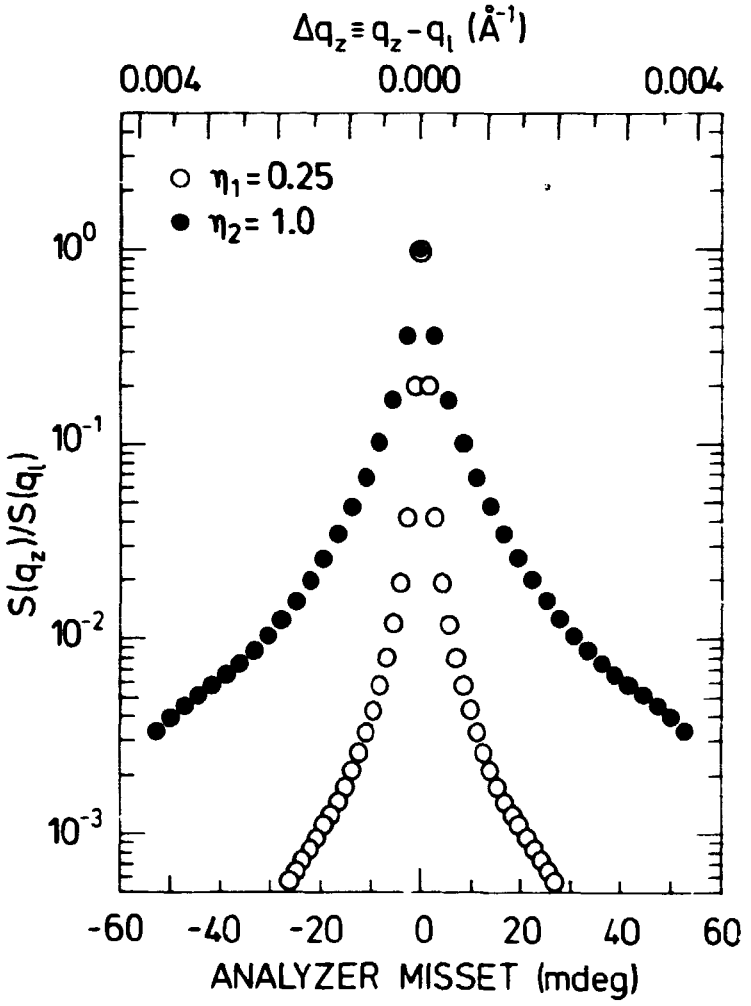

Fig. 8.9. Longitudinal (001)- and (002)-lineshapes, convoluted with the resolution function, for $\eta_1 = 0.25$ and the corresponding $\eta_2 = 1.0$.

The value of C can be obtained from the McMillan theory[1]:

$$C = \sqrt{\frac{1}{(1-2\gamma/\alpha)}} \approx 1.1 \text{ for 8CB, 8OCB \& CBOOA}$$

Thus an extension of the McMillan theory predicts a ratio which differs from the sinusoidal modulation result by a factor $(1/2 + \gamma/\alpha)^2$. This factor is typically 0.3[1] for smectic-A compounds like 8CB, 8OCB, and CBOOA.

8.7. Conclusion

On the basis of calculations such as the ones performed for 8OCB (Figures 8.4 and 8.7), various models for $O(q_\ell)$, and an experimental study it should be possible to elucidate which mechanisms are needed to explain experimental data for a liquid crystal that displays a smectic-A phase. One needs accurate measurements of the (001)- and (002)-line shapes for a number of temperatures close to T_c.

An experimental study must take due account of the multiple scattering that occurs in a sample with mosaicity. The process is shown in reciprocal space in Figure 8.10. Obviously, the multiple scattering contribution depends critically on the mosaicity. To rid oneself of ambiguities, the optimal thing to do is to pick a monolayer compound with a second-order nematic-smectic-A phase transition and learn to grow smectic-A phases with a mosaicity-distribution $<< 1^o$.

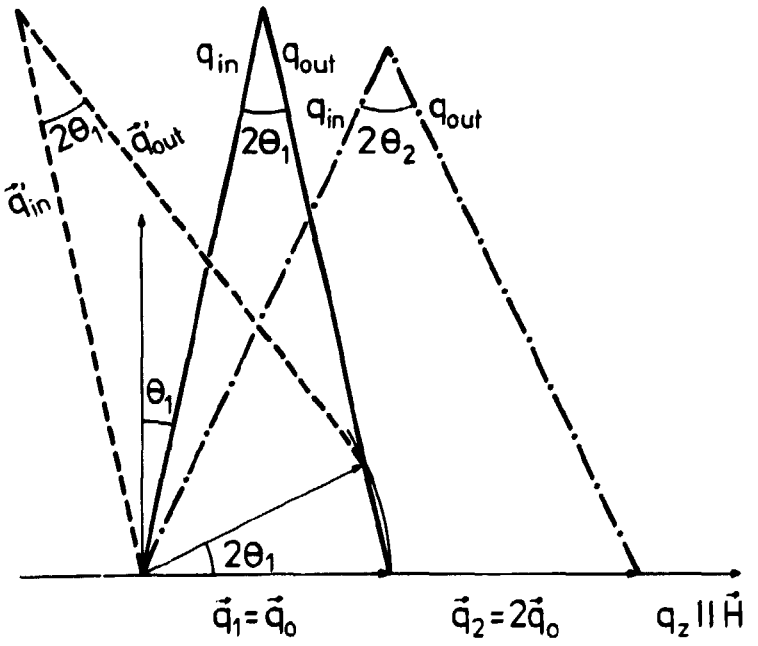

Fig. 8.10. Multiple scattering process in reciprocal space. $\vec{H}$ is aligning field. $|\vec{q}_0| = (2\pi)/(d)$. $\vec{q}'_{IN} \| \vec{q}_{OUT}$. A true second order reflection is also shown.

REFERENCES

1) J. Stamatoff, P.E. Cladis, D. Guillon, M.C. Cross, T. Bilash and P. Finn (1980) Phys. Rev. Lett. 44 1509. (In this letter δ = 6,5 Å and all the hydrogen atoms have beem omitted).

2) A.J. Leadbetter, J.C. Frost, G.W. Gray and A. Mosley (1979) J. Phys. Orsay Fr. 40, 375.

3) J.D. Litster, J. Als-Nielsen, R.J. Birgeneau, S.S. Dana, D. Davidov, F. Garcia-Colding, M. Kaplan, C.R. Safinya and R. Schaetzing (1979) J. Phys. Colloq. Orsay Fr. 40, C3, 339.

4) G.V. Vani and Kalyani Vijayan (1977) Mol. Cryst. Liq. Cryst. 42 249.

5) J. Als-Nielsen, J.D. Litster, R J. Birgeneau, M. Kaplan, C. R. Safinya, A. Lindegaard-Andersen and S. Mathiesen (1980) Phys. Rev. B. 22 312.

6) W.L. McMillan (1971) Phys. Rev. A 4 1238.

APPENDIX A

CALCULATION OF ANOMALOUS SCATTERING SINGULARITIES IN THE SMECTIC-A PHASE, USING THE HARMONIC APPROXIMATION

The model underlying the calculation is the following: The smectic-A phase is assumed to be a regular stack of layers. The layers are assumed to consist of basic building blocks (B.B.B.), which are distributed at random in the plane of the layer. The B.B.B. may be a single molecule (monolayer smectic-A's), or an overlapping configuration of two (bilayer smectic-A's).

Furthermore, the layers are assumed to perform harmonic oscillations around some average position. This oscillation can be described by the thermal average of the square of the Fourier transform of the layer displacement $\langle|u(\vec{q})|^2\rangle$ as obtained by equipartition (Chapter 2):

$$\langle|u(\vec{q})|^2\rangle = \frac{k_B T}{V\bar{B}(q_z^2 + \lambda^2 q_\perp^4)} \qquad (A.1)$$

A fundamental expression for the scattering cross-section is:

$$S(\vec{\kappa}) \propto \langle \Sigma\Sigma_{ij} e^{i\vec{\kappa}\cdot(\vec{R}_i^{\,\prime}-\vec{R}_j^{\,\prime})}\rangle \qquad (A.2)$$

where $\vec{R}_i^{\,\prime}$, $\vec{R}_j^{\,\prime}$ are the positions of the i'th and the j'th layer. Inserting $\vec{R}_i^{\,\prime} = \vec{R}_i + u(\vec{R}_i) \cdot \hat{1}_z$ gives:

$$S(\vec{\kappa}) \propto \langle \sum_{ij} \sum e^{i\vec{\kappa}(\vec{R}_i - \vec{R}_j) + i\kappa_z(u(\vec{R}_i) - u(\vec{R}_j))} \rangle$$

$$= N \cdot \sum_i e^{i\vec{\kappa}\cdot\vec{R}_i} \langle e^{i\kappa_z(u(\vec{R}_i) - u(\vec{o}))} \rangle \qquad (A.3)$$

↑ translation symmetry

In the harmonic approximation, one gets further:

$$S(\vec{\kappa}) \propto N \cdot \sum_i e^{-i\vec{\kappa}\cdot\vec{R}_i} \cdot e^{-1/2\kappa_z^2 \cdot \langle (u(\vec{R}_i) - u(\vec{o}))^2 \rangle} \qquad (A.4)$$

On inserting the Fourier expansion of $u(\vec{R}_i)$ and assuming that the phases of the different modes of $u(\vec{R}_i)$ are uncorrelated, we obtain:

$$S(\vec{\kappa}) \propto N \cdot \sum_i e^{i\vec{\kappa}\vec{R}_i} \cdot e^{-1/2\kappa_z^2 \sum_{\vec{q}} \langle |u(\vec{q})|^2 \rangle (1 - \cos(\vec{q}\cdot\vec{R}_i))}$$

Replacing $\sum_{\vec{q}}$ by $\frac{V}{(2\pi)^3} \int d\vec{q}$ gives:

$$S(\vec{\kappa}) \propto N \cdot \sum_i e^{i\vec{\kappa}\cdot\vec{R}_i} \cdot e^{-1/2\kappa_z^2 [\frac{V}{(2\pi)^3} \int \langle |u(\vec{q})|^2 \rangle (1-\cos(\vec{q}\cdot\vec{R}_i)) d\vec{q}]}$$

Shifting to the continuous variable $\vec{r}$ instead of $\vec{R}_i$ gives:

$$S(\vec{\kappa}) \propto N \cdot \int e^{i\vec{\kappa}\cdot\vec{r}} \cdot e^{-1/2\kappa_z^2 \cdot I(\vec{r})} d\vec{r} \equiv$$

$$N \cdot \int e^{i\vec{\kappa}\cdot\vec{r}} G(\vec{r}) d\vec{r} \qquad (A.5)$$

where $I(\vec{r}) \equiv \frac{V}{(2\pi)^3} \cdot \int \langle |u(\vec{q})|^2 \rangle \cdot (1-\cos(\vec{q}\cdot\vec{r})) d\vec{q}$ and

$$G(\vec{r}) = e^{-1/2\kappa_z^2 \cdot I(\vec{r})}$$

Note that the calculation so far has been exactly parallel to that of normal thermal diffuse scattering. But from now on it differs, since an expansion of the exponential term $e^{-1/2\kappa_z^2 \cdot I(r)}$ is <u>not</u> justified here.

Inserting $\langle |u(\vec{q})|^2 \rangle$ into $I(\vec{r})$ gives:

$$I(\vec{r}) = \frac{k_B T}{\bar{B}(2\pi)^3} \cdot \int \frac{1-\cos(\vec{q}\cdot\vec{r})}{q_\pi^2 + \lambda^2 q_\perp^4} dq_{||} dq_{\perp,1} dq_{\perp,2} \qquad (A.6)$$

$$= \frac{k_B T}{\bar{B}(2\pi)^3} \cdot \int \frac{1-e^{i\vec{q}\cdot\vec{r}}}{q_\pi^2 + \lambda^2 q_\perp^4} d\vec{q} \equiv A \cdot J(\vec{r})$$

↑
even numerator in integrand

In an infinite sample the only cut-off in $J(\vec{r})$ is $q_{||,min} = -2\pi n/d$ and $q_{||,max} = 2\pi n/d$ and $|q_{\perp,max}| = 2\pi n/d$ where n is the order of the reflection.

For the q_π-integration $q_{||,max}$ can be changed to ∞ and $q_{||,min}$ to $-\infty$. The q_π-integration can then be done by a residue-calculation. The q_π-integral is:

$$J_n(\vec{r}) = \int_{-\infty}^{+\infty} \frac{1-e^{i(q_n \cdot z + \vec{\rho} \cdot \vec{q}_\perp)}}{q_n^2 + \lambda^2 q_\perp^4} \, dq_n \qquad (A.7)$$

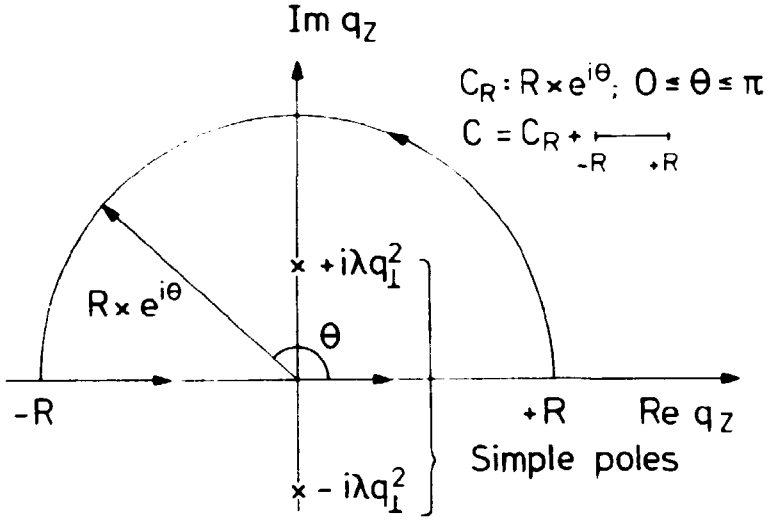

Fig. A. Integration path in the imaginary plane

Performing the contour integral along the curve C shown beneath gives:

$$\int_C = 2\pi i \; \Sigma \text{ resid} = \int_{C_R} + \int_{-R}^{+R} = \int_{C_R} + J_n(\vec{r})$$

For $R \to \infty$ $\int_{C_R} \to 0$ and $\int_{-\infty}^{+\infty} = 2\pi i \; \Sigma$ resid =

$$2\pi \cdot \frac{1-e^{-\lambda q_\perp^2 z + i\vec{\rho}\cdot\vec{q}_\perp}}{2\lambda q_\perp^2} \text{ and one gets:}$$

$$J_n(\vec{r}) = \pi \cdot \frac{1-e^{-\lambda q_\perp^2 z + i\vec{\rho}\cdot\vec{q}_\perp}}{\lambda q_\perp^2} \qquad (A.8)$$

Inserting $dq_{\perp,1} \cdot dq_{\perp,2} = q_\perp d\vartheta dq_\perp$ and using the Hansen integral expression for J_o (the zero'th Bessel function):

$$J_o(x) = \frac{1}{2\pi} \cdot \int_o^{2\pi} e^{ix\cos\vartheta} d\vartheta$$

gives, when integrating over ϑ:

$$\vec{J(r)} = \frac{2\pi^2}{\lambda} \int_o^{q_{\perp,max}} \frac{1}{q_\perp} (1 - e^{-z\lambda q_\perp^2} J_o(q_\perp \rho)) dq_\perp$$

$$= \frac{2\pi^2}{\lambda} \cdot \int_o^{q_{\perp,max}} \left[\frac{1}{q_\perp} - \frac{e^{-z\lambda q_\perp^2}}{q_\perp} \cdot \sum_{n=o}^{\infty} \frac{(-1)^n}{(n!)^2} \left(\frac{q_\perp^2 \rho^2}{4}\right)^n \right] dq_\perp$$

power series expansion of $J_o(q_\perp \cdot \rho)$

$$= \frac{2\pi^2}{\lambda} \left[\int_o^{q_{\perp,max}} \left(\frac{1-e^{z\lambda q_\perp^2}}{q_\perp}\right) dq_\perp \right.$$

$$\left. - \sum_{n=1}^{\infty} \frac{(-1)^n}{(n!)^2} \left(\frac{\rho^2}{4}\right)^n \cdot \frac{1}{2} \int_o^{q_{\perp,max}^2} (q_\perp^2)^{n-1} \cdot e^{-z\lambda q_\perp^2} d(q_\perp^2) \right]$$

The last integral is known and is given by:

$$\int_o^{q_{\perp,max}^2} x^{n-1} e^{-z\lambda x} dx = \left[e^{-\lambda x} \cdot \sum_{i=o}^{n-1} (-1)^i \frac{(n-1)! x^{n-1-i}}{(n-1-i)!(-z\lambda)^{i+1}} \right]_o^{q_{\perp,max}^2}$$

$$\rightarrow \frac{(n-1)!}{(\lambda a)^n} \text{ for } z\lambda q_{\perp,max}^2 >> 1.$$

Inserting this limit yields:

$$J(\vec{r}) = \frac{2\pi^2}{\lambda}\left[\int_0^{q_{\perp,max}} \left(\frac{1-e^{\lambda z q_\perp^2}}{q_\perp}\right) dq_\perp - \sum_{n=1}^{\infty} \frac{(-1)^n}{(n!)^2}\left(\frac{\rho^2}{4}\right)\frac{1}{2}\cdot\frac{(n-1)!}{(z\lambda)^n}\right]$$

$$= \frac{\pi^2}{\lambda}\left[2\cdot\int_0^{q_{\perp,max}} \frac{(1-e^{\lambda z q_\perp^2})}{q_\perp} dq_\perp + \gamma + \ln\left(\frac{\rho^2}{4\lambda z}\right) + E_1\left(\frac{\rho^2}{4\lambda z}\right)\right]$$

power series expansion of exponential integral $E_1(x) \equiv \int_x^{\infty} \frac{e^{-t}}{t}\, dt.$ (A.9)

$\gamma \equiv$ Euler const. The last integral can be evaluated in the following way:

$$2\cdot\frac{1}{2}\int_0^{q_{\perp,max}^2} \frac{(1-e^{\lambda z q_\perp^2})}{q_\perp^2}\, d(q_\perp^2) = \int_0^{\lambda z q_{\perp,max}^2} \frac{(1-e^{-t})}{t}\, dt$$

$$= \left[\ln(\lambda z q_{\perp,max}^2) + \gamma + E_1(\lambda z q_{\perp,max}^2)\right] \qquad (A.10)$$

"Handbook of mathematical functions" ed. by Abramowitz & Segun p. 230,

which finally gives ($E_1(x) \to 0$ for $x \gg 1$) for $\lambda z q_{\perp,max}^2 \gg 1$:

$$J(\vec{r}) = \frac{\pi}{\lambda}\left[\ln(\lambda z q_{\perp,max}^2) + 2\gamma + E_1\left(\frac{\rho^2}{4\lambda z}\right) + \ln\left(\frac{\rho^2}{4\lambda z}\right)\right] \qquad (A.11)$$

$$= \frac{\pi^2}{\lambda}\left[2\gamma + \ln\left(\frac{\rho^2 \cdot q_{\perp,max}^2}{4}\right) + E_1\left(\frac{\rho^2}{4\lambda z}\right)\right]$$

Inserting $J(\vec{r})$ into $I(\vec{r})$ (A.6) and thereafter $I(\vec{r})$ into $G(\vec{r})$ (A.5) gives:

$$G(\vec{r}) = \left(\frac{\rho \cdot q_{\perp,max}}{2}\right)^{-2\cdot\eta} \cdot e^{-\eta \cdot E_1}\left(\frac{\rho^2}{4\lambda z}\right) \qquad (A.12)$$

where

$$\eta = \frac{\kappa_z^2 \cdot k_B T \pi^2}{\overline{B} \cdot (2\pi)^3 \cdot 2\lambda} = \frac{k_B T \cdot \kappa_z^2}{16\pi \overline{B}\lambda} \qquad (A.13)$$

Inserting

$\kappa_z \approx nq_o = n\frac{2\pi}{d}$ and $q_{\perp,max} = \frac{2\pi n}{d}$ finally gives, for $z >> \frac{d}{4\pi^2 n^2 \lambda}$:

$$\boxed{G(\vec{r}) = e^{-2\gamma\eta} \cdot \left(\frac{2\cdot d}{2\pi n \cdot \rho}\right)^{2\eta} \cdot e^{-\eta E_1}\left(\frac{\rho^2}{4\lambda z}\right)} \qquad (A.14)$$

$$\text{where } \eta = \frac{k_B T \cdot q_o^2 n^2}{16\pi \overline{B}\lambda}$$

For $\rho << z$ one gets:

$$G(\vec{r}) = e^{-\gamma\eta} \cdot \left(\frac{d^2}{4\pi^2 n^2 \lambda z}\right)^{\eta} \qquad (A.15)$$

and for $z << \rho$ one gets

$$G(\vec{r}) = e^{-2\gamma\eta} \cdot \left(\frac{2d}{2\pi n \rho}\right)^{2\eta} \qquad (A.16)$$

which yields the postulated $S(\vec{\kappa})$ in Chapter 2.

APPENDIX B

CONSTRUCTION OF CONJUGATE DIAMETERS. TRANSFORMATION FROM ONE SET TO ANOTHER

The transformation from one set of conjugate diameters to another, where the direction of one of the new diameters is given (the y-axis on the figure), is given by the following formulae (Variables relate to the figure. On the same figure the construction of a set of conjugate diameters from perpendicular diameters in a circle with the same diameter as the long axes of the ellipse is shown):

$$Y_1 = \frac{X_1 \cdot X_2 \cdot \sin\phi}{w_x} \quad ; \quad w_x^2 = A_x^2 + B_x^2$$

$$\text{tg}\ \alpha = - \frac{w_x}{A_x A_y + B_x B_y} \quad ; \quad Y_2 = \frac{w_x}{\sin\alpha} \qquad \text{(B.1)}$$

A_x = x-component of X_1
A_y = y-component of X_1
B_x = x-component of X_2
B_y = y-component of X_2

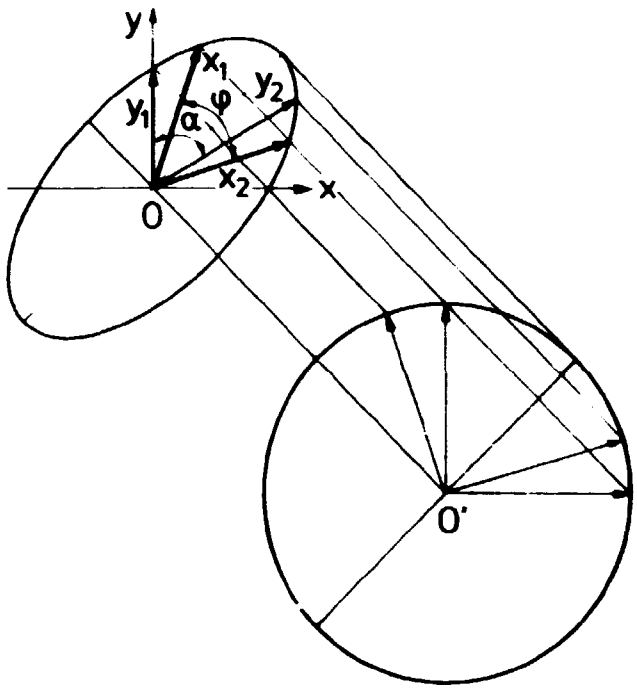

Fig. B. Geometric construction of conjugate diameters

APPENDIX C

NUMERICAL DECONVOLUTION PROCEDURE USED TO OBTAIN CRITICAL DATA FOR THE MONOLAYER LIQ. X-TAL $\bar{8}S5$ and THE MIXTURE $5CT:_9:7CB_x:8OCB_{91-x}$

The experiments reported on in this thesis, are high-resolution X-ray diffraction experiments in the critical region of the nematic to smectic-A phase transition. The perfect crystals, described in Chapter 3, have made it possible to measure the diverging correlation lengths as close as 10^{-5}-10^{-4} in reduced temp. Correlation lengths as large as 10,000 Å can be measured, but in order to obtain these data it is necessary to deconvolute the raw data. For this purpose it is essential to know what the resolution of the spectrometer is. Chapter 4 is dedicated to a discussion of the resolution function when the spectrometer operates in the horizontal triple-axis mode. The numerical deconvolution procedure used to deconvolute the data is a slightly modified version of a procedure developed at M.I.T. by M. Kaplan and coworkers. This appendix will describe this procedure. It is assumed that the resolution function is a given function. In the $\bar{8}S5$ and the mixture experiments the resolution function has two components, the in-plane resolution, and out-of-plane resolution $\delta_T(q_T)\cdot R_*(q_*)$ and $R_v(q_v)$ respectively, where R_* and R_v are assumed to be Gaussians with the measured and/or calculated FWHM.

Once the resolution function is known, the basic problem is to fit the experimental data, that is, longitudinal and transverse scans, to the scattering cross-section convoluted with the resolution function and, if necessary, convoluted with the mosaicity distribution.

Formally the scattered intensity is given by:

$$I(\vec{q}) = \int S_M(\vec{q}-\vec{q}') \cdot R(\vec{q}')d\vec{q}' \qquad (C.1)$$

where:

$$S_M(\vec{q}-\vec{q}') = \int M(\vec{q}''_\perp) \cdot S(\vec{q}-\vec{q}'-\vec{q}''_\perp)d\vec{q}''_\perp \ ;$$

$M(\vec{q}''_\perp)$ is the mosaicity distribution and

$$S(\vec{q}) = \frac{a \cdot \xi_\parallel^2}{1+(\xi_\parallel q_o)^2 \cdot [(q_\parallel - q_o)/q_o]^2 + (\xi_\perp q_o)^2 \cdot (q_\perp/q_o)^2} \qquad (C.2)$$

$$q_\parallel = q_z \quad ; \quad q_\perp^2 = q_x^2 + q_y^2$$

The essential steps in the numerical deconvolution are the following:

1) Conversion of intensity versus motor positions to intensity versus coordinates in reciprocal space.
2) Assuming no resolution correction a first guess on the parameters in (C.2) is obtained.
3) The data from 1) are least-squares fitted to a numerical convolution of S(q) with the resolution function, using the parameters from 2) as a first guess.

C.1. Conversion from motor position to reciprocal space

Since the k-vector of the radiation is $\sim 20 \cdot q_o$ it is simple to perform longitudinal and transverse scans. A longitudinal scan is made merely by rotating the analyzer crystal (A.R.) or rotating the sample arm (S.A.); similarly, a transverse scan can be made by rotating the sample (S.R.) (See the figures of the experimental setup in Chapter 3). This means that performing, either a longtudinal or transverse scan involves stepping only one motor; thus, it is quite convenient to operate the spectro-

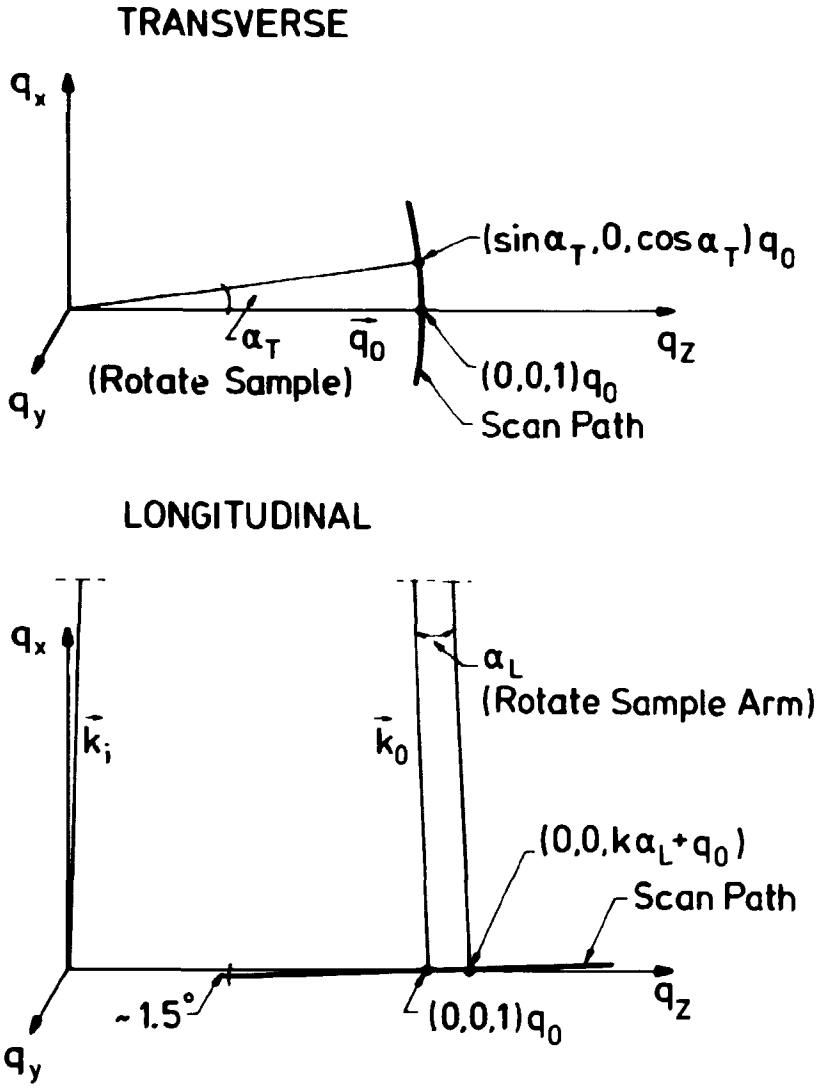

Fig. C.1. Conversion from motorpos. to reciprocal space coordinates.

meter in terms of motor positions, especially at the synchrotron where the data accumulation rate is very high. In principle, the spectrometer could be operated in reciprocal space coordinates. This would be a matter of merely using a different subroutine package for the remote computer control of the spectrometer.

The motor positions have to be converted to reciprocal space coordinates to put the data on a proper scale. This is easily done. In Figure C.1 the connection between angles (motor positions) and reciprocal space coordinates is displayed for either type of scan.

C.2. No resolution correction

There are essentially three physical parameters in (C.2) which can be deduced from the experimental data:

i) The longitudinal correlation length $\xi_{\parallel}(t)$
ii) The transverse correlation length $\xi_{\perp}(t)$
iii) The susceptibility $a \cdot \xi_{\parallel}^2(t)$.

If there are no resolution corrections, these parameters can be readily deduced from a longitudinal and transverse scan.

$$\text{Longitudinal: } q_{\perp} = 0 \Rightarrow S(\vec{q}_{\perp} = 0, q_{\parallel}) = \frac{a \cdot \xi_{\parallel}^2}{1+(\xi_{\parallel} q_0)^2 \cdot [(q_{\parallel}-q_0)/q_0]^2}$$

$$\Rightarrow \text{HWHM (Half Width at Half Maximum)} = \frac{1}{\xi_{\parallel} q_0}$$

$$\text{Transverse: } q_{\parallel} = 0 \Rightarrow S(\vec{q}_{\perp}.0) = \frac{a \cdot \xi_{\parallel}^2}{1+(\xi_{\perp} q_0)^2 \cdot q_{\perp}/q_0)^2}$$

$$\Rightarrow \text{HWHM} = \frac{1}{\xi_{\perp} q_0}$$

a can then obviously be obtained from the peak intensity.

The parameters thus obtained can then be used as a first guess when convoluting $S(\vec{q})$ with the resolution function.

C.3. Least-squares fit

The least-squares fitting was done using a standard fitting routing. This requires a convolution of $S(\vec{q})$ with the resolution function for all points in the longitudinal and transverse scans, typically 30-70 points, and for each set of parameters specified by the fitting routine. This two-dimensional integration, which has to be done many times in one fit, is rather time-consuming, and it is essential to find an integration procedure that is accurate and fast. The functions to be convoluted are

$$S(\vec{q}) = \frac{P(1)\cdot[P(2)]^2}{1+[P(2)]^2[(q_\parallel/q_o-P(4))]^2 + [P(3)]^2\cdot[q_\perp/q_o-P(5)]^2} \; ;$$

$$q_\parallel = q_z \quad ; \quad q_\perp^2 = q_x^2 + q_y^2 \tag{C.3}$$

and

$$R(\vec{q}') = e^{-(\frac{q_y'}{\sigma_y})^2} \cdot e^{-(\frac{q_\parallel'}{\sigma_z})^2} \cdot \delta(q_x') \tag{C.4}$$

where $P(1) \rightarrow P(5)$ are the fitting parameters. Note that $P(2) = q_o\cdot\xi_\parallel$; $P(3) = q_o\cdot\xi_\perp$; $a = P(1)/q_o^2$.

The parameters P(4) and P(5) have been included to deal with the possibility that the longitudinal scan was not made exactly at $q_\perp = 0$, and similarly for the transverse scan.

The two-dimensional integration procedure is one out of a number of integration procedures described by A.H. Stroud[1] which performs the integrations by intelligently picking out a number (N) of points in the plane and for each point specifying a corresponding weight factor. The convolution integral is thus calculated by the sum:

$$\sum_{i=1}^{N} B_i \cdot S(\vec{q}-\vec{q}_i') \cdot R(\vec{q}_i') \tag{C.5}$$

In Reference 1) the points and weight factors B_i; i=1, ... N are specified for N = 12,13,16,20,21,25,28,37,44,48. The points are defined for an integration over a -1, +1-quadrant in the plane. Therefore, scaling is necessary when applying the method to integration in the q'_y-q'_z plane, but since $R(\vec{q}')$ is only significantly different from zero within a few FWHM in the q_y-direction and a few FWHM in the q_z-direction, the integration range was chosen to be 2·(FWHM of R_v) in the q_y-direction and 2·(FWHM of R_*) in the q_z-direction.

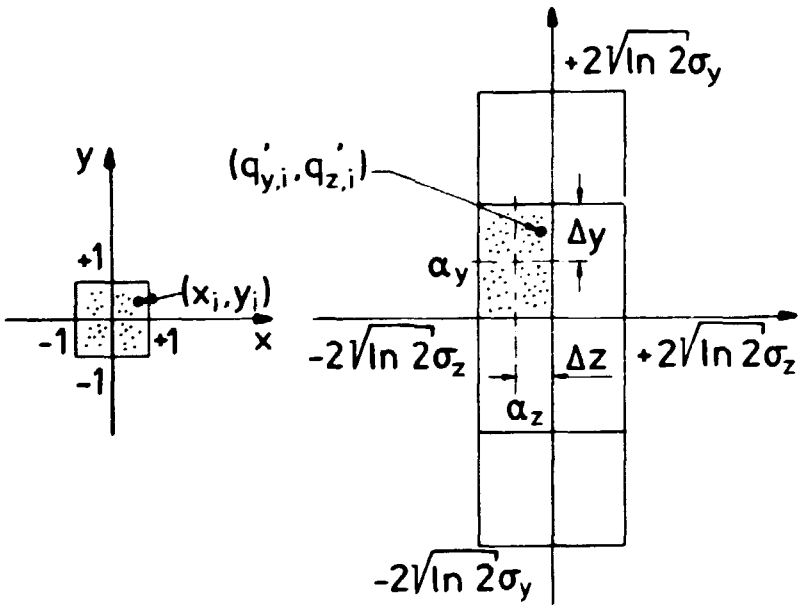

SCALING:

$$(q'_{y,i}, q'_{z,i}) = (\alpha_y + \Delta_y \cdot y_i, x_z + \Delta_z \cdot x_i)$$

Fig. C.2. Area of integration - scaling.

This area is shown in Figure C.2. When performing the integration, this area could, optionally, be subdivided into smaller squares, thus increasing the accuracy of the integration. The points in the -1, +1-quadrant from 1) were scaled to each square (see Figure C.2). A fast and accurate procedure could be obtained with N=28 and four boxes in the q_y-direction and two in the q_z-direction. The analysis was done on a P.D.P.-11-computer with floating point processor and a complete fit could be done in approximately 5 minutes.

If pretransitional mosaicity is an essential feature of the nematic to smectic-A phase transition, the resolution function must be modifed by inclusion of the mosaicity, as outlined in Chapter 4. Since the out-of-plane resolution $R_v(q_y'))$ in any case was much broader than the mosaicity, the only correction to $R(\vec{q}')$ is in the q_x-direction. The inclusion of mosaicity in the fit was made simply by convoluting $S(\vec{q})$ with $M(q_x)$ before convolution with $R(\vec{q}')$. The convolution of $M(q_x)$ and $S(\vec{q})$ was made by a simple equidistant summation along q_x:

$$S_M(q_x,q_y,q_z) = \sum_i M(q'_{x,i}) \cdot S(q_x - q'_{x,i}, q_y, q_z)$$

where $M(q'_{x,i})$ was obtained from transverse scans at or just below T_c.

The only correction to the intensity was a volume correction. The sample geometry is shown in Figure C.3. From this figure it is clear that the <u>beam attenuation</u> goes like:

$$e^{-t/\cos\phi}$$

and that the <u>illuminated volume</u> is proportional to $1/\cos\phi$. This gives the following gain factor to the intensity:

$$e^{-t/\cos\phi} \cdot \frac{1}{\cos\phi} \qquad (C.6)$$

All measured intensities have thus been divided by this factor.

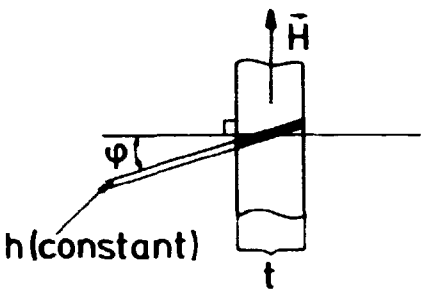

Fig. C.3. Sample geometry - transmission geometry.

REFERENCES

1) Stroud, A.H. "Approximate calculation of multiple integrals" Prentice Hall, Englewood Cliffs, N.J. p. 255-265.

APPENDIX D

COMBINATION OF THE TWO RESOLUTION ELLIPSES

In order to be able to combine the two ellipses to a final resolution function it is useful to transform the $\vec{X}_1$, $\vec{X}_2$-set of conjugate diameters to a new set with $\vec{X}_2' \perp \vec{k}_i$. This is done by using the formulas of Appendix B, and the result is that:

$$X_1'^2 = \frac{(X_{0,1}^2+X_{0,2}^2)\cdot\cot^2\theta_M}{\sin^2\alpha_M} \quad ; \quad X_3'^2 = \frac{(X_{0,3}^2+X_{0,4}^2)\cot^2\theta_M}{\sin^2\alpha_A}$$

$$X_2'^2 = \frac{X_{0,1}^2\cdot X_{0,2}^2}{X_{0,1}^2+X_{0,2}^2} \quad ; \quad X_4'^2 = \frac{X_{0,3}^2\cdot X_{0,4}^2}{X_{0,3}^2+X_{0,4}^2} \qquad (D.1)$$

$$\text{tg}\ \alpha_M = -\frac{X_{0,1}^2+X_{0,2}^2}{X_{0,1}^2\cdot\tan\theta_M} \quad ; \quad \text{tg}\ \alpha_A = -\frac{X_{0,3}^2+X_{0,4}^2}{X_{0,3}^2\tan\theta_M}$$

where $X_{0,1} \equiv Ck\sigma_o$ and $X_{0,2} = Ck\sigma_D$; $C = 2\sqrt{2\ell n2}$ and α_M is the angle between X_1' and X_2'. Similarly α_A is the angle between X_3' and X_4'.

From Chapter 4 one has:

$$X_3' = X_3 = "\infty" \quad ; \quad X_4' = X_{0,2} \quad ; \quad \alpha_A = 90-\theta_M$$

The set-up in Figure 3.1 in Chapter 3 corresponds to configuration 2) in Figure 4.3 in Chapter 4. In Figure D.1 this set-up is shown together with the resolution ellipses and conjugate diameters X_1, X_2, X_1', X_2' and X_3, X_4, X', X_4'.

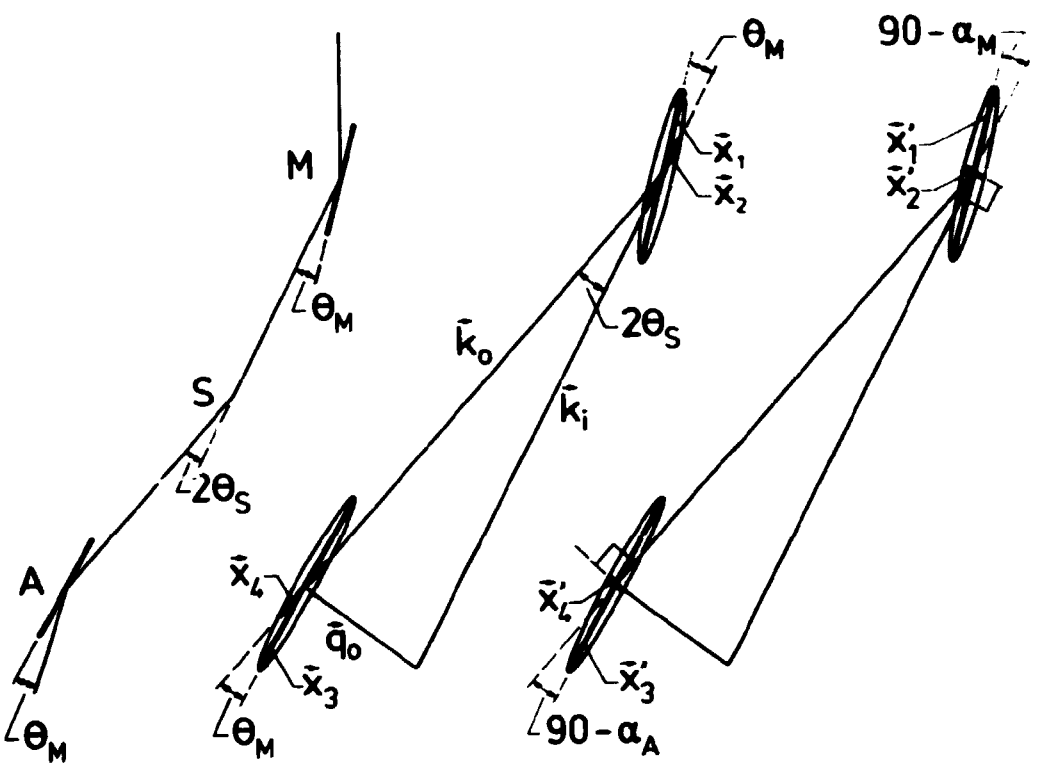

Fig. D.1. The two resolution elipses tied to the monochromator and the analyzer, respectively. Note that $\vec{X}_1 || M$ and $\vec{X}_3 || A$.

It is now straightforward to combine the resolution ellipses, since deviations of $\vec{k}$ along $\vec{X}'_2$ or $\vec{X}'_4$ automatically fulfils the condition of elastic scattering. These two conjugate diameters will thus contribute to R_i by the half-contour ellipse shown in Figure D.2a, where it is assumed that $\sigma_0^2 >> \sigma_D^2$, leading to the relation $X'_2 = X'_4$.

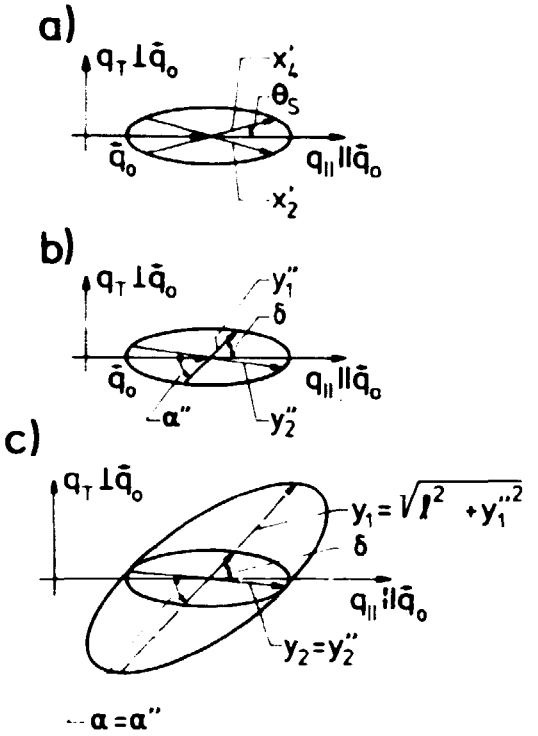

Fig. D.2. The combination of $\vec{X}_2'$ and $\vec{X}_4'$ and the final resolution ellipse.

In the same Figure D.2b a transformation of the $\vec{X}_2'$, $\vec{X}_4'$-set of conjugate diameters is shown. The formulae for Y_1'', Y_2'' and α'' are:

$$Y_1''^2 = \frac{4X_4'^2 X_2'^2 \cdot \cos^2\theta_s \sin^2\theta_s}{X_4'^2 \sin^2(\delta-\theta_s) + X_2'^2 \sin^2(\delta-\theta_s)}$$

$$\mathrm{tg}\,\alpha'' = -\frac{X_4'^2 \sin^2(\delta-\theta_s) + X_2'^2 \sin^2(\delta+\theta_s)}{X_4'^2 \sin(\delta-\theta_s)\cos(\delta-\theta_s) + X_2'^2 \sin(\delta+\theta_s)\cos(\delta+\theta_s)}$$

$$Y_2''^2 = \frac{X_4'^2 \sin^2(\delta-\theta_s) + X_2'^2 \sin^2(\delta+\theta_s)}{\sin^2\alpha''}$$

In the above formulae it is assumed that $90-\theta_S > \delta > \theta_S$. It is straightforward to construct the transformation in other regions for δ using Appendix B.

Note that the contribution from $\vec{x}'_2$ and $\vec{x}'_4$ to the in-plane resolution is <u>independent</u> of the spectrometer configuration. Furthermore it is salient to notice that for, $\theta_S \to 0$ and $\sigma_M^2 >> \sigma_D^2$, this contribution degenerates to a line along $\vec{q}_o$ of length $Y_2'^2 = 2 \cdot X_{0,2}^2$ which is simply a convolution of the

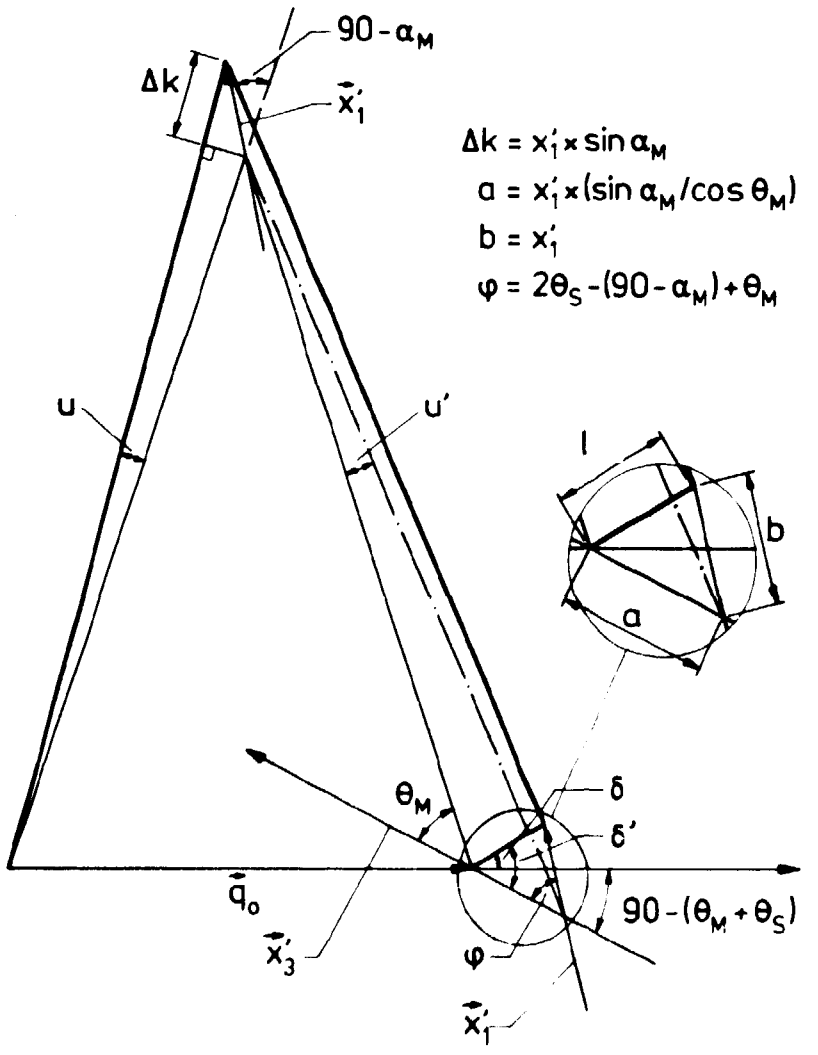

Fig. D.3. The combination of $\vec{x}'_1$ and $\vec{x}'_3$.

Darwin-reflectivity with itself = the direct beam profile! Similarly, if $\theta_s \to 0$ and $\sigma_D^2 >> \sigma_M^2$ the contribution from X_2' and X_4' degenerates to a line along $\vec{q}_o$ of length $Y_2^2 = X_{0,2}^2$.

The remaining contribution to R_i comes from X_1' and X_3'. These two must be combined under the condition of elastic scattering. The contribution to R_i depends on the spectrometer configuration and the contribution is derived in Figure D.3 for one of the two analogous non-dispersive set-ups (configurations 1 & 2 in Figure 4.3 in Chapter 4).

The half-value ℓ of the line contribution in Figure 3 can be found by looking at the probability for a scattering process like the one in Figure D.3. Generally, such a scattering process can be designated by the coordinates (X_M, X_A), where X_M is the coordinate along $\vec{X}_1'$ and X_A is the coordinate along $\vec{X}_3'$; the following relation then holds between X_M and X_A:

$$|X_A| = |X_M| \cdot \frac{\sin\alpha_M}{\cos\theta_M}$$

The relation is imposed because the scattering is elastic. The probability for the scattering process (X_M, X_A) is:

$$P(X_M, X_A) = e^{-1/2 \left(\frac{X_M}{X_1'}\right)^2} \cdot e^{-1/2 \left(\frac{X_A}{X_3'}\right)^2}$$

$$= e^{-1/2\, X_M^2 \left(\frac{1}{X_1'^2} + \left(\frac{\sin\alpha_M}{X_3'^2 \cos\theta_M}\right)\right)^2}$$

$$\equiv e^{-1/2 \left(\frac{X_M}{\sigma_\ell}\right)^2}$$

where

$$\left(\frac{1}{\sigma_\ell}\right)^2 = \left(\frac{1}{X_1'}\right)^2 + \left(\frac{\sin\alpha_M}{X_3'\cos\vartheta_M}\right)^2 = \left(\frac{1}{X_1'}\right)^2$$

and ℓ can be found by setting $X_M = 2\sqrt{2\ln 2'}\cdot\sigma_\ell$ as done in Figure D.3.

Once the angle between ℓ and a in the triangle a,b,$\ell \equiv \delta'$ is determined it is straightforward to find the angle between $\vec{q}_o$ and $\ell \equiv \delta$ for the specific set-up and if ℓ has been found, the line contribution to the resolution function, originating from $\vec{X}_1'$ and $\vec{X}_3'$, can be combined with the ellipse determined by $\vec{X}_2'$ and $\vec{X}_4'$. In Figure D.2 there is prepared for it and the final resolution ellipse is given by the conjugate diameters $\vec{Y}_1$, $\vec{Y}_2$ and the angle between them α, and the angle δ, where:

$$\begin{aligned} Y_1^2 &= \ell^2 + Y_1''^2 \\ Y_2^2 &= Y_2''^2 \\ \alpha &= \alpha'' \end{aligned} \qquad \text{(D.3)}$$

The rule of sum-of-squares has been used for conjugate diameters along the same direction (Reference 2 in Chapter 4; see Figures D.2b) and D.2c)).

Looking at the triangle a,b,ℓ in Figure D.3 the following general expressions are valid for ℓ and δ':

$$\ell^2 = a^2 + b^2 - 2ab\cos\vartheta = X_1'^2 \cdot \left[\frac{\sin^2\alpha_M}{\cos^2\vartheta_M}\right.$$

$$\left. + 1 - 2 \cdot \frac{\sin\alpha_M}{\cos\vartheta_M} \cdot \cos\phi\right] = X_1'^2 \cdot f^2$$

and

$$\text{Cos}\,\delta' = \frac{a^2+\ell^2-b^2}{2a\ell} = \frac{f^2 + \dfrac{\sin\alpha_M}{\cos^2\theta_M} - 1}{2 \cdot \dfrac{\sin\alpha_M}{\cos\theta_M} f} \qquad \text{(D.5)}$$

α_M is given by the formula in the beginning of the appendix.

ϕ is the angle between a and b in triangle a,b,ℓ and is given by the following table for the four different configurations.

Configuration	ϕ
+ - - ~ 1	$\lvert 90-\alpha_M+\theta_M-2\theta_S\rvert$
+ + - ~ 2	$\lvert 90-\alpha_M-\theta_M-2\theta_S\rvert$
+ - + ~ 3	$\lvert 90+\alpha_M+\theta_M-2\theta_S\rvert$
+ + + ~ 4	$\lvert 90-\alpha_M+\theta_M+2\theta_S\rvert$

APPENDIX E

THE EFFECT OF MOSAICITY IN THE SAMPLE

The resolution is modified by the mosaicity of the sample and for some experiments mosaicity may be the factor which limits the resolution; therefore it is worth looking at the effect of mosaicity in the sample. The argument $\vec{q}_o$ will be dropped in R in the following. If the mosaicity is described by

$$M(\vec{q}''_\perp) = M_T(q''_T) \cdot M_v(q''_v); \quad \vec{q}''_\perp = q''_T \cdot \hat{1}_T + q''_v \cdot \hat{1}_v$$

where $M(\vec{q}''_\perp)dq''_T dq''_v$ is the fraction of "mosaic blocks" with normal vector in the solid angle $\delta\Omega$ shown in the figure, then the expression (*) in Chapter 4 must be modified in the following way:

$$I(\vec{q}) = \int S_M(\vec{q}-\vec{q}')R(\vec{q}')d\vec{q}'$$

where

$$S_M(\vec{q}-\vec{q}') = \int M(\vec{q}''_\perp) \cdot S(\vec{q}-\vec{q}'-\vec{q}''_\perp)d\vec{q}''_\perp$$

$$= \int M(\vec{q}_\perp-\vec{q}'_\perp-\vec{q}''_\perp) \cdot S(\vec{q}''_\perp, q_{//}-q'_{//})d\vec{q}''_\perp$$

(see the figure).

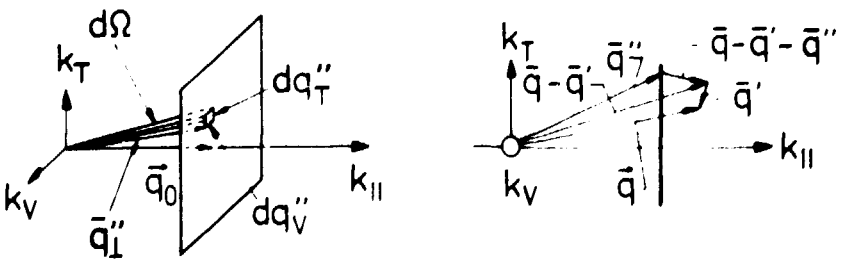

Inserting $S_M(\vec{q}-\vec{q}')$ into the expression for $I(\vec{q})$ gives:

$$I(\vec{q}_\perp,q_z) = \int \ldots \int M_T(q_T-q_T'-q_T'') \cdot M_V(q_V-q_V'-q_V'') \cdot S(q_T'',q_V'',q_n-q_n')$$

$$\cdot dq_T''dq_V'' \cdot R_T(q_T') \cdot R_V(q_V') \cdot R_n(q_n')dq_T'dq_V'dq_n' =$$

$$\int \{[M_T(q_T-p_T'-q_T'') \cdot R_T(q_T')dq_T'] \cdot$$

$$[\int M_V(q_V-q_V'-q_V'') \cdot R_V(q_V')dq_V'] \cdot S(q_T'',q_V'',q_n-q_n')$$

$$\cdot R_n(q_n')\} \cdot dq_T''dq_V''dq_n'$$

$$\equiv \int \alpha_T(q_T-q_T'') \cdot \alpha_V(q_V-q_V'') \cdot R_n(q_n') \cdot S(q_T'',q_V'',q_n-q_n')dq_T''dq_V''dq'$$

where

$$\alpha_{T,V}(q_{T,V}-q_{T,V}'') \equiv \int M_{T,V}(q_{T,V}-q_{T,V}'-q_{T,V}'') \cdot R_{T,V}(q_{T,V}')dq_T'$$

Using the α-notation one gets further:

$$I(\vec{q}) = \int \alpha_T(q_T-q_T'') \cdot \alpha_V(q_V-q_V'') \cdot R_n(q_n-q_n'')$$

$$\cdot S(q_T'',q_V'',q_n'')dq_T''dq_V''dq_n''$$

where $q_n'' = q_n-q_n'$.

This gives:

$$I(\vec{q}) = \int R_C(\vec{q}-\vec{q}'')\ S(\vec{q}'')d\vec{q}''$$

with $R_C \equiv \alpha_T \cdot \alpha_V \cdot R''$.

Thus the usual expression for $I(\vec{q})$ is obtained except $R \rightarrow R_C$, which means that the corrected resolution function $R_C \neq R$ if the mosaicity-FWHM >> FWHM of either R_T or R_V.

Sales distributors:
Jul. Gjellerup, Sølvgade 87,
DK-1307 Copenhagen K, Denmark

Available on exchange from:
Risø Library, Risø National Laboratory,
P. O. Box 49, DK-4000 Roskilde, Denmark

ISBN 87-550-0823-
ISSN 0106-2840